FLIGHT TEST OF A SUPERSONIC DECELERATOR ON EARTH TO SIMULATE A MARS ENTRY

Darrell R. Branscome

Thesis submitted to the Graduate Faculty of the
Virginia Polytechnic Institute and State University
in partial fulfillment of the requirements for the degree of
MASTER OF SCIENCE
in
Mechanical Engineering

Approved: _____
Chairman, F. J. Pierce

_____ J. B. Jones

_____ R. A. Comparin

September, 1973

Blacksburg, Virginia

TABLE OF CONTENTS

LIST OF TABLES

LIST OF FIGURES

LIST OF SYMBOLS

A	reference drag area
A_p	strength reduction factor
B_{cp}	ballistic number of parachute
$C_{A,o}$	flight test parachute nominal axial force coefficient
$C_{D,o}$	flight test parachute average drag coefficient
C_D	average drag coefficient
$(C_{D,o})_{eff}$	parachute effective drag coefficient (based on vertical descent velocity and acceleration)
C_M	moment coefficient
D_l	bluff forebody (aeroshell) diameter
D_o	nominal parachute diameter
D_d	disk diameter
D_p	projected parachute diameter
D_v	parachute vent diameter
E_l	aeroshell drag force
F	force
F_o	parachute opening force
H_b	geometric height of parachute band
H_d	geometric height of parachute disk
H_g	geometric height of parachute gap
H_p	pressure scale height
H_v	geometric height of parachute vent

I_{sp}	rocket fuel specific impulse
K	constant
M_w	molecular weight
M	Mach number
N	number of gores in parachute
P'_R	required total strength
P	pressure load on parachute canopy
P_c	maximum parachute canopy cloth design load
P_{SL}	maximum parachute suspension line design load
P_{RT}	maximum parachute radial tape design load
R*	universal gas constant
S_o	nominal surface area of parachute including gap and vent
S_b	band surface area of the parachute
S_g	gap area of the parachute
S_d	disk surface area of the parachute
S_p	parachute projected surface area
S_v	vent area of the parachute
S_{og}	nominal surface area of parachute gore
S_{bg}	band surface area of parachute gore
S_{gg}	gap area of parachute gore
S_{dg}	disk surface area of parachute gore
S_{vg}	vent area of parachute gore
SF	safety factor
T	temperature

T_r	retro descent thrust
T_o	Mars surface temperature
V	velocity
V_i	retro descent ignition velocity
W	weight
W_p	propellant weight
W_i	weight of vehicle at retro descent ignition
W_f	weight of landed vehicle
X	parachute opening shock amplification factor
a	acceleration
g_c	the Earth's gravitational constant
g_e	acceleration due to gravity on Earth
g_m	acceleration due to gravity on Mars
h	altitude above the surface of a planet
h_T	altitude at the troposphere
k	specific heat ratio
ℓ	parachute trailing distance behind bluff forebody
m	mass
m_A	apparent mass
m_t	total mass
m_{pl}	mass of payload
p	gas pressure
p_o	surface gas pressure
q	free stream dynamic pressure

r	radius of curvature
t	time
t'	time from mortar fire
$\dot{z}_E$	payload vertical velocity
$\ddot{z}_E$	payload vertical acceleration
dp	incremental change in pressure
dh	incremental change in altitude
w_{vg}	vent geometric base width of parachute gore
w_{dg}	disk geometric base width of parachute gore
w_{gg}	gap geometric width of parachute gore
w_{bg}	band geometric width of parachute gore
γ	flight path angle
ρ	atmospheric density at altitude
ρ_o	atmospheric density at surface of Mars
ρ_T	atmospheric density at the troposphere of Mars
α	angular acceleration
ω	angular velocity
θ_g	disk-gap-band parachute gore included angle
Γ	atmospheric adiabatic temperature lapse rate
Σ	summation

I. INTRODUCTION

When a spacecraft mission includes entry into and descent through a planetary atmosphere of sensible density, a deployable aerodynamic decelerator system may be employed to control the spacecraft's motion in preparation for landing or initiation of other means (e.g., retrorockets) of effecting a terminal landing operation. A typical deployable aerodynamic deceleration system is a combination of pliant fabric surfaces designed to decelerate, stabilize, and control the descent of the spacecraft. This type of system can produce large drag surfaces from relatively small masses of material. During deployment, structural stresses on both the spacecraft and the decelerator are caused primarily from inertial and friction forces and, during inflation, from aerodynamic forces generated by the transfer of kinetic energy from the entering spacecraft to the surrounding air.

The size and required strength of the decelerator drag or lifting surface are determined by the spacecraft's gross weight, the deployment conditions (altitude and velocity), and the velocity desired during steady descent. The aerodynamic characteristics of the main descent surface are defined by the stability, controllability, and maneuverability required during the descent. For systems to be deployed in the atmospheres of planets other than the Earth, environmental data needed for design include information on the composition, the density/altitude profile of the atmosphere, and on surface gravity. Special design considerations must be given to scale effects, model laws, and unusual

environments.

Parachutes have grown in diversity of design to meet the requirements of parachutists, aircraft spin recovery, cargo drop, and space missions. Aerodynamic decelerators have assumed an important role in aerospace technology, as exemplified by the Apollo Program, where an efficient, reliable, parachute landing system was essential for the successful return by man from his first voyage into deep space. Large technical efforts were required to develop the decelerator systems used on Mercury, Gemini, and Apollo. Parachutes have been used on these space programs to decelerate spacecraft during reentry through the Earth's atmosphere.

The operational reliability of parachute landing systems has been extremely high. The only catastrophic failure of a manned-spacecraft parachute system occurred with Russia's Soyuz 1 in April, 1967, and cost the life of Cosmonaut Vladimar Komarov. It was learned that the main parachute system did not function properly and was not disconnected when Komarov deployed his reserve system. The reserve parachutes became twisted around the primary system and could not inflate. Deployable deceleration system failures, caused by design deficiencies and difficulties in adequately simulating operational conditions, have also been encountered during development tests.

For the successful development of a parachute system the operating environment must be known. The analysis for a Mars mission must consider the Martian environment and any applicable scaling and modeling laws for relating the Martian environment to that on Earth.

Studies that have been conducted in interplanetary missions to Mars have given considerable insight into parachute requirements for a soft landing. The Martian atmosphere is less dense than that on Earth and is considered to have a surface pressure between five and ten millibars as compared to the surface pressure on Earth of 1013 millibars. The gravitational constant for Mars is 12.3 ft/sec^2 compared to 32.2 ft/sec^2 for the Earth.

II. MARS ATMOSPHERIC ENVIRONMENT

Since this analysis involves a decelerator system to simulate a Mars mission, the first step is to identify the Martian environmental characteristics and a density altitude profile. The Martian atmosphere is relatively unknown, but several atmospheric models have been postulated.

Eight engineering model atmospheres and their respective physical characteristics are presented in table 1. As seen in table 1 the surface pressure ranges from 5 to 20 millibars for the postulated engineering models and this is significantly less than the surface pressure on Earth of 1013 millibars. The atmospheric density at the surfaces ranges from 1.32×10^{-5} to 7.44×10^{-5} slugs/ft^3, which is about 100 times less than the earth's surface atmospheric density of 2.375×10^{-3} slugs/ft^3. The postulated molecular weight, pressure scale height, and adiabatic temperature lapse rate for each engineering model are presented.

The Martian atmosphere is assumed to have two layers and the altitude of transition is referred to as the tropopause. Above the tropopause the temperature is assumed constant and below the tropopause the temperature is assumed to be a linear function of altitude. Two equations were used to describe the atmospheric density profile for each of the engineering model atmospheres. The equations used are as follows:

Below the tropopause,

TABLE 1. MARS ENGINEERING MODEL ATMOSPHERIC CONSTANTS

	VM-7	VM-8	VM-1	VM-2	VM-3	VM-4	VM-9	VM-10
Surface Pressure, p_o, mb	5.0	5.0	7.0	7.0	10.0	10.0	20.0	20.0
psf	10.4	10.4	14.6	14.6	20.9	20.9	41.7	41.7
Surface Density, ρ_o, (slugs/ft^3)10^5	1.32	2.56	1.85	3.59	2.65	4.98	5.30	7.44
Density at Tropopause, ρ_T, (slugs/ft^3)10^5	0.573	0.397	0.803	0.556	1.15	1.016	2.32	1.53
Surface Temperature, T_o, °R	495	360	495	360	495	360	495	360
Molecular Weight, M_w, mol^{-1}	31.2	44.0	31.2	44.0	31.2	42.7	31.2	31.9
Adiabatic Lapse Rates, Γ, °R/1000 ft	-2.13	-2.96	-2.13	-2.96	-2.13	-3.21	-2.13	-2.36
Tropopause Altitude, h_T, 1000 ft	63.3	61.0	63.3	61.0	63.3	56.1	63.3	75.8
Pressure Scale Height, H_p, 1000 ft	46.520	16.480	46.520	16.480	46.520	16.980	46.520	22.68
Effective Height of Atmosphere, 1000 ft	621	252	636	258	653	269	777.4	392.6

$$\rho = \rho_o \left[1 + \frac{\Gamma h}{T_o} \right]^{-\frac{(M_w) g_m}{g_c R^* \Gamma} - 1} \qquad (1)$$

Above the tropopause,

$$\rho = \rho_T \, e^{-\frac{(h - h_T)}{H_p}} \qquad (2)$$

Atmospheric density as a function of altitude is presented for each atmospheric model in figure 1.

ρ is the atmospheric density at altitude, slugs/ft^3

ρ_o is the atmospheric density at the surface, slugs/ft^3

Γ is the temperature lapse rate (usually negative), $^\circ$R/1000 ft

h is the altitude above the surface, ft

T_o is the atmospheric temperature at the surface, $^\circ$R

M_w is the atmospheric molecular weight, mol^{-1}

g_m is the acceleration of gravity at the surface of Mars, 12.3 ft/sec^2

g_c is the earth's gravitational constant

R^* is the universal gas constant

ρ_T is the density at the tropopause, slugs/ft^3

h_T is the altitude at the tropopause, ft

H_p is the pressure scale height, ft

In order to establish an entry point consistent with all the atmospheres, an effective height or upper limit for each atmosphere was determined. This was done by computing the altitude at which the den-

sity corresponded to the density of the Earth's atmosphere at 400,000 feet altitude, which is generally accepted as the effective height of the Earth's atmosphere for reentry purposes. The calculations were made by setting density in equation (2) equal to the value of the Earth's density at 400,000 feet (0.36165×10^{-10} slugs/ft^3) and solving for the altitude h. The resulting equation is

$$h = - H_p \ln \left(\frac{\rho_{(\text{earth } 400000 \text{ ft})}}{\rho_T} \right) + h_T \qquad (3)$$

Values of the effective heights of the various Martian atmospheres are given in table I. The highest value resulting from the calculations was approximately 777,000 feet. The entry point of 800,000 feet was used to insure that computations of trajectories would be started outside the sensible atmosphere.

The altitude density profiles for the engineering atmospheric models are shown in figure 1. The density of the VM-8 model atmosphere is less than the other models down to an altitude of about 45,000 feet at which point the VM-7 model atmosphere becomes the least dense. The VM-8 model atmosphere was used for the analysis and subsequent data obtained from fly-by Mars spacecraft missions confirm this choice as being most representative.

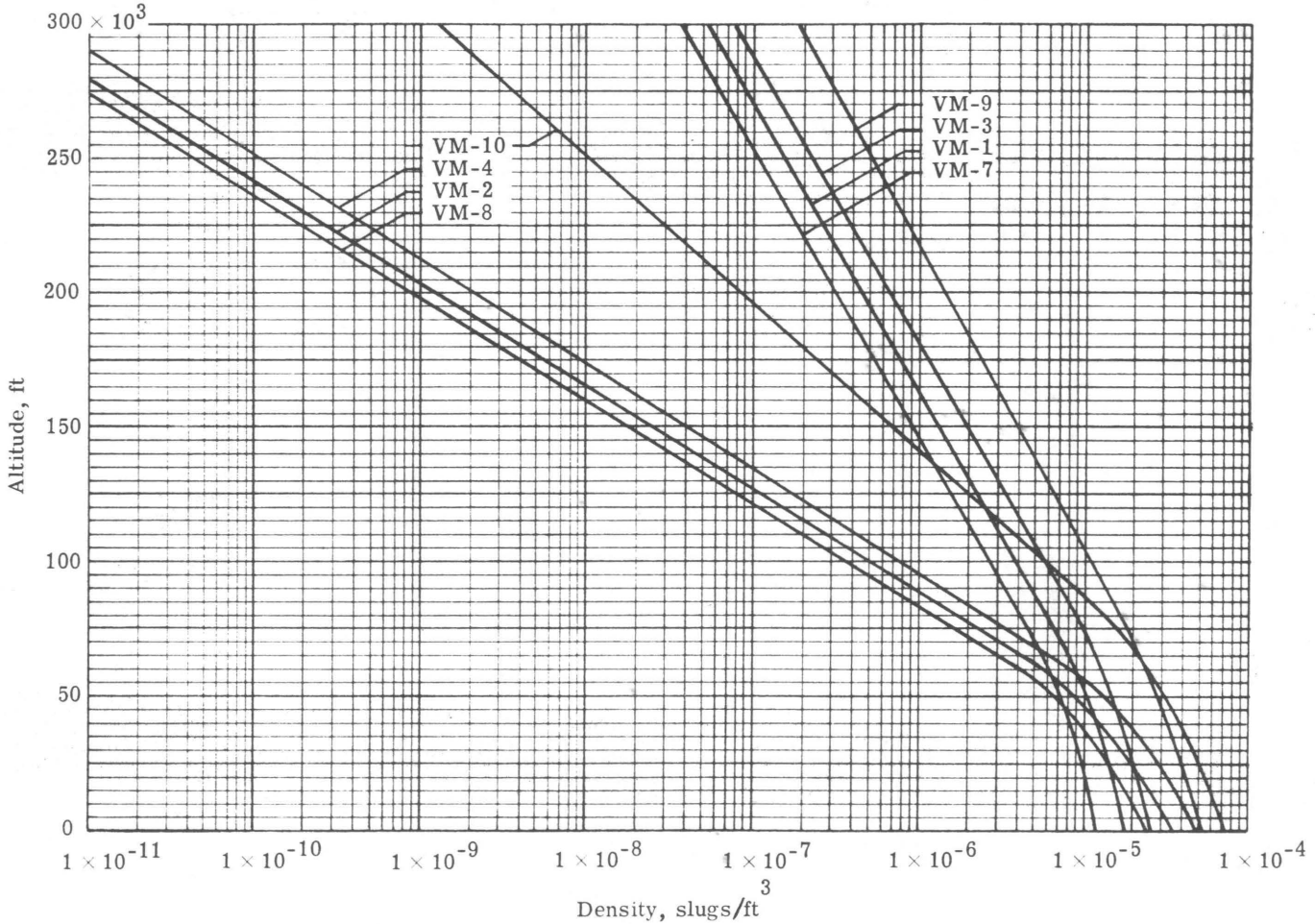

Figure 1.- Mars engineering atmospheric model altitude-density profile.

III. DECELERATOR FOR A MARS MISSION

Research and development of deployable decelerator systems must be governed by the future needs of those systems. This chapter presents the analysis involved in selecting a parachute to be used on an unmanned mission to the planet Mars. Typical decelerator deployment conditions for representative entry through two engineering model atmospheres of Mars and the deployment conditions of parachutes used for Apollo reentry throught the Earth's atmosphere are compared in figure 2. It is evident that Mars entry generates requirements for flexible decelerate technology at higher Mach numbers and lower dynamic pressures than are typical for earth reentry missions. A comparison of parachute flight experience and the region of interest for Mars application is made in figure 3. A general sequence of events from atmosphere entry to landing for a Mars mission is illustrated in figure 4. Atmospheric drag decelerates the bluff body capsule to some Mach number and altitude at which time a parachute is deployed. After parachute deployment the bluff forebody is ejected and the lander descends to some altitude where a terminal retro descent system further decelerates the lander to essentially a zero velocity for a soft landing. During entry through the Martian atmosphere, the primary purpose of a parachute system is to decelerate and control a lander's motion in preparation for initiation of a retro-descent system.

Minimum weight is always a primary goal for flexible decelerators and terminal retro-descent systems for space missions. The performance

of the parachute system has a significant impact on the retro-descent system; therefore, the parachute must be sized to minimize the weight requirements of the terminal retro-descent system.

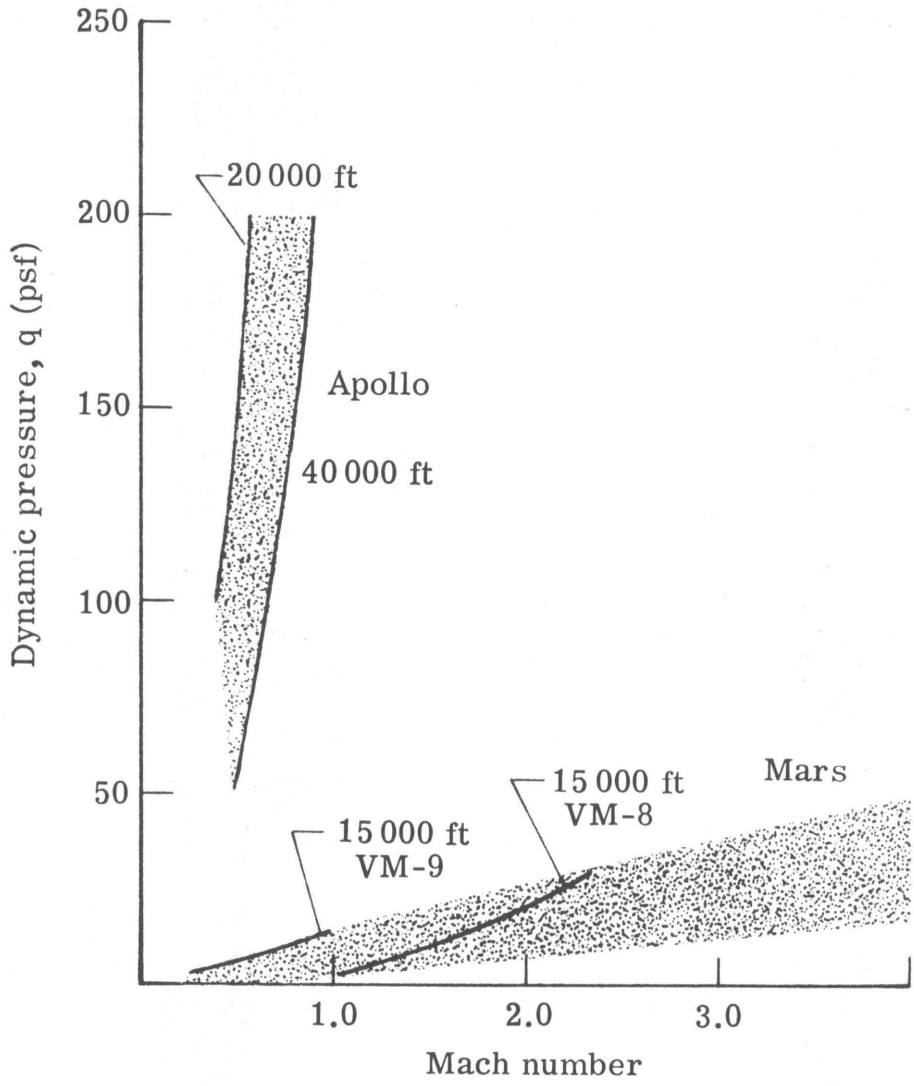

Figure 2.- Comparison of decelerator deployment parameters for Mars and Earth entry.

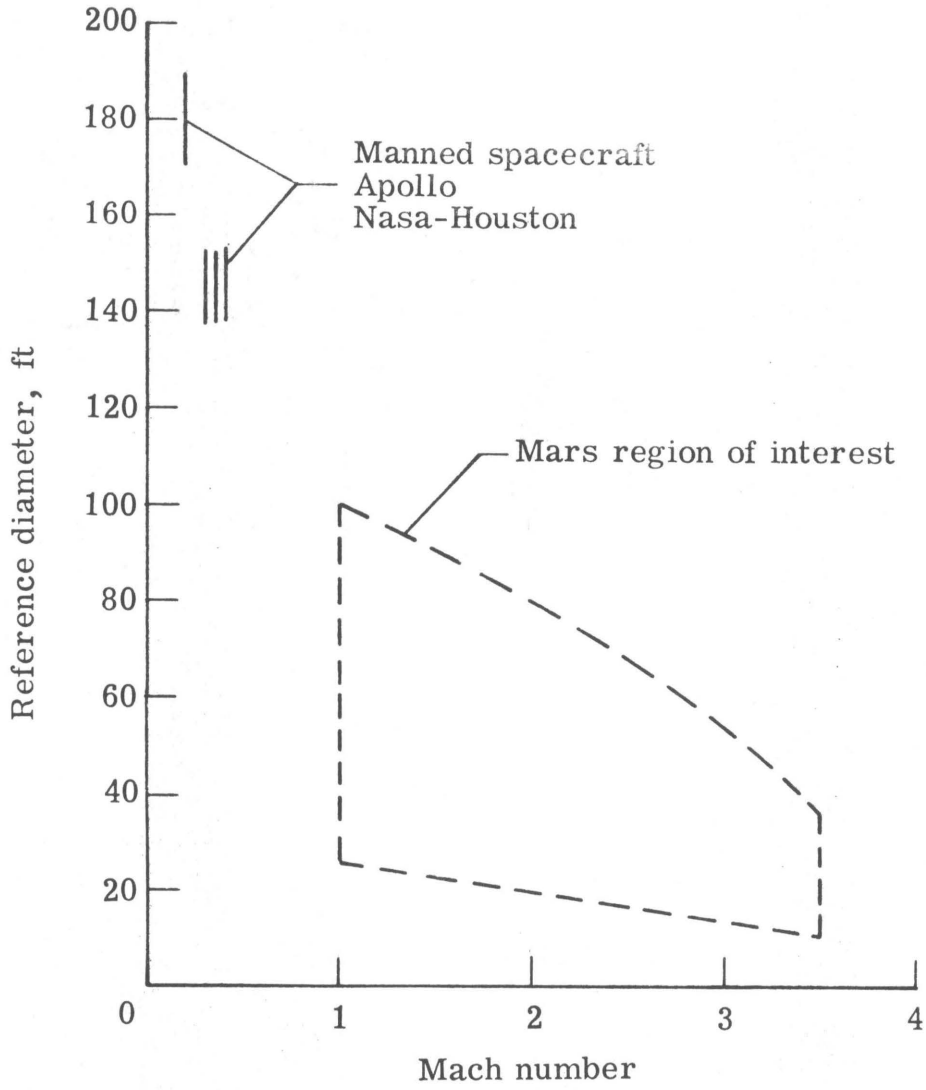

Figure 3.- Decelerator technology region of interest for Mars entry.

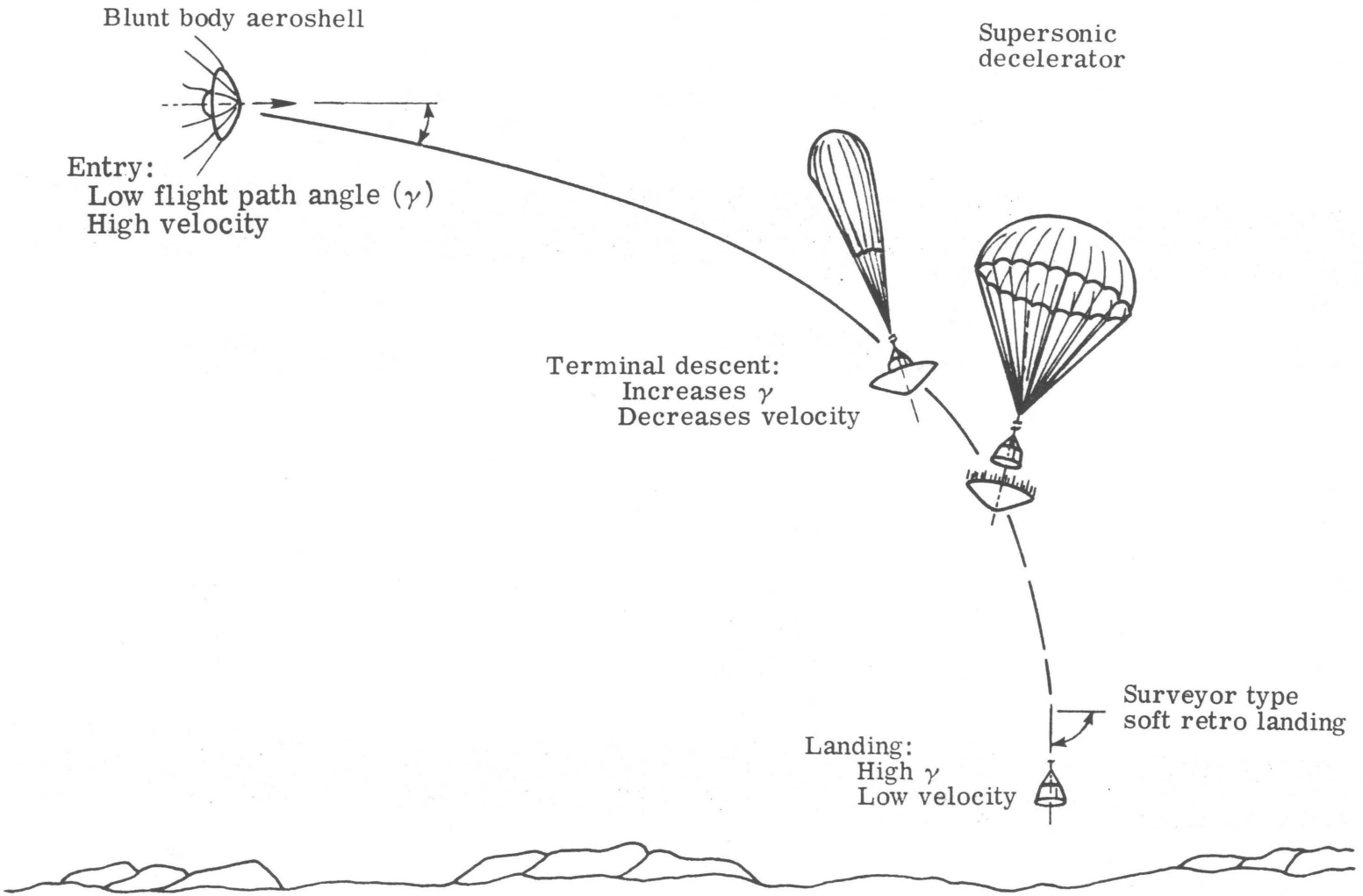

Figure 4.- General sequence of events for Mars terminal descent.

A. Mars Mission Profile

One of the basic flight modes being considered for an unmanned lander mission to Mars is the orbit mode illustrated in figure 5. It is assumed that the lander vehicle is guided to the vicinity of Mars by a bus vehicle which can either fly-by the planet or enter orbit. In the orbit mode the bus carries itself and the lander into a Martian orbit. At some time later, the lander is separated from the bus and decrbits onto an impact trajectory.

An advantage of the orbit mode is that it allows shallow entries which make better use of the light atmospheres for aerodynamic braking. With shallow entries a blunt forebody will slow the lander enough to make use of a parachute to accomplish a major part of the deceleration required during terminal descent to the surface of Mars.

A general mission sequence of events from entry to landing is illustrated in figure 4. The Mars atmosphere to be encountered may be anywhere within the range postulated by the VM series of atmospheric properties discussed in the Chapter II. The surface pressure is considered to be between 5 and 20 millibars with the resulting density versus altitude profiles dependent also upon postulated temperature profiles.

As illustrated in figure 4 the descent through the Martian atmosphere to the surface of the planet can be separated into three distinct phases: aeroshell descent, parachute descent, and terminal retro rocket descent. Trajectory analyses covering the envelope of entry conditions and mission requirements established a range of parachute

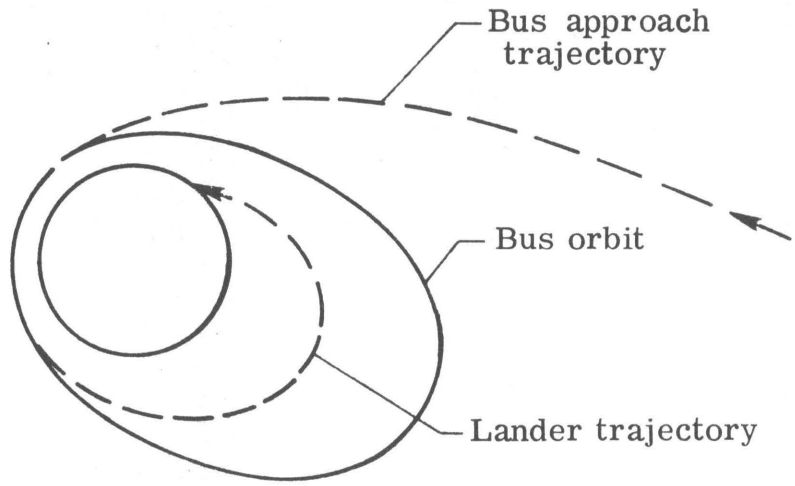

Figure 5.- Out-of-orbit lander flight mode
for Mars mission.

descent system requirements including parachute deployment Mach numbers and altitudes. The entry conditions for a bluff body aeroshell with 60 degree half-angle is determined and controlled by deorbit maneuvers of the lander and trans Mars trajectory corrections. The vehicle entry envelope chosen is defined by the ranges of parameters in table 2. The parameter in the table 2 referred to as ballistic number is the ratio of the vehicle mass to its effective drag area ($B_{cp} = m/C_D A$). The most critical atmosphere model for establishing decelerator requirements is VM-8 because with this atmosphere model the velocity at time of parachute deployment is greatest. The terminal descent corridor of an entry vehicle defined by the parameters in table 2 is shown in figure 6. When an entry vehicle with a ballistic number of 0.32 slug/ft^2 descends through the VM-8 model atmosphere, a Mach number of 2.7 is reached at a higher altitude for an entry velocity of 12,000 ft/sec and an entry flight path angle of -15° than for an entry velocity of 16,000 ft/sec and an entry flight path angle of -20°. However, for either case a Mach number of 2.7 is reached above 15,000 feet altitude which is considered to be the minimum acceptable altitude for parachute deployment during a Mars entry (reference 19).

B. Propellant Weight Sensitivity to Retro-Descent Initiation

One of the important parameters to be considered in sizing a parachute is the parachute terminal velocity and flight path angle desired at acquisition of the terminal retro-descent system. The parachute terminal velocity and flight path angle are driving parameters in determining the amount of propellant needed for a successful soft land-

TABLE 2. ATMOSPHERIC ENTRY PARAMETERS FOR A MARS MISSION

Altitude, h_e	800,000 feet
Velocity, V_e	12,000 to 16,000 ft/sec
Flight Path Angle, γ_e	-15° to -20°
Ballistic Number, B_{cp}	0.32 slugs/ft^2

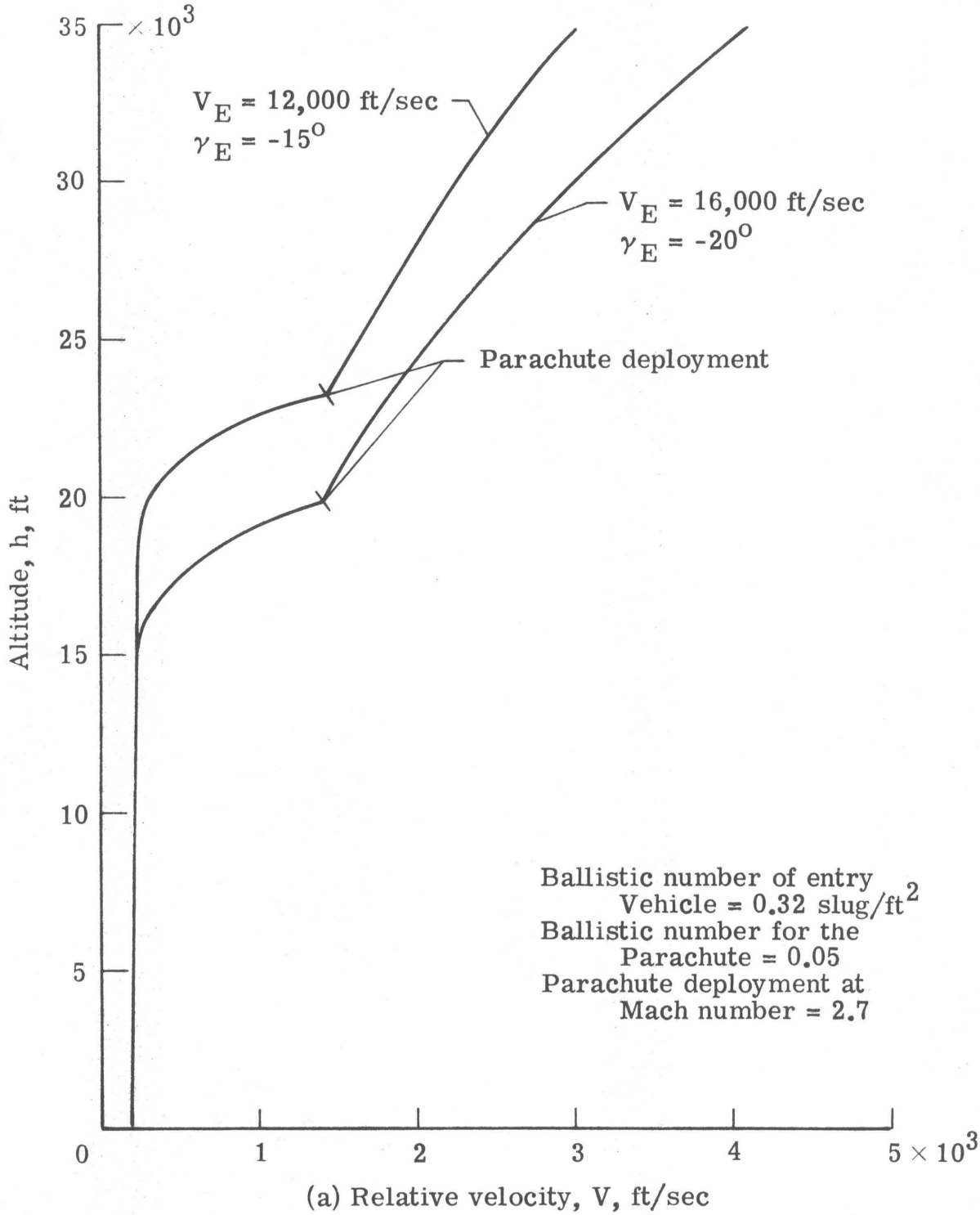

Figure 6.- Terminal descent corridor for entry through VM-8 atmosphere model.

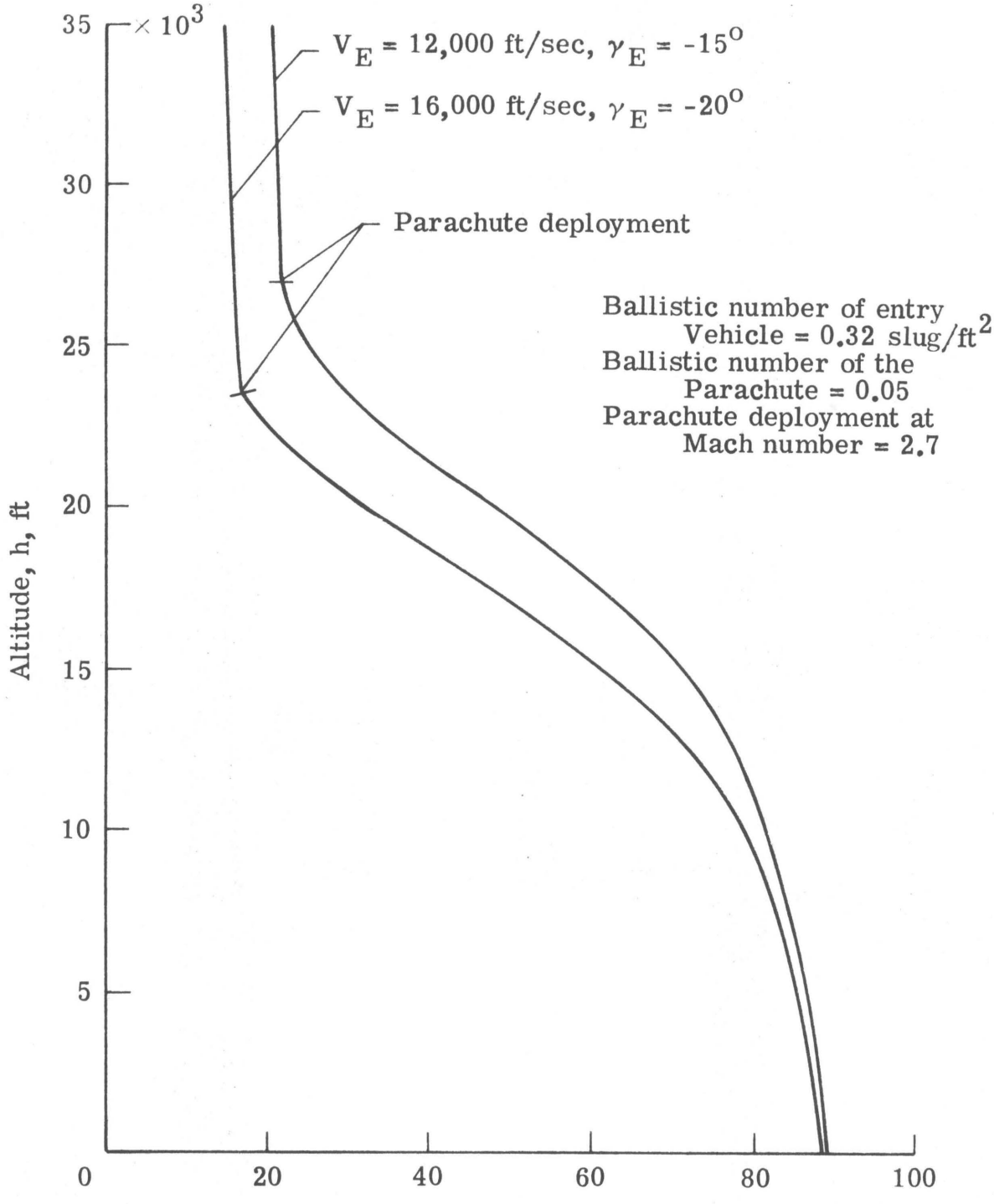

Figure 6.- Continued.

ing. An understanding of the propellant weight sensitivity to retro-descent system ignition velocity, altitude, and flight path angle is important to sizing the parachute.

Referring to figure 6b, we can see that at an altitude of 5000 feet a lander suspended on a parachute will be descending at a flight path angle of approximately 90° or very near vertical descent. The propellant requirements for vertical descent from 5000 feet altitude for a range of retro ignition velocities were determined as follows. In this analysis constant deceleration descent was chosen as a desirable descent mode for convenience and the drag of the lander was considered negligible.

The general equations for the motion of a body under the action of a constant unbalanced force (F) and at constant deceleration are:

$$F = T_r - W \tag{4}$$

$$h - h_i = V_i t + \frac{1}{2} a t^2 \tag{5}$$

$$V = V_i + at \tag{6}$$

where T_r is the thrust acting on the body, W is the weight of the body, V_i is the initial velocity of the body, h_i is the initial altitude of the body, h is the instantaneous altitude, V is the instantaneous velocity, and t is time.

Since descent is considered to be by constant deceleration the deceleration a in equations (5) and (6) is constant. The time for

vertical descent to zero velocity at the surface can be expressed from equation (6) as $t = -V_i/a$. Substituting this expression into equation (5) with $h = 0$

$$-h_i = V_i \left(-\frac{V_i}{a}\right) + \frac{1}{2} a \left(-\frac{V_i}{a}\right)^2 \tag{7}$$

or solving for a

$$a = \frac{V_i^2}{2h_i} \tag{8}$$

Rewriting equation (4) gives

$$\frac{F}{W} = \frac{T_r}{W} - 1 \tag{9}$$

Solving for $\frac{T_r}{W}$ and substituting $F = ma$ and $W = mg_m$ gives

$$\frac{T_r}{W} = \frac{ma}{mg_m} + 1 \tag{10}$$

Substituting equation (8) gives the constant thrust/weight (T_r/W) ratio required for constant deceleration descent to zero velocity at the surface

$$\frac{T_r}{W} = \frac{V_i^2}{2g_m h} + 1 \tag{11}$$

Table 3 summarizes descent times, constant deceleration rates, and thrust/weight required for vertical constant deceleration descents from an altitude of 5000 feet for a range of ignition velocities.

The propellant weight requirement can be calculated and plotted

as a function of ignition velocity. The equation which follows expresses the propellant weight (W_p) as the lander weight at retro ingition (W_i) minus the lander weight at the planet surface (W_f).

$$W_p = W_i - W_f \tag{12a}$$

This equation may be rewritten as

$$\frac{W_p}{W_i} = 1 - \frac{W_f}{W_i} \tag{12b}$$

The rocket equation from rocket engine theory may be written as

$$V_{id} = I_{sp}\, g_c\, \ell n \frac{W_f}{W_i} \tag{13}$$

The Earth's gravitational constant is used since this is the value used in evaluating specific impulse for propellants. This equation relates the ideal change in velocity of a rocket engine while the weight of the engine is decreased from the initial weight (W_i) to the final weight (W_f) and the amount of propellant (with a given I_{sp}) burned is simply $W_p = W_i - W_f$. A spacecraft with a retro descent system can be viewed as a rocket engine. As already defined the spacecraft weight at retro ignition (initial weight of rocket engine) is W_i and the weight after retro descent (final weight of the rocket engine) is W_f.

Equation (13) may be rearranged to give

$$\frac{W_f}{W_i} = \frac{1}{\exp\left(\frac{V_{id}}{I_{sp} g_c}\right)} \tag{14}$$

Substituting equation (14) in equation (12b) gives

$$\frac{W_p}{W_i} = 1 - \frac{1}{\exp\left(\frac{V_{id}}{I_{sp} g_c}\right)} \tag{15}$$

This equation relates the amount of propellant burned to the ideal change in velocity of the rocket engine.

The ideal velocity V_{id} is so called because this velocity change occurs only under the ideal conditions of absence of gravitational force and drag. Assuming the drag on the descending spacecraft negligible gives the ideal velocity as

$$V_{id} = V_i + \Delta V_{gm} \tag{16a}$$

where V_i is the velocity at retro ignition and ΔV_{gm} is the equivalent velocity change which occurs in the presence of Mars gravity (g_m). Therefore equation (16a) may be rewritten as

$$V_{id} = V_i + g_m t \tag{16b}$$

where t is the time of powered descent.

Using the ideal velocity calculated from equation (16b) with V_i and t from table 3 the propellant requirements are given in table 4

and figure 7 is a plot of this data.

TABLE 3. MARS RETRO DESCENT PARAMETERS FOR VERTICAL CONSTANT DECELERATION FROM AN ALTITUDE OF 5000 FEET FOR A BODY OF UNITY MASS

Ignition Velocity (ft/sec)	Retro Descent Time (sec)	Deceleration Rate (ft/sec^2)	Thrust/Weight T_r/W
100	100	1	1.0813
200	50	4	1.3252
300	33.3	9	1.7317
400	25	16	2.3008
500	20	25	3.0325

TABLE 4. MARS RETRO-DESCENT PROPELLANT REQUIREMENTS FOR VERTICAL CONSTANT DECELERATION FROM AN ALTITUDE OF 5000 FEET

Ignition Velocity, V_i (ft/sec)	Propellant Requirement, W_f/W_i (%)	Vid (ft/sec)
100	15.2	1330
200	9.63	815
300	8.44	709.9
400	8.41	707.5
500	8.85	746

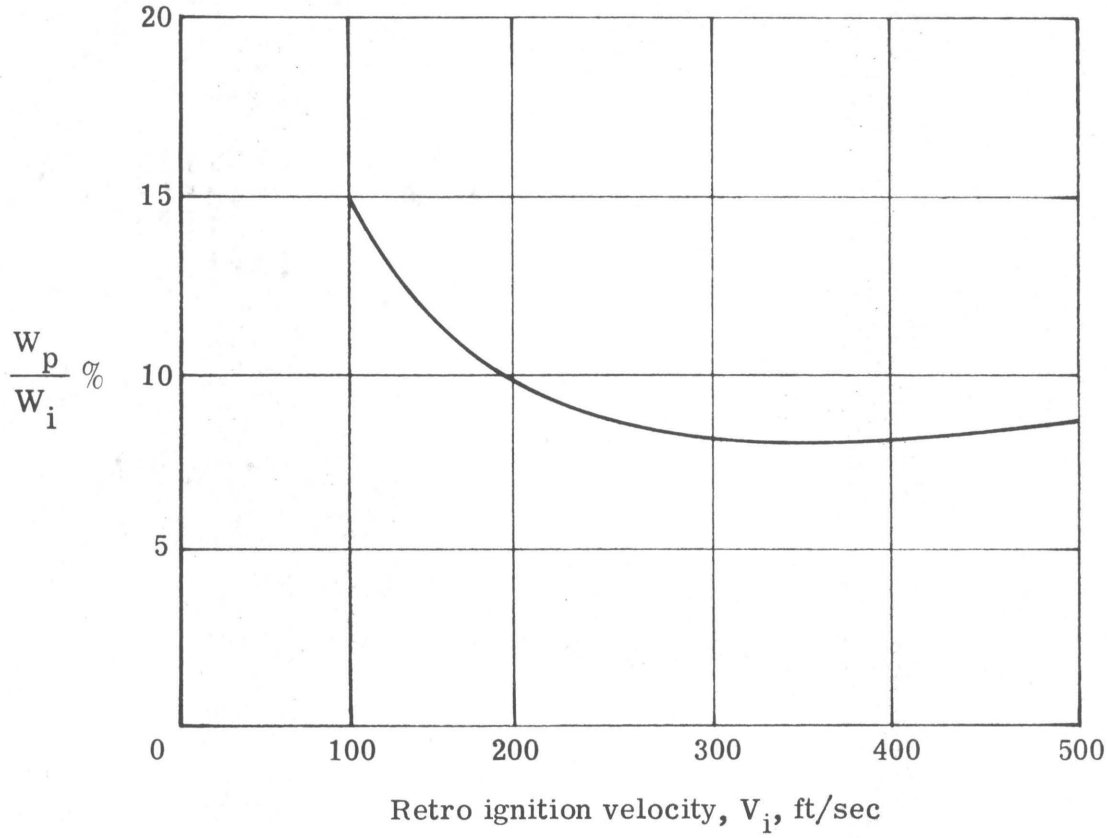

Figure 7.- Propellant requirements for vertical retro descent from an altitude of 5000 feet.

C. Sizing a Decelerator for a Mars Mission

From figure 7 there is little difference in the propellant requirememts for ignition velocities between 280 and 400 ft/sec. Therefore, it is desirable to choose a parachute which will have a terminal velocity between 280 and 400 ft/sec at an altitude of 5000 feet.

The terminal velocity of a parachute lander combination occurs when the drag of the descending parachute is equal to the weight of the parachute lander combination and assuming the drag of the lander negligible. An expression for terminal velocity (V_t) as a function of ballistic number and density may be derived as follows:

Drag = Weight

$$\tfrac{1}{2} \rho V_t^2 C_D A = m g_m \tag{17}$$

$$V_t^2 = \frac{2 g_m (m/C_D A)}{\rho} \tag{18}$$

$$V_t = \sqrt{\frac{2 g_m (m/C_D A)}{\rho}} \tag{19}$$

The terminal velocity of a lander descending on a parachute is reached shortly after parachute deployment. Also, parachute deployment is anticipated to be at an altitude of 15,000 feet or higher. With deployment at or above 15,000 feet the parachute/lander should have reached its terminal velocity by the time it descends to 5000 feet, at which altitude the retro descent engines are initiated.

By rearranging equation (19) an expression for ballistic number ($B_{cp} = \frac{m}{C_D A}$) of the parachute can be obtained as a function of terminal

velocity and density as follows:

$$B_{cp} = \frac{m}{C_D A} = \frac{\rho V_t^2}{2g_m} \tag{20}$$

For a terminal velocity between 250 and 500 feet/second at an altitude of 5000 feet from figure 7 the resulting ballistic number is between 0.056 and 0.143 slugs/ft^2.

For a given lander weight the range of parachute diameter requirements can be defined if the drag coefficient of the parachute is known. The reference area in equation (20) is the area of a circle with a diameter equal to the nominal diameter of the parachute

$$A = \frac{\pi D_o^2}{4}$$

The ballistic number has already been defined as

$$B_{cp} = \frac{m}{C_D A}$$

Combining and rearranging these two expressions gives an expression for the parachute nominal diameter as a function of the system mass, the parachute drag coefficient, and the ballistic number as follows:

$$D_o = \sqrt{\frac{4m}{\pi C_D B_{cp}}}$$

or

$$D_o = \sqrt{\frac{4}{\pi C_D B_{cp}} \frac{W}{g_m}}$$

For a range of lander weights and a typical decelerator drag coefficient of 0.50 the resulting required parachute diameters are given in figure 8 for ballistic numbers from 0.056 to 0.143 slugs/ft^2.

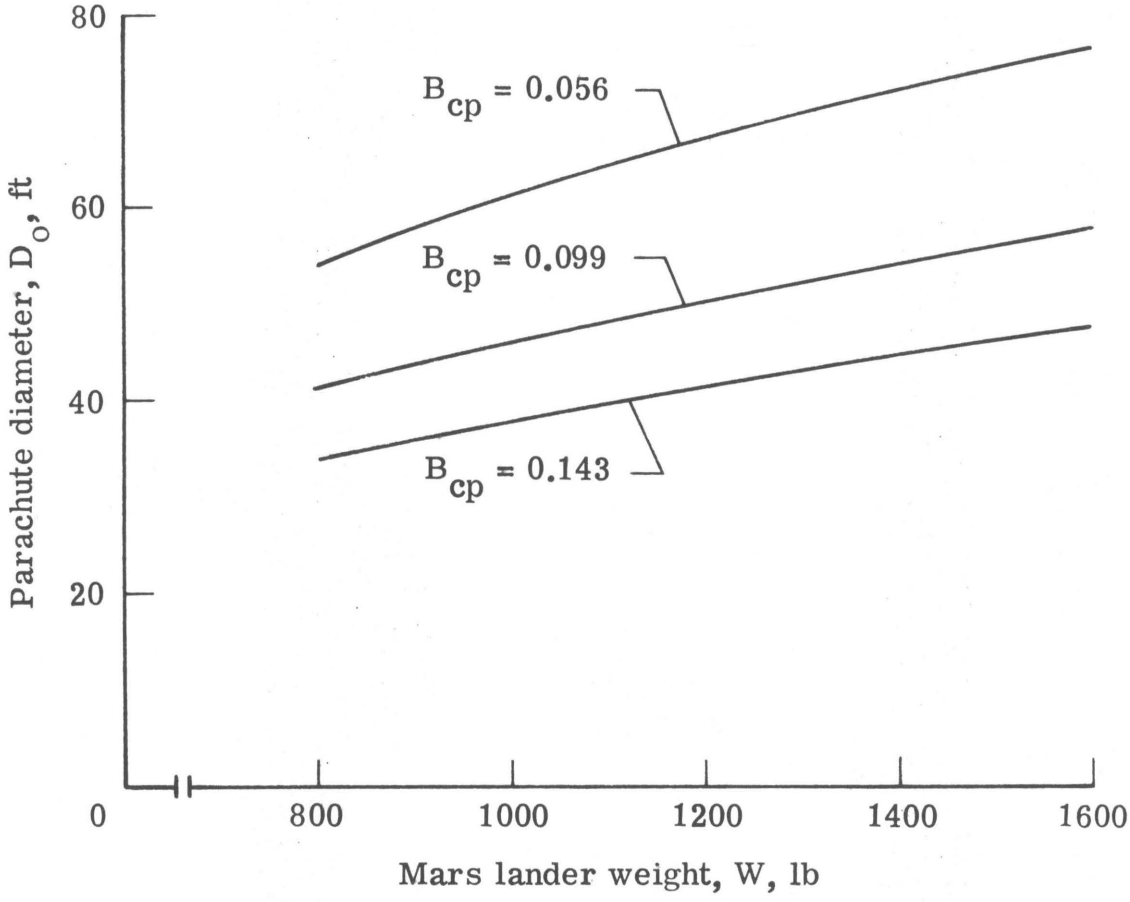

Figure 8.- Parachute diameter requirements as a function of lander weight for a range of ballistic numbers.

IV. MODEL LAWS GOVERNING PARACHUTE PERFORMANCE IN MARTIAN ENVIRONMENT

Most landing systems for the soft landing of spacecraft on Earth or on other planets with a reasonably cool atmosphere consider the use of parachutes for a part of the terminal descent. The aerodynamic and dynamic performance characteristics of subsonic and supersonic parachutes are influenced by the air density, wind shear layers in the atmosphere, and the gravitational constant. The Martian atmosphere in conjunction with the Martian gravitational constant impose upon the functioning of the parachute conditions which are quite different from those existing on Earth. Helmut G. Heinrich (reference 1) has developed model laws to allow prediction of parachute performance on Mars based on experimental results in the Earth's atmosphere.

Model laws concerning the dynamic and aerodynamic conditions of bodies entering the atmosphere of other planets are considered in reference 17. This study and its references consider very thoroughly the various influences upon rigid bodies. However, flexible parachutes, built out of porous woven screens, introduce a new aspect, namely the aerodynamic drag of the porous canopy material. A possible variation of this drag will be reflected in the parachute rate of descent. Furthermore, it is known that the dynamic stability behavior of parachutes is strongly influenced by the steady state aerodynamic coefficients which in turn depend on mass flow through the canopy. The mass flow, however, is

related to the air resistance of the canopy material, which is basically a function of the Mach, Reynolds, and Knudsen numbers, with the dimensions of the screen openings being the characteristic length (references 2 and 3).

Reference 3 shows the influence of the Reynolds number inasmuch that, under the condition of constant pressure differential, the effective porosity of a woven screen decreases when the air density is lowered. This of course affects the steady state aerodynamic coefficients.

Experiments have shown that the stability of solid cloth parachutes at high altitude and under identical pressure loading is not as good as indicated by wind tunnel results and theoretical predictions. The parachutes also inflate faster and develop greater opening shock loads at high altitude than at sea level.

In view of these experiences, the effective porosity must be considered to be the most fundamental and influential parameter of parachute performance.

For any given altitude the density of the Martian atmosphere is much lower than that of the Earth's atmosphere. Therefore, at the same altitude and under the same pressure loading, the effective porosity of any porous screen is lower on Mars than on Earth, and under these conditions identical parachutes may show a completely different behavior. However, the known relationship between aerodynamic parachute coefficients and effective porosity is the link which permits the prediction of parachute performance in the Martian atmosphere based on observations made on Earth, and in view of this concept model laws can be establish-

ed in which the effective porosity is the independent variable.

In reference 1 the effective porosity on the Martian surface was estimated to be 15 to 30 percent of that on the Earth's surface. This variation is primarily caused by the low density; but Martian porosity conditions can be simulated on Earth when the pressure ratio and the air density are duplicated. This means that pertinent experiments on Earth need to be performed with the identical pressure ratio, in the so-called simulation altitude and this concept provides the foundation for the proposed model laws.

For supersonic parachutes, the Reynolds number influence is weak while the Mach number is the dominating parameter. Therefore, model experiments with supersonic parachutes require primarily the duplication of Mach number. The density is important since this will determine the actual parachute forces.

It has been shown by Henn (reference 14) and other authors that for the dynamic stability behavior the aerodynamic coefficients, the distribution of mass about the center of gravity of the system, the apparent mass of the parachute, and the gravitational constant are the most influential terms. The dynamic stability behavior of descending parachutes may be judged by comparing their angular acceleration caused by the aerodynamic moment. Therefore, model experiments can be considered significant when the angular accelerations are the same.

In the first approximation the moment equation for an oscillating parachute can be written as (see figure 9)

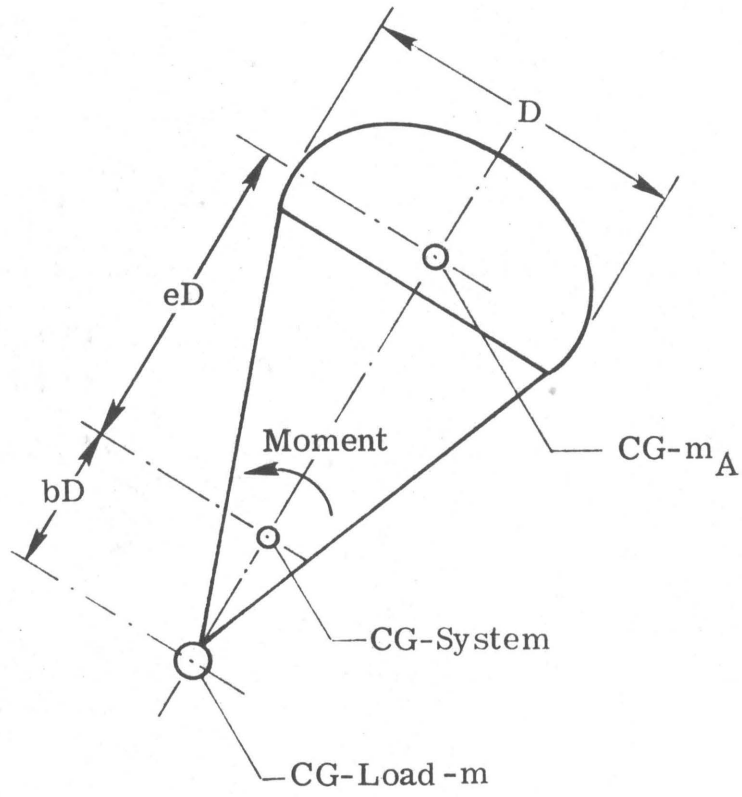

Figure 9.- Schematic of an oscillating parachute-payload system.

$$(m_A e^2 D^2 + mb^2 D^2) \frac{d\omega}{dt} = C_M D \frac{\rho V^2}{2} \frac{\pi D^2}{4} \tag{21}$$

An equilibrium speed or velocity can be defined when the drag force equals the inertial forces from gravitational acceleration

$$V^2 = \frac{mg}{C_D \frac{\rho}{2} \frac{\pi}{4} D^2} \tag{22}$$

Substituting the equilibrium speed into the moment equation gives

$$(m_A e^2 D^2 + mb^2 D^2) \frac{d\omega}{dt} = \frac{C_M}{C_D} Dmg \tag{23}$$

The angular acceleration is then

$$\frac{d\omega}{dt} = \frac{C_M}{C_D} \frac{mg}{D(m_A e^2 + mb^2)} \tag{24}$$

An inspection will show that $m_A << m$ and the equation reduces to

$$\frac{d\omega}{dt} = \frac{C_M}{C_D} \frac{g}{Db^2} \tag{25a}$$

or

$$\alpha = \frac{C_M}{C_D} \frac{g}{Db^2} \tag{25b}$$

This equation may be qualified for Earth and Mars operations by means of the subscripts e and m respectively as follows:

$$\alpha_e = \frac{C_M}{C_D} \frac{g_e}{D_e b^2} \tag{26a}$$

$$\alpha_m = \frac{C_M}{C_D} \frac{g_m}{D_m b^2} \tag{26b}$$

Assuming the aerodynamic coefficients C_M and C_D are identical, the ratio is then

$$\frac{\alpha_e}{\alpha_m} = \frac{g_e}{g_m} \frac{D_m}{D_e} \tag{27}$$

Considering this ratio to be unity and since $g_e/g_m = 1/0.38$

$$\frac{D_m}{D_e} = 0.38$$

In order to assure the similarity of the steady-state aerodynamic coefficients, the differential pressure on the Earth and Martian parachute should be identical, which is also the condition for rate of descent simulation. This can be expressed as follows:

$$V_e^2 = \frac{m_e g_e}{\frac{\rho_e}{2} C_D \frac{\pi D_e^2}{4}} \tag{28a}$$

and

$$V_m^2 = \frac{m_m g_m}{\frac{\rho_m}{2} C_D \frac{\pi D_m^2}{4}} \tag{28b}$$

The ratio is then

$$\frac{V_e^2}{V_m^2} = \frac{m_e}{m_m} \frac{g_e}{g_m} \frac{D_m^2}{D_m^2} \tag{29}$$

We have already defined $D_m/D_e = 0.38$.

Therefore,

$$\frac{V_e^2}{V_m^2} = \frac{m_e}{m_m} \frac{g_e}{g_m} (0.38)^2$$

With $g_e/g_m = 1/0.38$ and requiring the velocity ratio to be unity gives

$$\frac{m_m}{m_e} = 0.38$$

The differential pressure ΔP can be defined as follows:

$$\Delta P = \frac{mg}{\frac{\pi D^2}{4}} \tag{30}$$

This equation can be qualified for Earth and Mars respectively with the subscripts e and m. The following ratio results

$$\frac{\Delta P_e}{\Delta P_m} = \frac{m_e}{m_m} \frac{g_e}{g_m} \left(\frac{D_m}{D_e}\right)^2 \tag{31}$$

Using results already obtained

$$\frac{\Delta P_e}{\Delta P_m} = 1$$

which together with $\rho_e/\rho_m = M_e/M_m = 1$ satisfies the concept of scaling.

The results of these considerations can be summarized as follows:

$$D_e/D_m = 1/0.38 = 2.63$$

$$m_e/m_m = 1/0.38 = 2.63$$

$$\alpha_e/\alpha_m = 1$$

$$V_e/V_m = 1$$

$$\Delta P_e/\Delta P_m = 1$$

and these are proposed model laws for Earth testing in view of parachute operations for Mars.

V. PARACHUTE DESCRIPTION

A disk-gap-band type parachute was selected for the flight test. The disk-gap-band design was originated in 1963 to provide a highly stable and high drag parachute for meteorological rocket applications at altitudes in excess of 100,000 feet. The disk-gap-band parachute is simple in design, has a low packing volume, and is fabricated in the form of a short cylinder having a closed end (figure 10). The short wall of the cylindrical portion of the canopy is formed by the band and the closed end of the cylinder is formed by the disk portion of the canopy. The parachute canopy is ventilated with a wide peripheral slot or gap between the disk and the band. Although the inflated shape of the parachute canopy is generally never the same as the constructed shape, the disk-gap-band parachute does retain some shape change at the intersection of the disk and gap portions of the canopy in the inflated conditions. The disk-gap-band parachute was one of three configurations flight tested in a low-density environment in other NASA parachute programs including the Planetary Entry Parachute Program (PEPP); the Supersonic Planetary Entry Decelerator Program, Part I (SPED I); and the Supersonic High Altitude Parachute Experiments (SHAPE). The nominal diameter of the disk-gap-band parachute was selected as 55 feet. From the PEPP, SPED I, and SHAPE parachute programs, the steady state drag coefficient has been estimated to be approximately 0.53 which is slightly more than the assumed C_D for figure 8 in Chapter III.

A. Geometric Description

The nominal diameter of the parachute was selected to be 55 feet

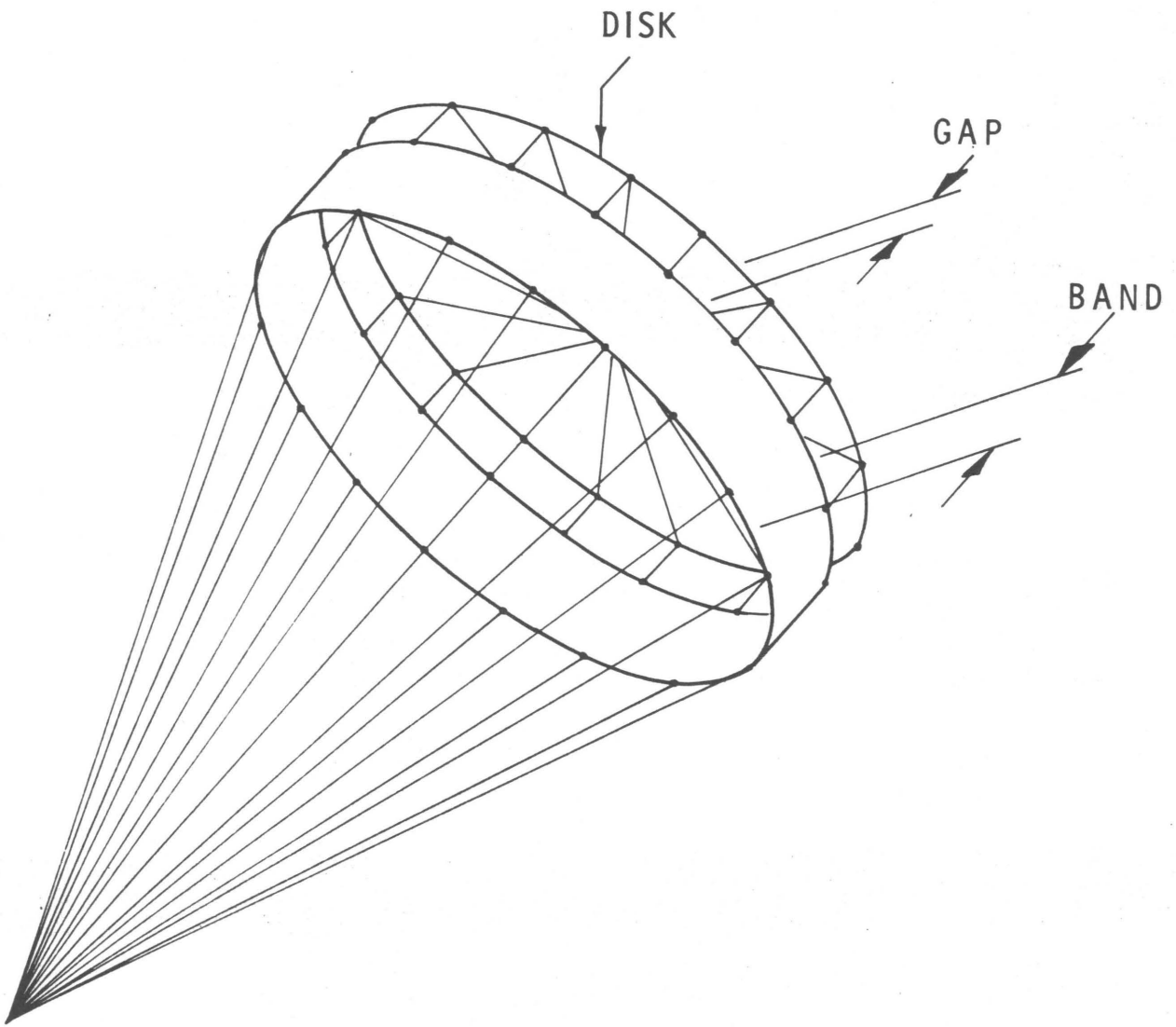

Figure 10.- Constructed geometric shape of the disk-gap-band parachute.

with a resulting nominal surface area of 2376 ft^2. The disk or center part of the canopy, which included the vent area, had a surface area equal to 53 percent of the nominal surface area. The disk was a regular polygon with 42 sides (nearly a circle). The band part of the canopy, with a surface area equal to 35 percent of the nominal surface area, was a right circular cylinder with a circumference equal in length to the perimeter of the disk portion of the canopy. The disk and the band were separated by a gap or open area equal to 12 per cent of the nominal surface area. There was also a vent at the center of the disk with an open area equal to 0.5 percent of the nominal surface area. The total ventilated area or geometric porosity of the canopy was therefore 12.5 percent of the nominal surface area. The dimensional details are presented in table 5.

B. Gore Dimensions

The constructed shape of a single gore with dimension and area labels are illustrated in figure 11. Based on a geometric porosity of 12.5 percent, the gore dimensions and areas were calculated as follows:

The nominal surface area is equal to the area of a circle having a diameter equal to the nominal diameter of the parachute.

$$S_o = \frac{\pi}{4} D_o^2 \tag{32}$$

The number of gores (N) was 42. The included angle of the gore was calculated from

$$\theta_g = \frac{2\pi}{N}$$

Table 5. DIMENSIONS AND AREAS FOR A DISK-GAP-BAND PARACHUTE

Nominal diameter, D_o	55 ft
Nominal surface area, $S_o = \frac{\pi D_o^2}{4}$	2375.8 ft^2
Disk area, $S_d = 0.53\ S_o$	1259.2 ft^2
Disk diameter, D_d	40.05 ft
Disk circumference	125.79 ft
Gap area, $S_g = 0.12\ S_o$	285.1 ft^2
Gap width, w_g	2.27 ft
Band area, $S_b = 0.35\ S_o$	831.5 ft^2
Band width, w_b	6.61 ft
Vent area, $S_v = 0.005\ S_o$	11.88 ft^2
Vent diameter, D_v	3.89 ft
Suspension line length, ℓ	55 ft

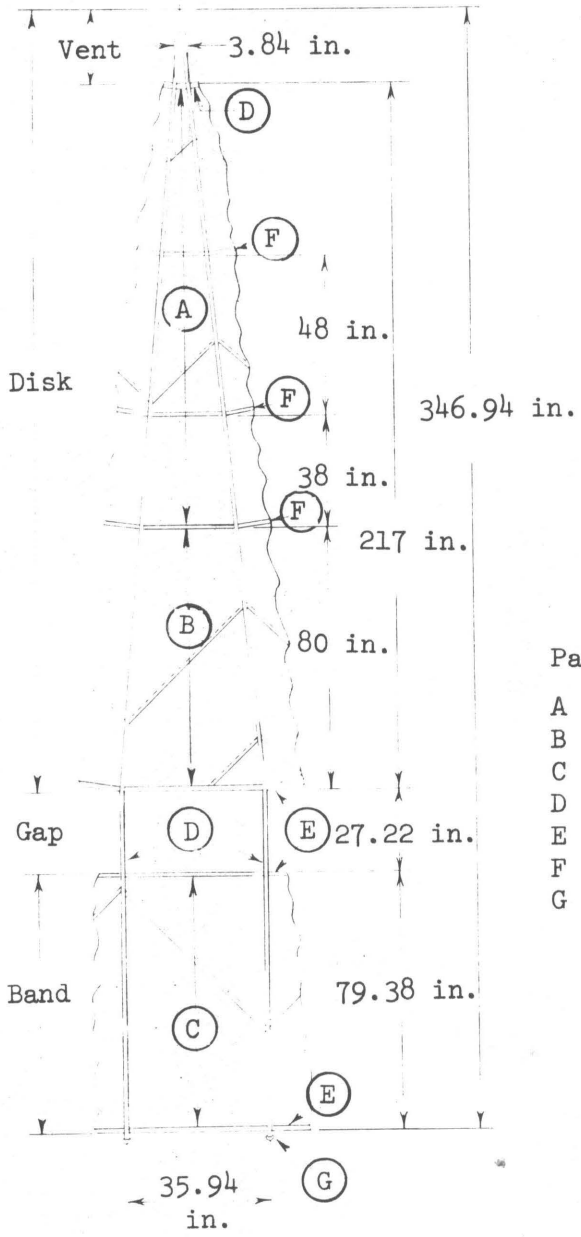

Parachute materials

A Nomex cloth, disk area
B Dacron cloth, disk area
C Dacron cloth, band area
D Radial and vent tapes
E Hem tapes
F Reinforcement tapes
G Suspension lines

Figure 11.- Parachute gore details.

and the nominal area per gore was calculated by

$$S_{og} = \frac{S_o}{N} \tag{33}$$

The disk, gap, band, and vent areas per gore were calculated as follows:

$$S_{dg} = 0.35\ S_{og}$$
$$S_{gg} = 0.12\ S_{og}$$
$$S_{bg} = 0.35\ S_{og}$$
$$S_{vg} = 0.005\ S_{og}$$

Each disk gore had a triangular shape and the area was calculated from the height and included angle as follows:

$$S_d = \tfrac{1}{2}\ H_d\ w_{dg} \tag{34}$$
$$S_d = \tfrac{1}{2}\ H_d\ (H_d \sin \theta_g) \tag{35}$$

and for small angles

$$S_d = \tfrac{1}{2}\ H_d^2\ \theta_g \tag{36}$$

Solving for the height gives

$$H_d = \sqrt{\frac{2S_d}{\theta_g}} \tag{37}$$

Also, from geometry

$$w_{bg} = w_{gg} = w_{dg} = \frac{2S_d}{H_d} \tag{38}$$

The height of the band was calculated from

$$H_b = \frac{S_b}{w_{bg}} \tag{39}$$

The height of the gap was calculated

$$H_g = \frac{S_g}{w_{bg}} \tag{40}$$

The height of the vent was determined in the same manner as the disk height

$$H_v = \sqrt{\frac{2S_v}{\theta_g}} \tag{41}$$

and also

$$w_{vg} = \frac{2S_v}{H_v} \tag{42}$$

to allow additional gore curvature for stress relief in the vent area 10 percent fullness was added.

$$w_{vg} = w_{vg}(1.1)$$

The new apex angle was determined

$$\text{Tan } \frac{\theta_g}{2} = \frac{(w_{dg} - 1.1\ w_{vg})}{2(H_d - H_v)} \tag{43}$$

With the new apex angle a new contruction height was calculated

$$H_c = \frac{w_{dg}/2}{\text{Tan } (\theta_g/2)} \tag{44}$$

The gore areas and dimensions are presented in table 6.

TABLE 6. GORE DIMENSIONS AND SURFACE AREAS FOR A 55 FEET D_o DISK-GAP-BAND PARACHUTE

Gore Disk Included Angle, θ_{dg}	8.57^{o}
Gore Surface Area, S_{og}	8145.6 in^2
Gore Disk Surface Area, S_{dg}	4317.2 in^2
Gore Gap Surface Area, S_{gg}	977.5 in^2
Gore Band Surface Area, S_{bg}	2851.0 in^2
Gore Vent Area, S_{vg}	40.7 in^2
Disk Radius, R_d	240.3 in
Disk Base Width, w_d	35.9 in
Gap Height, H_g	27.2 in
Gap Width, w_g	35.9 in
Band Height, H_b	79.4 in
Band Width, w_b	35.9 in
Vent Radius, R_v	23.3 in
Vent Base Width, w_{vg}	3.8 in

VI. PARACHUTE DESIGN

The importance of knowing the loads and stresses in parachutes lies in the necessity for minimizing the weight of the canopy and, with it, the required packing volume. The loads and stresses in a canopy are caused by aerodynamic loads acting on and between the various structural components. The loads and stresses are both dynamic and static. The severe loads and stresses usually exist for a comparatively short time during the period of attaining full inflation.

Although the structure of a parachute differs considerably in many respects from more common load-bearing structures, a stress analysis still requires a knowledge of three basic items: the shape and fabrication details of the structure, the manner and magnitude of application of the loads, and the characteristics of the structural material. The load-carrying elements are fabric materials that have little stiffness and, therefore, can take no bending loads. Loads are resisted by tension in the members.

A rigorous stress analysis for a canopy is extremely complicated since maximum stresses occur during the opening process, which is the period of rapidly changing shape and load. The determination of stresses in a canopy is essentially an aeroelastic problem, insofar as the cloth and suspension lines may be said to be elastic. Experience with structural failures in canopies indicates that the critical stresses occur most often during opening-shock loading. The approach used in this stress analysis is an approximation to the actual dynamic case.

The loads and stresses were calculated assuming the parachute statically loaded by the opening shock load.

Approximate empirical methods (described in reference 4) were used to calculate the decelerator loads and stresses. The probable maximum opening loads were estimated by computational procedures derived from the so-called "opening-shock-factor" method. The method provides a simplified analytical approach for quick and dependable results when carefully applied and when the pertinent empirical data are available. Data on measured opening loads, drag areas, system weight, and flight-test conditions were available from previous flight tests of the disk-gap-band parachute configuration. A non-rigorous empirical method (reference 4) was used for the stress analysis of the parachute structure. Critical loading of canopy fabric is not amenable to analytical treatment because the highest stresses result from fluttering and whipping ("flagging"). A major problem in the calculation of stresses is the lack of knowledge of the magnitude of transient aerodynamic pressures and forces.

A. Opening and Design Loads

The opening-load-factor method was used for predicting the opening load of the disk-gap-band parachute. The maximum expected opening load was calculated using the following equation

$$F_o = X\, C_D\, q\, S_o \qquad (45)$$

where q is the free stream dynamic pressure at the fully opened condition. The maximum opening load was calculated to be 34,870

pounds based on a dynamic pressure of 21 lb/ft^2, a nominal steady state drag coefficient of 0.53, and an opening load amplification factor of 1.32. To allow for errors in the programmed deployment sequence, the maximum opening design load was based on a dynamic pressure of 23 lb/ft^2 or a maximum design load of 38,230 pounds.

In the design and stress analysis certain assumptions were made for the calculations. The maximum opening design load was assumed symmetrically distributed to the suspension lines and radial tapes.

With the maximum design load equally distributed, the load in each suspension line and radial tape can easily be calculated. Since the radial tapes are extensions of the suspension lines across the parachute canopy the load in the radial tape is equal to the load in the suspension line at the connection between the two structural components. The load in each radial tape and suspension line was calculated as follows:

$$P_{RT} = P_{SL} = F_o/N \qquad (46)$$

$$= 38{,}230 \text{ lb}/42$$

$$= 910.2 \text{ lb}$$

The canopy cloth strength requirement is the most uncertain item relating to the parachute stress analysis. An empirical method was used to calculate the stress in the canopy cloth. From membrane theory an expression for the circumferential unit load, or "hoopstress", in an all ellipsoidal surface of revolution, P_c, can be written as

$$P_c = KPr \tag{47}$$

where K is 1.0 for simple curvature (conical, cylindrical) and 0.5 for a spherical surface.

The uniform pressure was calculated by assuming the opening load distributed uniformly over the cloth surface area. The shape of the inflated disk-gap-band can best be described with the disk approaching a hemispherical shape and the band approaching a cylindrical or conical shape. This points out the question of what value of K should be used when applying equation (47). Since the more conservative case is cylindrical or conical, a value of K = 1.0 was used. The radius of curvature was assumed as one half of the projected diameter, D_p, which is two-thirds of the nominal diameter, D_o, for a disk-gap-band parachute. Therefore,

$$P = \frac{F_o}{S_d + S_b} \tag{48}$$

and

$$r = \frac{D_p}{2} = \frac{D_o}{3} \tag{49}$$

which gives

$$P_c = \frac{F_o}{S_d + S_b} \cdot \frac{D_o}{3} \tag{50}$$

$$P_c = 27.98 \text{ lb/in}$$

B. Aerodynamic Heating

An analysis was made of the aerodynamic heating environment for the parachute (reference 5). One of the conclusions from this analysis was

that equilibrium surface temperatures in excess of 400°F (figure 12) might be expected during the flight test.

C. Structural Design Factors

In order to conform with generally accepted practice in structural design and analysis of textile structures, the design-factor data given in reference 4 was used. The approach used is as follows:

(1) A strength reducing factor, A_p, was applied to rated strength levels of fabric material to account for losses of strength caused by such known phenomena as abrasion, fatigue, sterilization, joint efficiency, nonuniform loading, and line convergence.

(2) A safety factor (S.F.) was applied to the limit load to determine the ultimate load and account for uncontrollable variations in material properties and degradations resulting from manufacturing processes.

From these two factors an overall structural design factor (D.F.) was determined

$$D.F. = \frac{S.F.}{A_p} \tag{51}$$

A tabulation of the strength-reducing factors, safety factors, and overall design factors is presented in table 7.

D. Component Meterial Selection

The data in sections A, B, and C were used in selection of materials and required strengths. The required rated strength of the

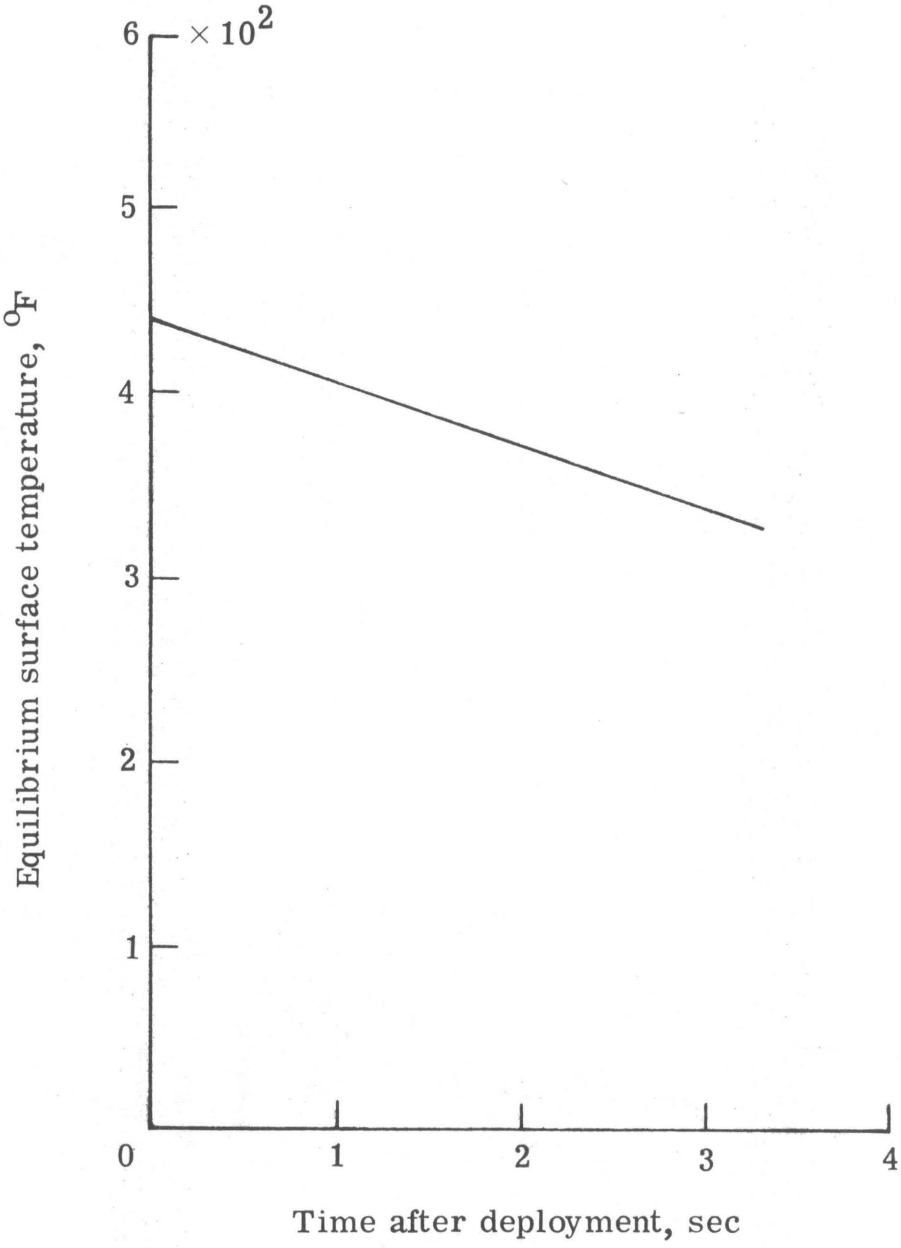

Figure 12.- Equilibrium surface temperatures for disk-gap-band parachute flight test on Earth.

TABLE 7. STRUCTURAL DESIGN FACTORS

	Suspension Lines	Radial Taper	Canopy Cloth		
			nomex	2.6 oz dacron	2.0 oz dacron
Strength Reducing Factors					
Abrasion, c	0.96	0.96	0.96	0.96	0.96
Sterilization, n	NA	NA	NA	NA	NA
Line Convergence, d	.95	.95	NA	NA	NA
Asymmetrical heading, f	.95	.95	.95	.95	.95
Joint Efficiency, b	.90	.80	.80	.80	.74
A_p = cndfb	.78	.69	.73	.73	.67
Safety Factor, S.F.	1.5	1.5	1.5	1.5	1.5
Design Factor $D.F. = \frac{S.F.}{A_p}$	1.92	2.16	2.06	2.06	2.22

structural components was determined by multiplying the maximum expected load (P_{max}) by the design factor.

$$P'_R = (D.F.)\ P_{max} \tag{52}$$

The required strength of the suspension lines and radial tapes and the rated strength of the materials used are presented in table 8.

Three different types of cloth were selected. This selection was guided by minimum weight, required strength, and aerodynamic heating on a previous flight test (reference 6). The portion of the parachute canopy damaged on the reference flight test is shown in figure 12. Based on this evidence and the aerodynamic heating analysis (figure 11), nomex cloth which has good strength retention at high temperatures was used in the center portion of the disk. A 2.6 oz/yd^2 dacron cloth was selected for use in the outer portion of the disk. A 2.0 oz/yd^2 dacron cloth was used in the band to minimize weight. Also, on previous flight tests of disk-gap-band parachutes where cloth damage was experienced, the damage occurred in the disk. Therefore, a minimum weight cloth was selected as acceptable for the band. The three types of cloth and their respective required strengths and rated strengths are shown in table 8.

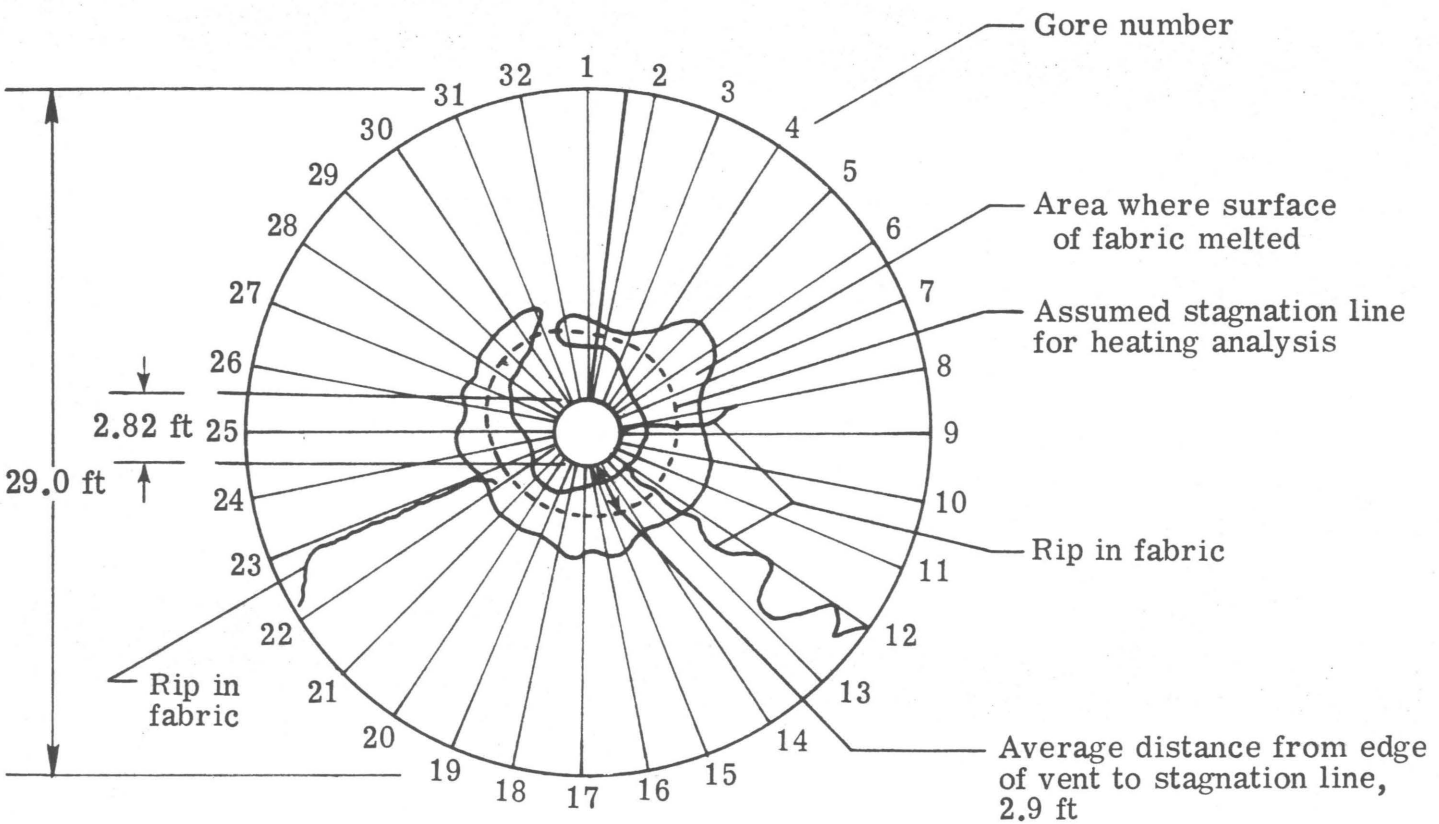

Figure 13.- Features of the disk of the 40-foot nominal diameter disk-gap-band parachute subsequent to Mach number 3.31-deployment flight.

TABLE 8. COMPONENT MATERIAL STRENGTHS FOR A DISK-GAP-BAND PARACHUTE

	Maximum Design Load	Design Factor	Required Rated Strength	Manufactured Rated Strength
Suspension Lines	910 lb	1.92	1748 lb	2000 lb
Radial Tapes	910 lb	2.16	1966 lb	2000 lb
Canopy Cloth				
Nomex	27.98 lb/in	2.06	57.63 lb/in	120 lb/in
2.6 oz dacron	27.98 lb/in	2.06	57.63 lb/in	90 lb/in
2.0 oz dacron	27.98 lb/in	2.22	62.12 lb/in	66 lb/in

VII. FLIGHT TEST

A flight test was conducted with a disk-gap-band parachute having a nominal diameter of 55 feet and located at a trailing distance of 4.4 forebody diameters behind a 15-feet diameter bluff body planetary entry type aeroshell and attached instrumented payload. The parachute and payload aeroshell flight configuration is illustrated in figure 14. The major objective of this flight test was to investigate the deployment performance of a full-scale supersonic decelerator behind a simulated model of a Mars entry capsule.

The parachute diameter and payload weight can be compared with the Mars requirements established by figure 8 in Chapter III. The test parachute had a nomianal diameter of 55 feet and the payload weight was 1472 pounds. This results in a ballistic number for the parachute payload combination of 0.095. This is near the upper limit of the lander weights considered, near the middle of the ballistic number range, and near the middle of the range of diameters considered in figure 8.

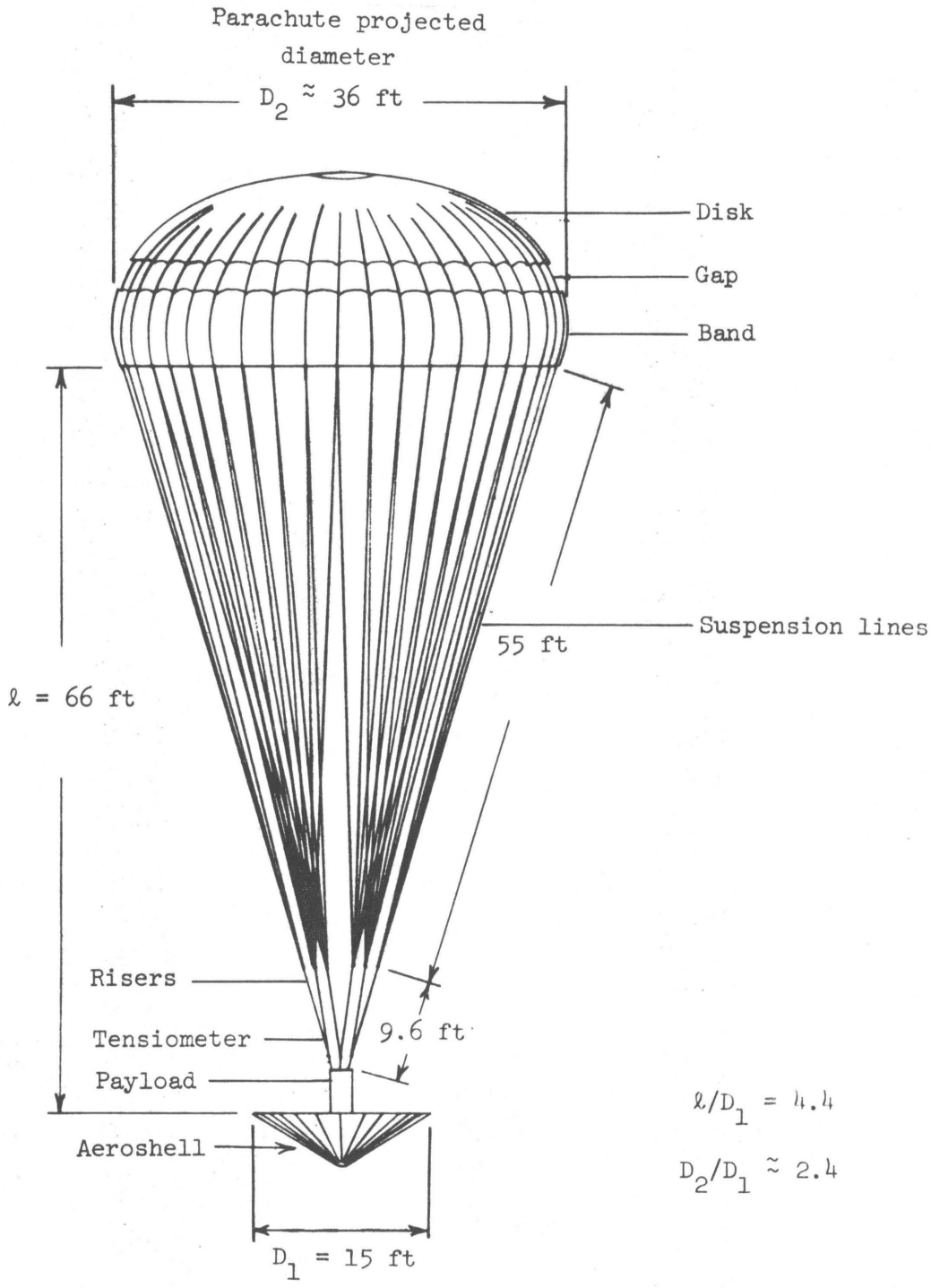

Figure 14.- Sketch of parachute and aeroshell-payload configuration.

A. Test System Description

The launch vehicle consisted of a single stage Castor rocket motor with two Recruit launch assist rocket motors, an instrumented payload with an attached erectable forebody (aroshell), and a jettisonable nose cone as shown in figures 15 and 16. A photograph of the rocket vehicle in the launch position is presented as figure 17. The weights at the various flight-conditions of time, velocity, Mach number, and altitude are presented in table 9.

The umbrella-like erectable aeroshell was maintained in the folded position until the re-entry portion of the flight-test as shown in figure 18. In the erected position the aeroshell formed a 120° total angle blunted cone with a maximum diameter of 15 feet. An attitude control system was utilized to reorient the vehicle attitude in a downward direction at flight apogee (as shown in figure 18) and to hold this position so that it would be pointed in the direction of the flight path at the time of erection of the aeroshell forebody. After erection of the aeroshell and jettisoning of the nose cone the attitude control jets were no longer operational. It was planned that spacecraft would then be maintained in the proper flight attitude by aerodynamic forces acting on the aeroshell forebody.

A redundant command receiver system in the instrumented payload section was utilized to perform three of the system functions shown in figure 18. These system functions commanded from the ground control center were the:

(1) erection of the aeroshell forebody,

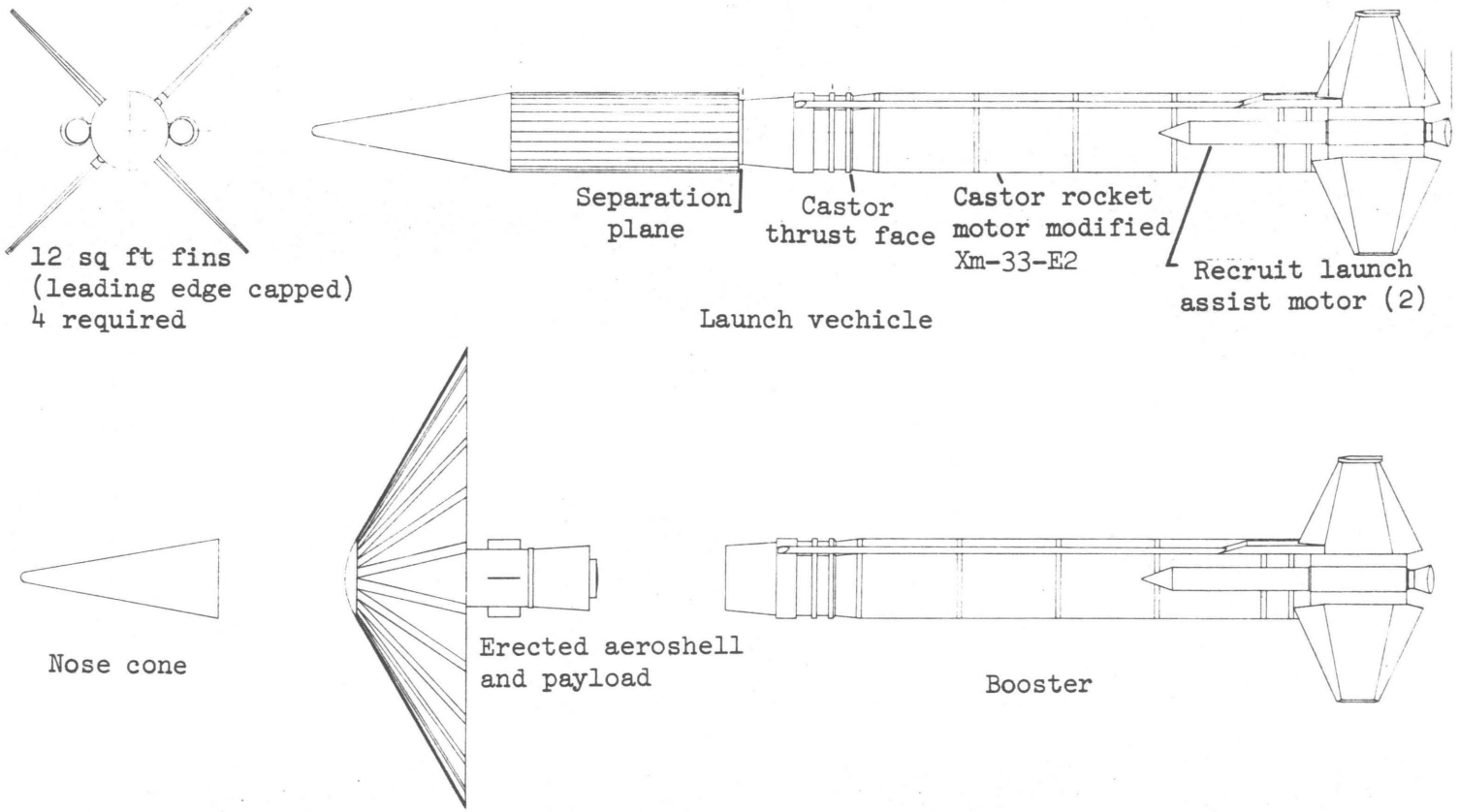

Figure 15.-Sketch of SPED-II launch vechicle and separated parts including erected aeroshell and payload.

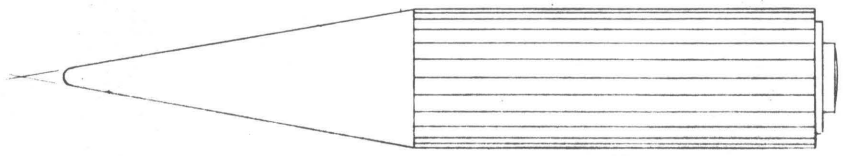

(a) Folded spacecraft.

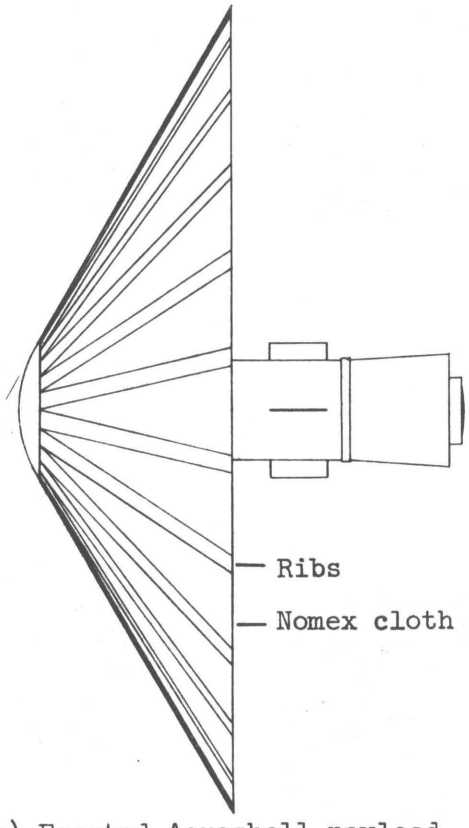

(b) Erected Aeroshell-payload.

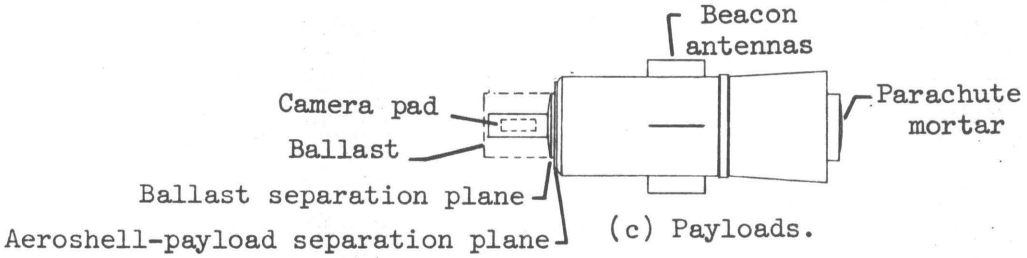

(c) Payloads.

Figure 16.- Sketches of folded aeroshell, erected aeroshell-payload, and payload alone.

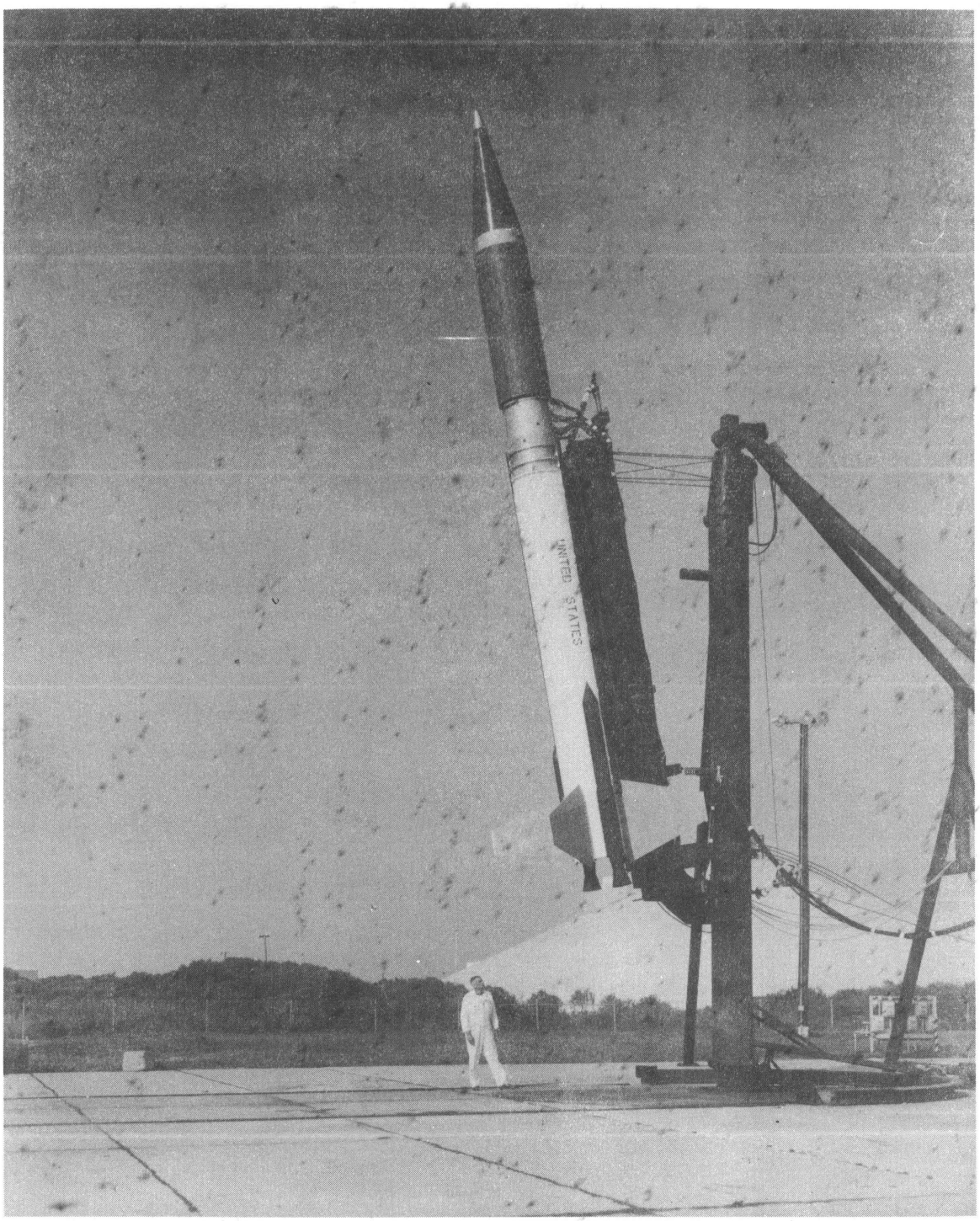

L-70-258

Figure 17.- Test vehicle on launcher.

TABLE 9. CONFIGURATION WEIGHTS

Configuration	Weight lb
Total vehicle at launch	14,745
Total vehicle after burnout of motors	6783
Spacecraft after motor and adapter section separation	3062
Spacecraft after aeroshell erection and nose cone separation	2637
Spacecraft and parachute system after parachute ejection and separation of the mortar sabot	2631
Payload and parachute system after aeroshell separation	1472
Payload and parachute system after ballast separation	694

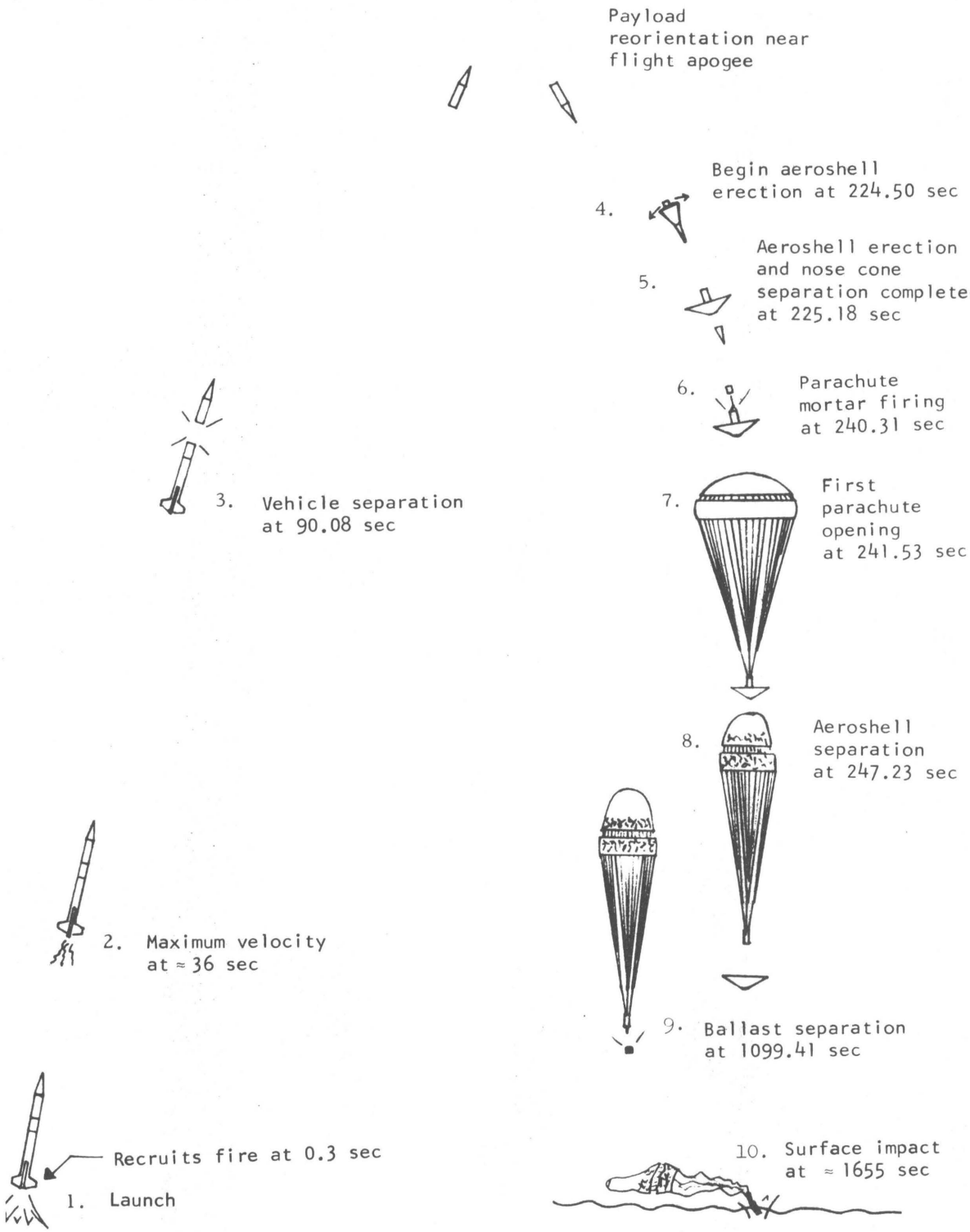

Figure 18.- Earth flight test sequence of events.

(2) firing of the mortor system for deployment of the test parachute, and

(3) activation of the payload ballast release mechanism to reduce system weight and facilitate recovery of the payload.

The test parachute was stored in and deployed by a mortor system located at the aft end of the payload. The mortar volume available for storage of the packed parachute was 3.12 ft^3. The expected in-flight pack ejection velocity, based on several pre-flight ground deployment tests, was about 154 ft/sec for a 127-pound parachute pack assembly.

A complete description of the launch vehicle, the erectable aeroshell, the attitude control system, and other vehicle associated hardware and an evaluation of their performance may be found in reference 7.

B. Payload Instrumentation

The payload instrumentation utilized to acquire data for the evaluation of the test parachute performance included: the three tensiometers located on the aft bulkhead of the payload for direct measurement of loads in the parachute attachment risers, accelerometers along the three mutually perpendicular body axes, an attitude reference system, and four cameras. Data from the accelerometers, the tensiometers, and the attitude reference system were telemetered to ground recording stations whereas the camera film was obtained after recovery of the payload from the impact area.

The three tensiometers located on the aft bulkhead were of the electrical strain gage type with each calibrated from 0 to 16,000 pounds. The tensiometers (see figure 19) were attached to the payload by means

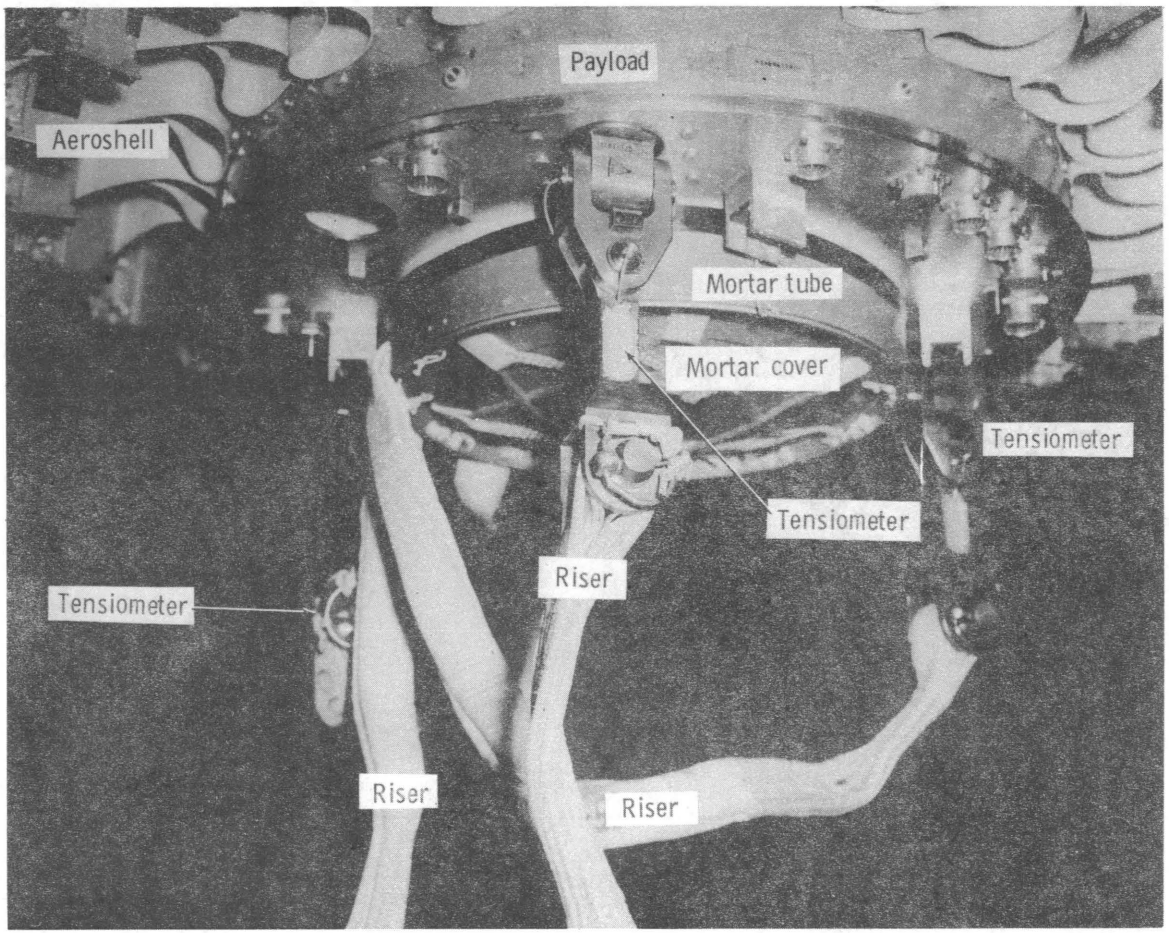

L-70-24.1

Figure 19.- Photograph of aft end of payload showing tensiometers, risers, end of mortar tube, and mortar cover.

of a universal joint arrangement which allowed them to assume alignment with the parachute attachment riser during the parachute test period.

Payload accelerations were measured by servo-type accelerometers. Two accelerometers were aligned with the longitudinal axis of the payload. The first, referred to as the high-range longitudinal accelerometer was calibrated for ± 30 g units. The other longitudinal accelerometer referred to as the low-range unit, was calibrated for ± 5 g units. This lower-range longitudinal accelerometer was included to provide more accurate data during portions of the test when accelerations were low. Two other accelerometers were mounted normal to the payload longitudinal axis and normal to each other. These units, referred to herein as the transverse accelerometers, were also calibrated for ± 5 g units.

The attitude reference system, referred to herein as the gyro platform, consisted of two two-degree-of-freedom gyros mounted on a common gimbal. During flight the gyro platform was used to measure the attitude of the payload relative to an inertial reference.

Two cameras were used to record the parachute deployment process, the canopy inflation, and the subsequent parachute performance. Both of these aft-looking cameras were started at the same time (1 second prior to mortar firing) although one camera operated at 64 pictures per second and the other at 16 pictures per second. The faster frame rate camera was used primarily to acquire details of the high frequency motion of the parachute during deployment and operation at supersonic velocities whereas the slower frame rate camera (having the same length of film) was able to record events for a much longer period of time

(100 seconds versus 25 seconds).

Coded timing marks appeared on all the payload camera films and on the telemetry records recorded at the ground stations to allow correlation of events recorded on film with actual flight test times.

VIII. RESULTS AND DISCUSSION

The data obtained during the flight test included radar tracking, loadings associated with parachute opening and descent through the Earth's atmosphere, meteorological data, and on-board payload camera coverage of the parachute during opening and descent through the Earth's atmosphere. The radar and meteorological data were used for assessing the operating environment and performance of the parachute including the Mach number, density, payload true air speed, dynamic pressure. Tensiometer and camera film data were used to relate parachute loads to the significant events associated with parachute opening including line stretch, snatch force, and fully opened shock load. The camera film data were also used to analyze the causes of the damage sustained by the parachute during the flight test.

A. Flight Test Data

Histories of payload altitude and relative velocity for the first 400 seconds of the flight as measured by the Wallops radar are shown in figures 20 and 21. Figure 18 presented the flight sequence and the recorded times for the significant flight events.

Meteorological data used in the analysis of the parachute performance were attained by means of an Arcasonde sounding rocket payload launched at 2 hours and 55 minutes after the parachute flight test launch time. These data were supplemented by data from a radiosonde which was released

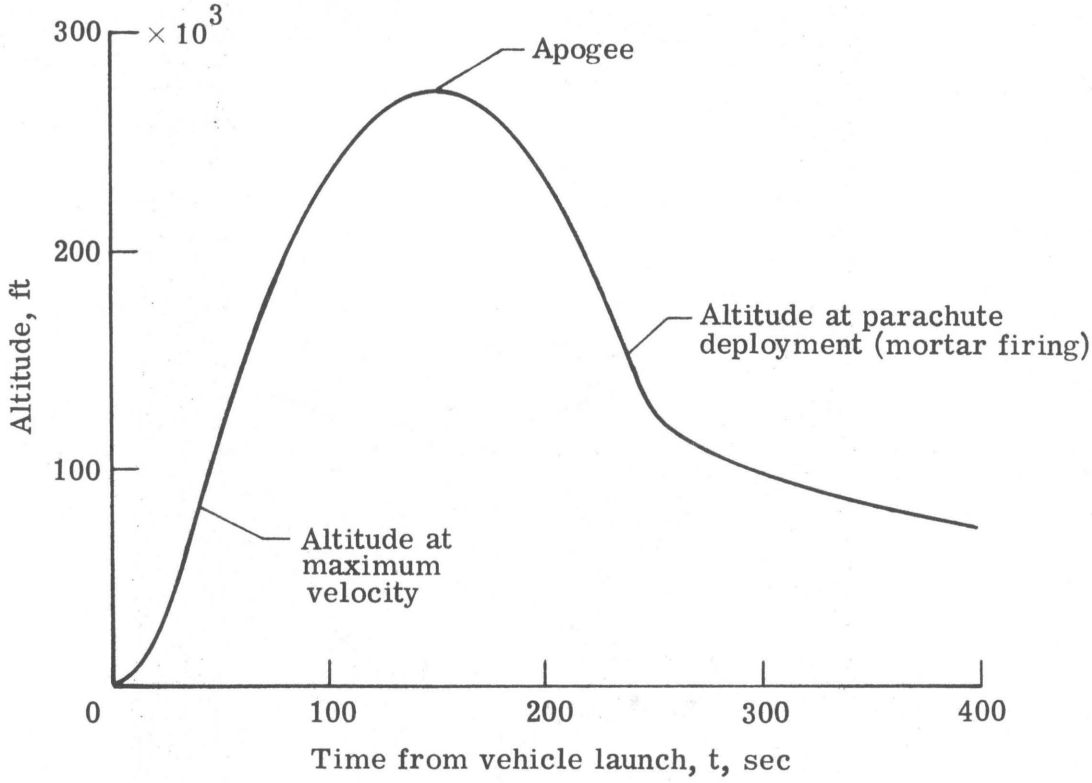

Figure 20.- Flight history of altitude.

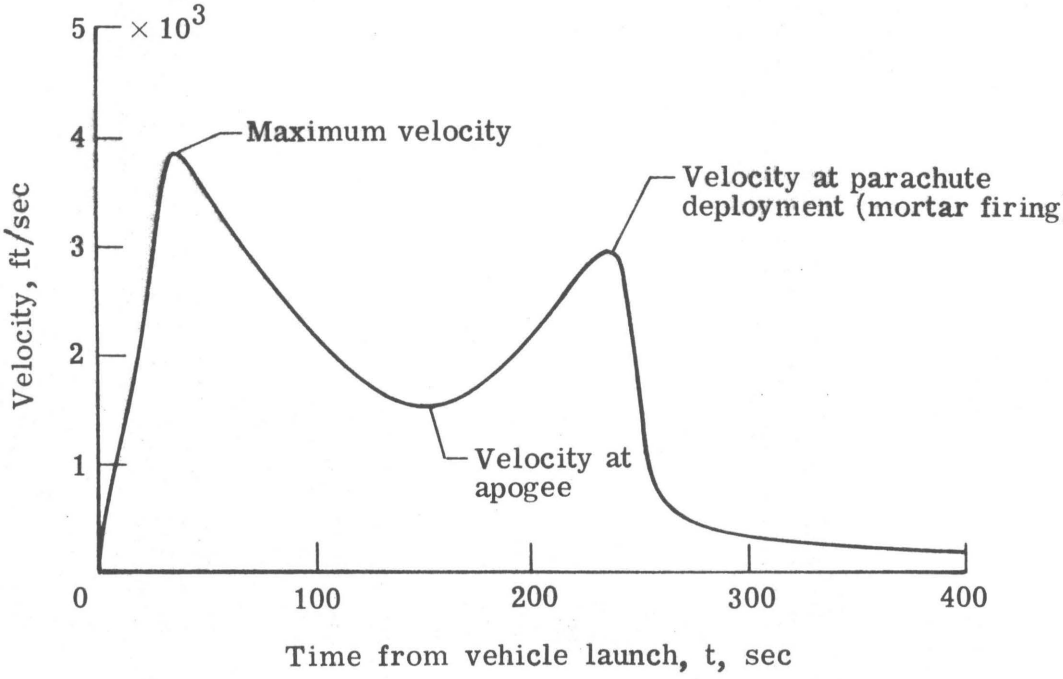

Figure 21.- Flight history of relative velocity.

3 hours and 34 minutes before the flight test vehicle was launched. The Earth's atmospheric density as derived from the measured temperature profiles is shown in figure 22 as a ratio to the 1962 U.S. Standard Atmosphere values found in reference 11. The estimated uncertainty of the derived density ranges from ±3 percent at ground level to about ±6 percent at 54 km.

The measured atmospheric data were used with the radar track data to determine histories of payload true air speed (figure 23), Mach number (figure 24), and dynamic pressure (figure 25) during the 20-second period immediately after initiation of parachute deployment. By definition, the initiation of parachute deployment corresponds to mortar firing (t' = 0). Parachute deployment was initiated at a true air speed of 2900 ft/sec, a Mach number of 2.69, a dynamic pressure of 18.3 psf, and an altitude of 145,300 feet above mean sea level. The first peak load associated with full opening of the parachute canopy came at t' = 1.22 seconds at which time the test conditions were a true airspeed of 2805 ft/sec, a Mach number of 2.62, a dynamic pressure of 19.4 psf, and an altitude of 142,235 feet above mean sea level. The estimated uncertainty of these test conditions is about ±1 percent for the Mach number and ±5 percent for the dynamic pressure based on a ±1 percent velocity error, a ±2 percent temperature error, and a ±4 percent density error and by using a first-order error analysis.

The history of forces transmitted to each of the three riser line tensiometers and the direct summation of these forces for the first 20

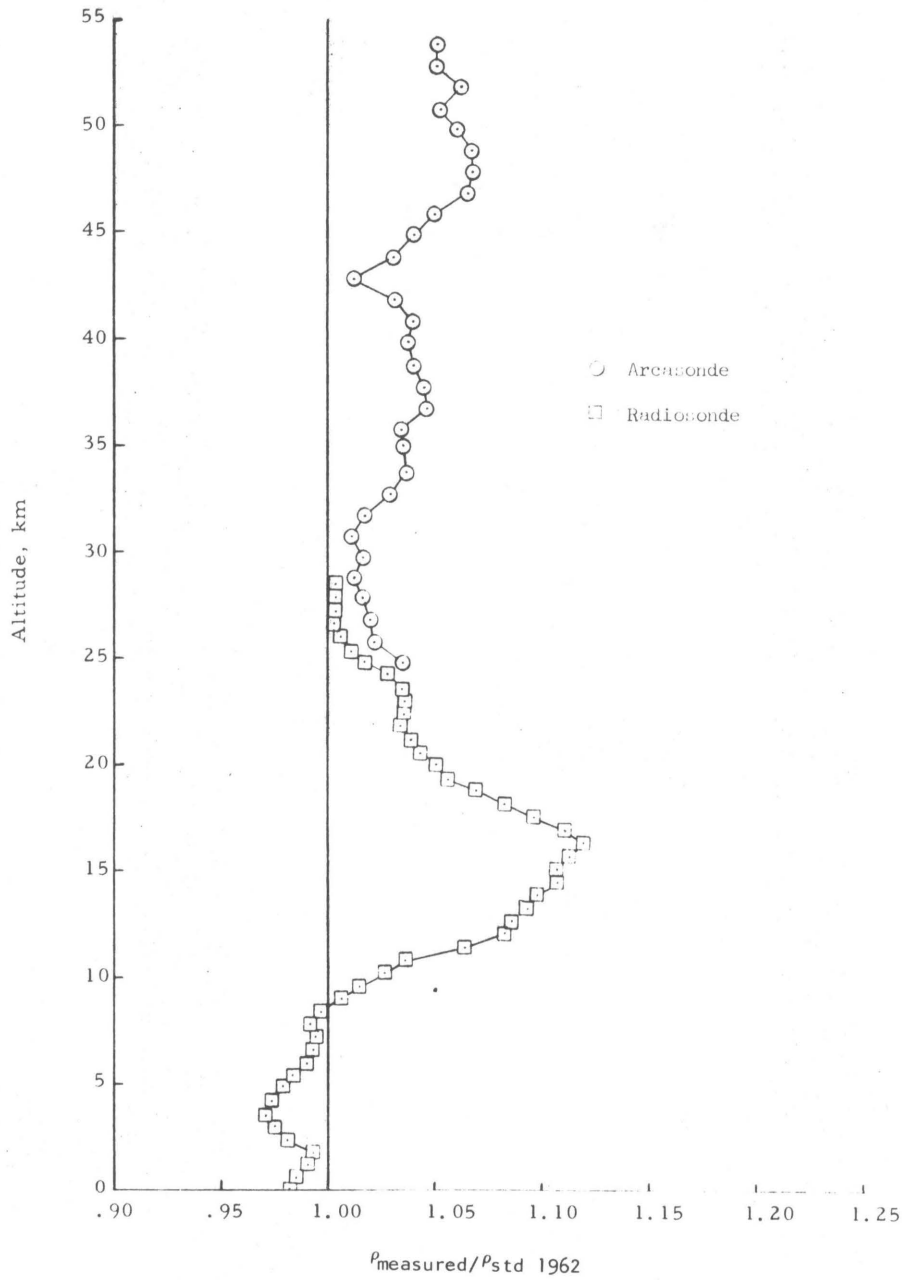

Figure 22.- Atmospheric-density profile.

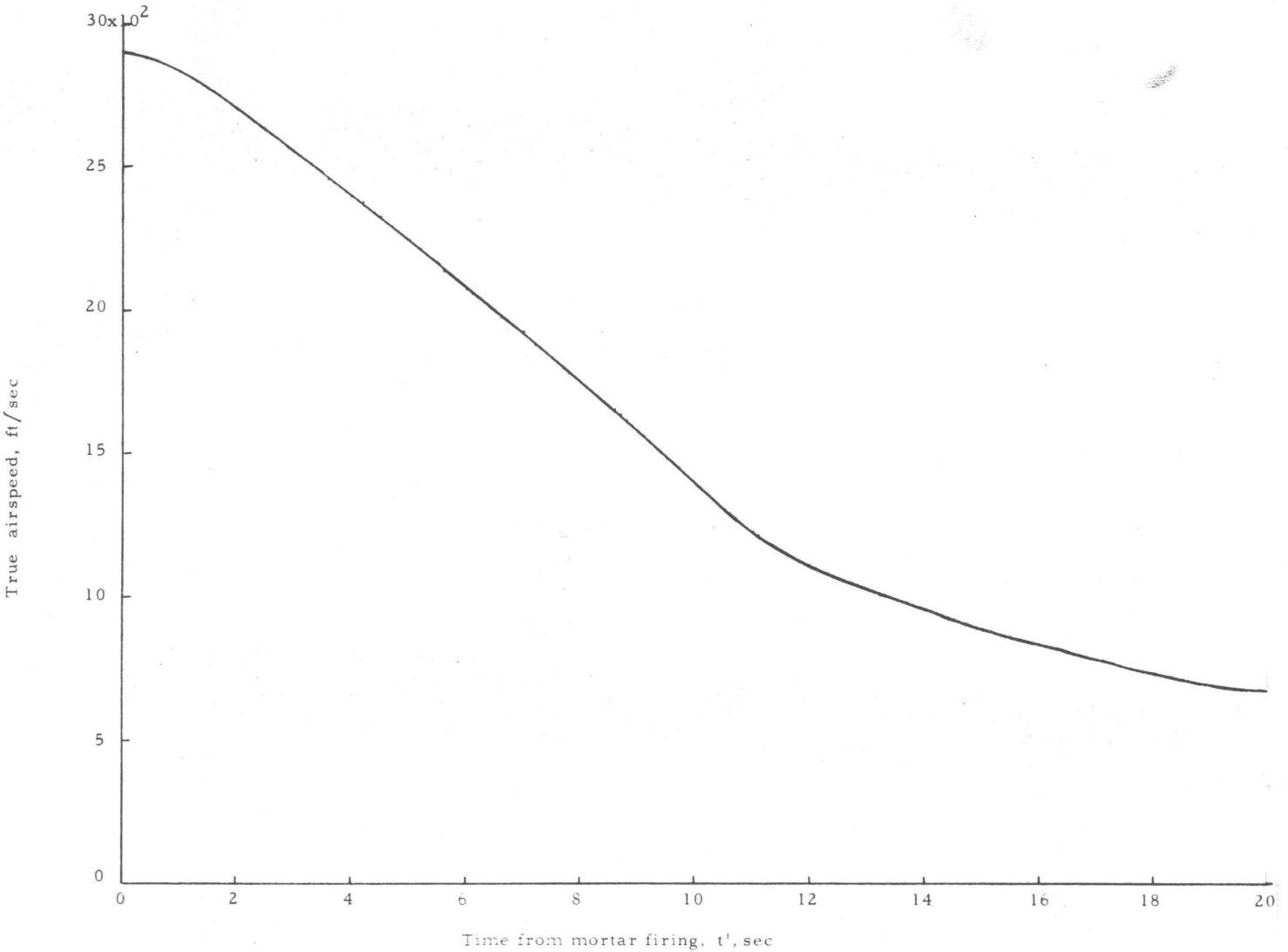

Figure 23.- True-airspeed history after mortar firing.

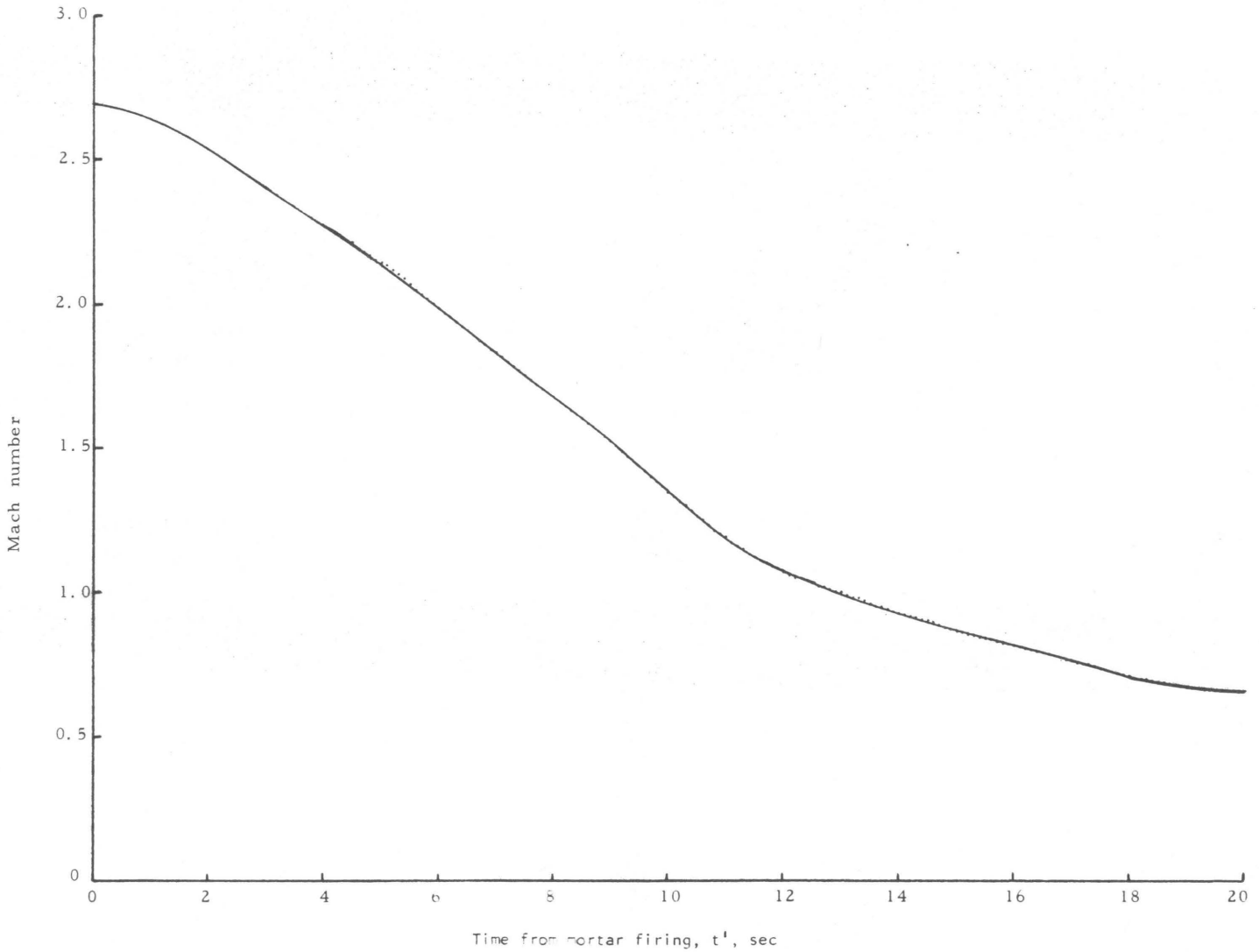

Figure 24.- Mach number history after mortar firing.

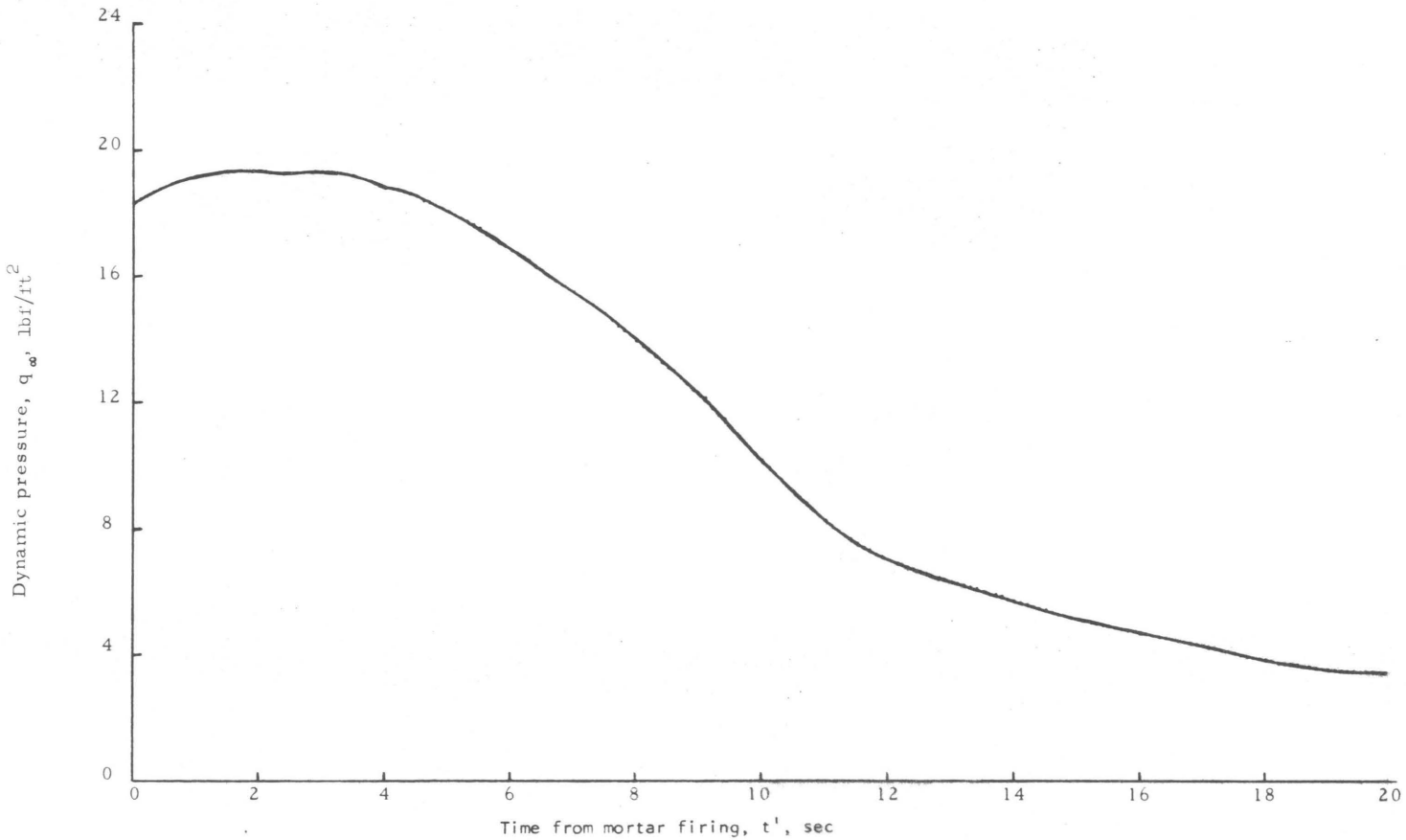

Figure 25.- Dynamic pressure history after mortar firing.

seconds after initiation of parachute deployment are presented in figure 26. The first small peak deployment load at t' = 0.12 seconds is believed to be associated with the full length deployment of the risers and tensiometers from their storage location on the aft deck of the payload. The second small peak deployment load (snatch force) of 2040 pounds at t' = 0.51 seconds is associated with full length deployment of the suspension lines (line stretch) and the beginning of canopy deployment. The loads associated with the parachute opening process begin at about t' = 0.86 seconds with the first peak opening load of 21,500 pounds occuring at t' = 1.22 seconds. This first peak load is associated with the first opening of the parachute canopy. Three more peak loads were encountered immediately thereafter. These loads (figure 26) were associated with the varying parachute frontal area, the continued increase in free stream dynamic pressure, and the elasticity of the system (particularly the parachute suspension lines). The last of these first four peak loads associated with the opening process was the largest loading encountered. This largest peak load was 23,330 pounds at t' = 1.42 seconds. Thereafter, the riser loads were of less magnitude, partially because the damage sustained by the parachute resulted in reduced frontal area, and later because of the reduced free stream dynamic pressure.

The histories of accelerations recorded by the accelerometers in the payload are presented in figure 27. The magnitudes of the accelerations shown are due in part to the deceleration forces imparted by the parachute to the aeroshell-payload and partly from the rapidly changing

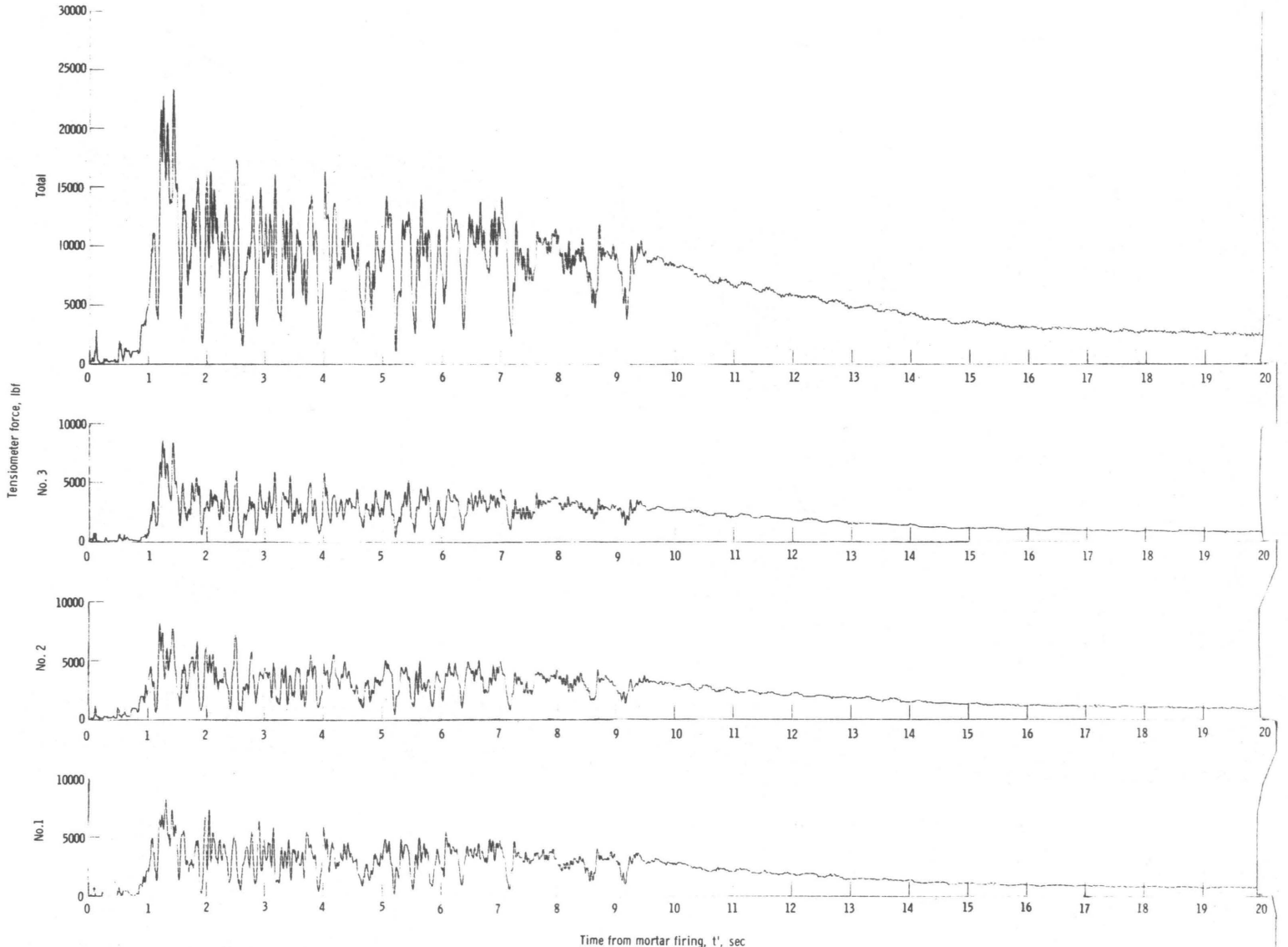

Figure 26.- Histories of measured tensiometer forces.

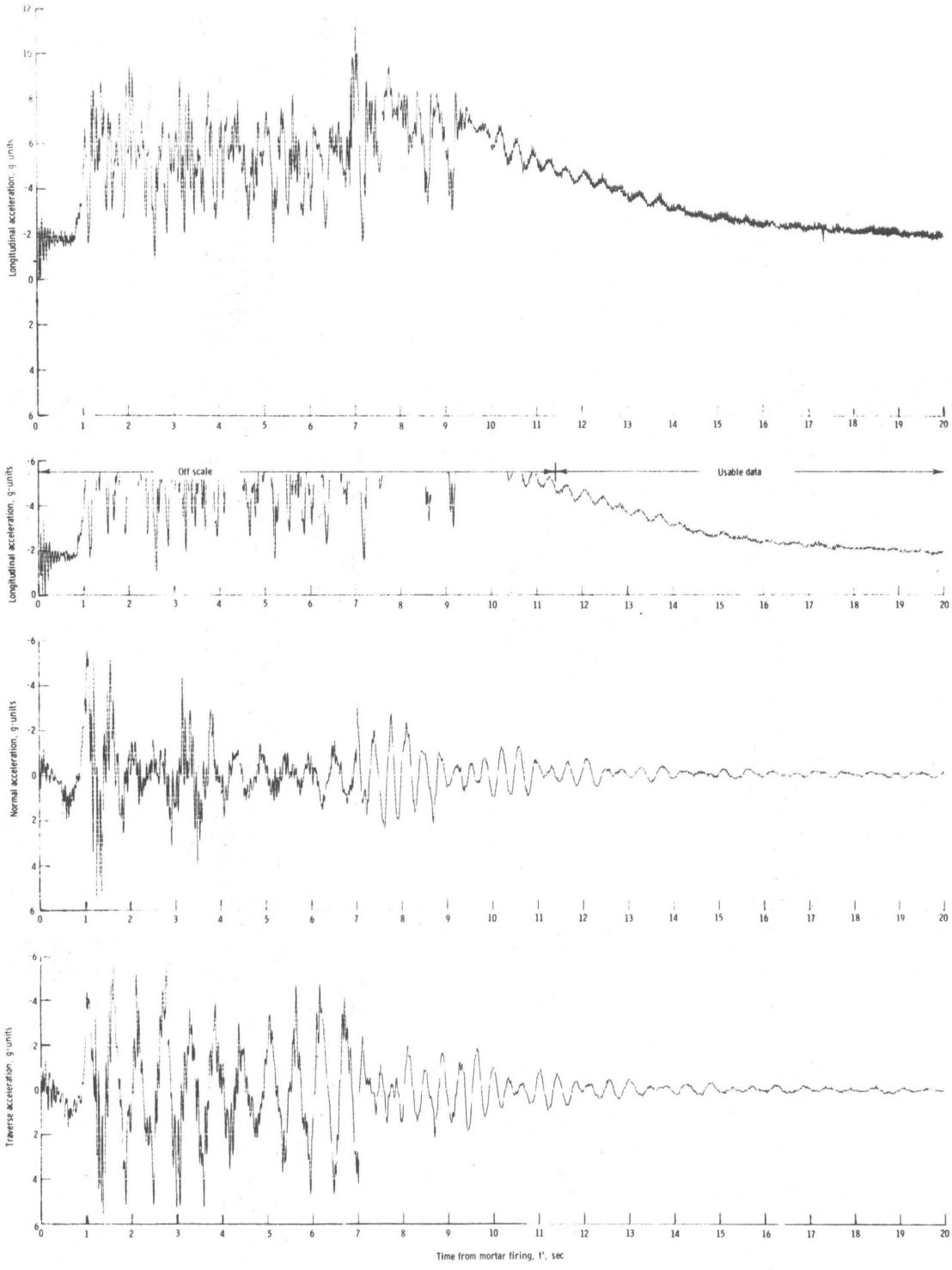

Figure 27.- Acceleration time histories.

aeroshell-payload angular position. The large peak in longitudinal deceleration at t' = 6.91 seconds is associated with the release of the payload from the aeroshell, which resulted in a 44-percent reduction in system weight from 2631 pounds to 1472 pounds.

The payload angular positions with respect to the flight path were determined by the procedure given in reference 8 and are presented in figure 28.

B. Analysis of Parachute Performance

The disk-gap-band parachute was flight tested behind the bluff body aeroshell and attached payload for a period of seven seconds after which the bluff body aeroshell was released. During the flight test the parachute was damaged at the outer disk edge and in the band area. About one-half of the gores were damaged at the disk edge area and all of the gores in the band area were damaged. Some damage occurred during the first opening of the parachute but most of the damage occurred in a progressive manner in a short interval of time immediately after the first opening. Most of the damaged areas of the parachute could be identified on the aft camera film by the end of the first four seconds of the flight test. An analysis of the various aspects of the parachute performance are presented in this section and an analysis of the parachute damage in the following section.

Parachute deployment.- Based on a total suspension line plus attachment system length of 64.6 feet (see figure 14) and a measured time to line stretch of 0.51 seconds, the average deployment velocity from mortar firing to line stretch was 126 ft/sec. The resulting snatch

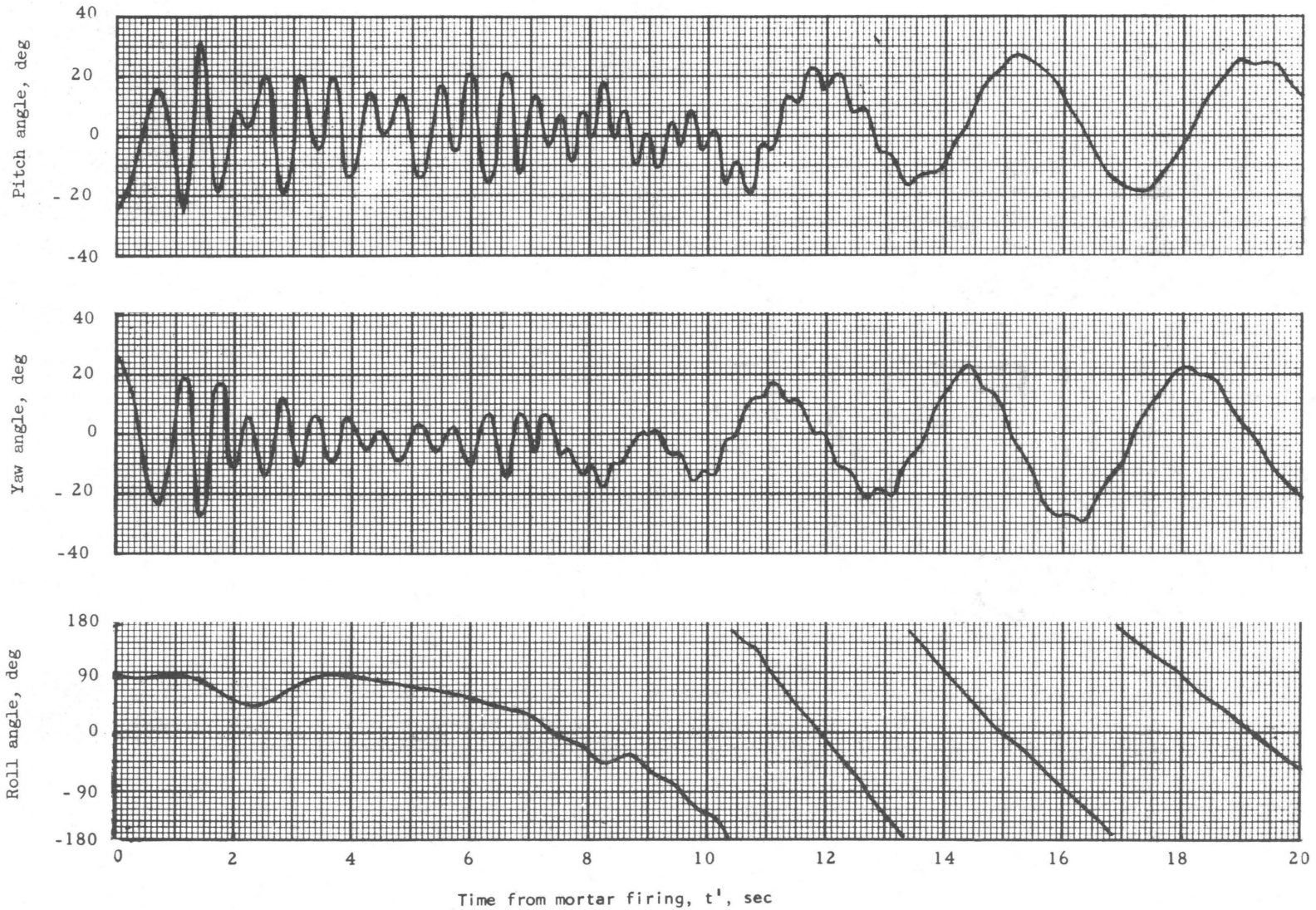

Figure 28.- Payload pitch, yaw, and roll angles with respect to vehicle flight path.

force from the tensiometer force history was 2040 pounds.

Parachute inflation.- Selected frames from the aft camera film showing the initial stages of parachute deployment, inflation, shape distortions, and damage propagation sequences are presented in figure 29.

The parachute projected area ratio history as determined from the aft camera film is presented in detail in figure 30 for the inflation sequence and for a short interval thereafter. A more general presentation of the parachute projected area ratio history for the total 20 seconds after mortar firing is presented in figure 31. The solid lines between data points on figures 30 and 31 represent intervals where the parachute canopy was in the camera field of view from frame to frame. The blank spaces between data points represent intervals where the parachute canopy is partially or totally out of view of the payload aft-viewing camera. A dashed line was used in the interval of the initial parachute opening from t' = 0.95 to 1.19 seconds during which the parachute is not in the field of view of the payload camera to indicate that the projected area ratio curve probably continues to grow smoothly. This is believed to be so even though the tensiometer forces have a peak at 1.09 seconds, a minimum at 1.17 seconds and the first large peak at 1.22 seconds. Similar variations in transmitted parachute loads occurred during the parachute opening process of the flight tests of references 9, 10, and 11 even though the parachute projected area ratio growth continued smoothly during this interval. The variations in tensiometer forces during this interval are due primarily to the elasticity

Frame 6, t' = 0.096 sec

Frame 7, t' = 0.111 sec

Frame 8, t' = 0.127 sec

Frame 9, t' = 0.143 sec

L-72-6590

Figure 29.- Onboard camera photographs.

Frame 10, t' = 0.159 sec

Frame 11, t' = 0.175 sec

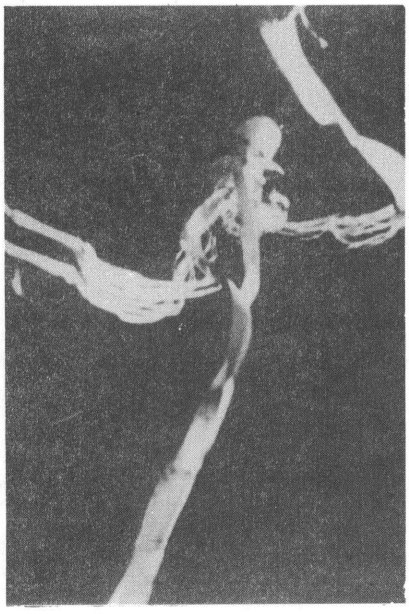

Frame 12, t' = 0.191 sec

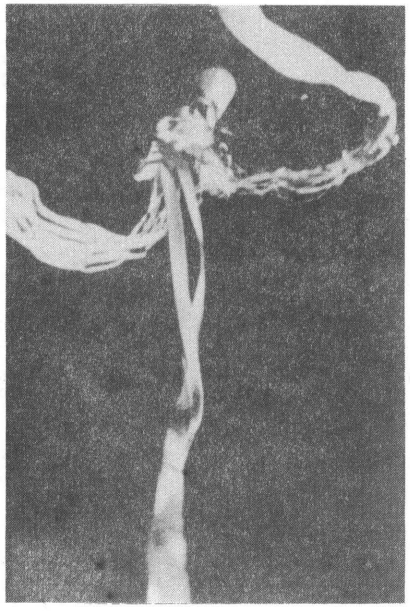

Frame 13, t' = 0.207 sec

L-72-6591

Figure 29.- Continued.

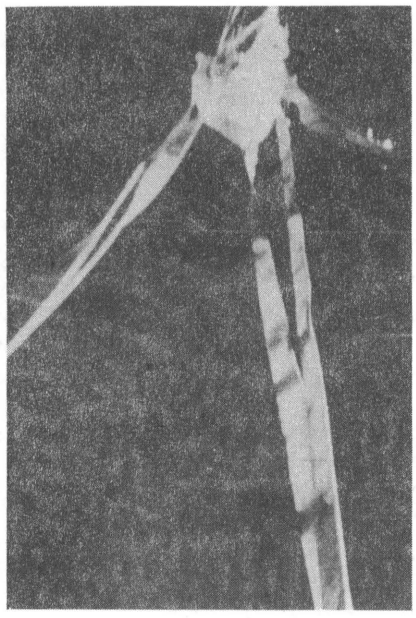

Frame 52, t' = 0.828 sec

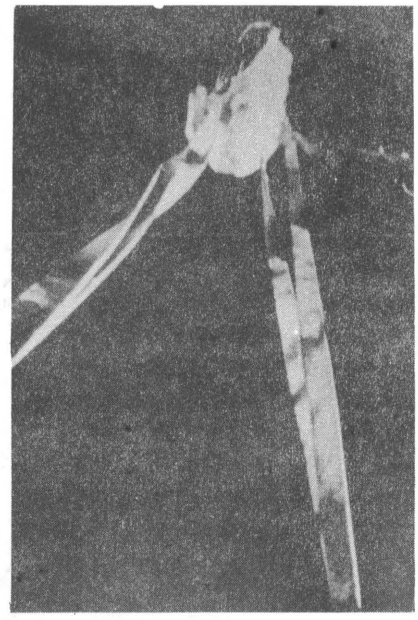

Frame 53, t' = 0.844 sec

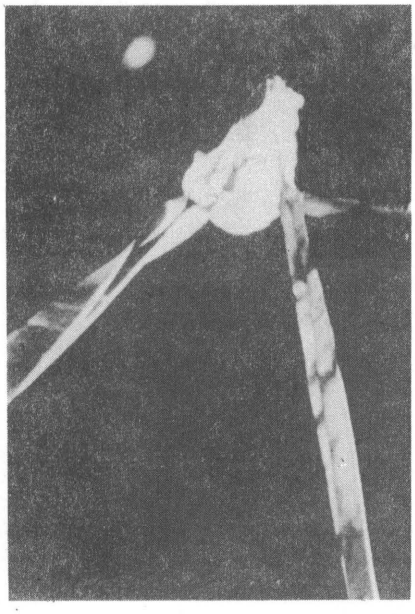

Frame 54, t' = 0.860 sec

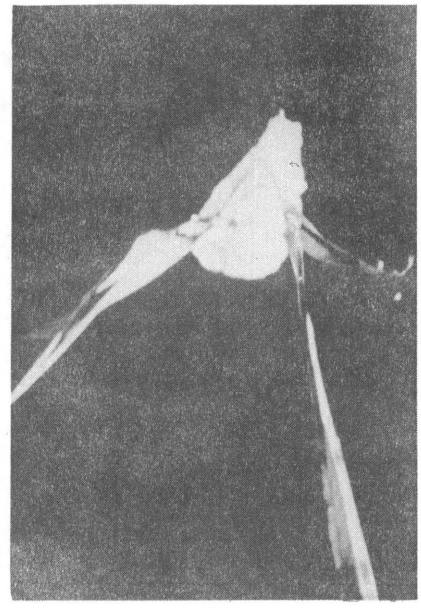

Frame 55, t' = 0.876 sec

L-72-6592

Figure 29.- Continued.

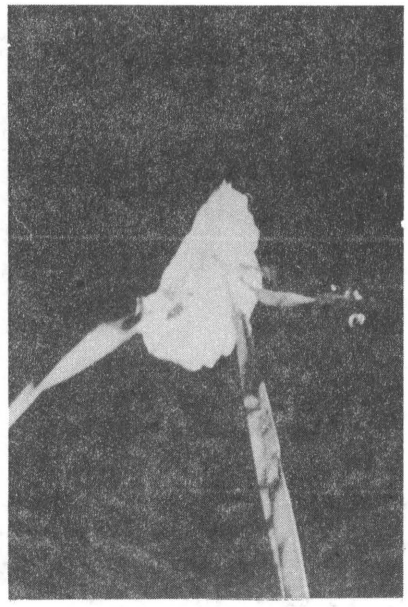

Frame 56, t' = 0.892 sec

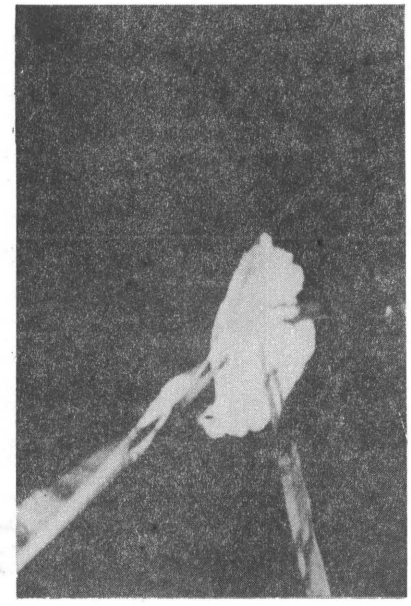

Frame 57, t' = 0.908 sec

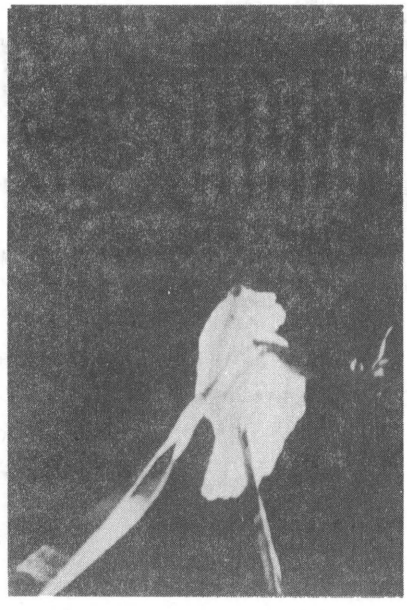

Frame 58, t' = 0.924 sec

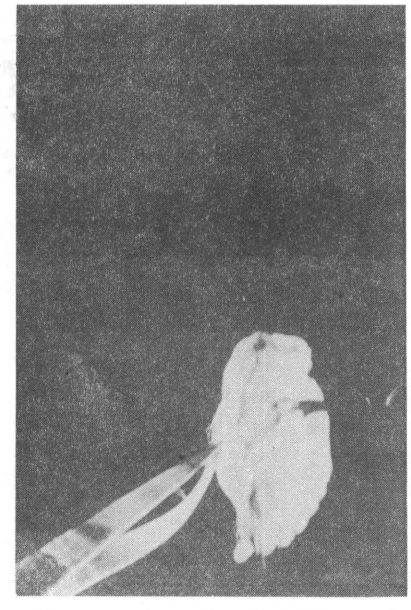

Frame 59, t' = 0.939 sec

L-72-6593

Figure 29.- Continued.

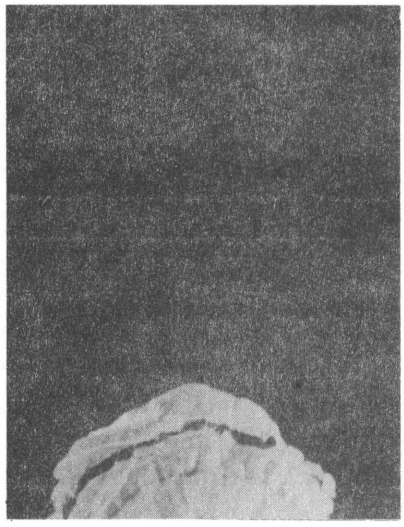

Frame 71, t' = 1.131 sec

Frame 72, t' = 1.146 sec

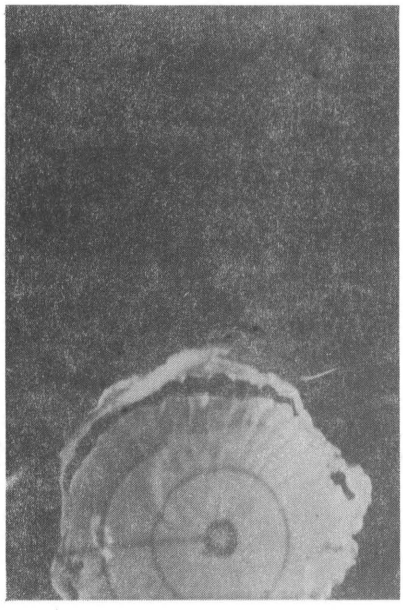

Frame 73, t' = 1.162 sec

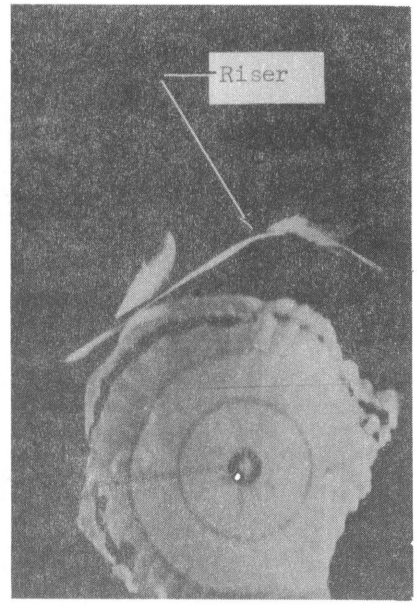

Frame 74, t' = 1.178 sec

L-72-6594

Figure 29.- Continued.

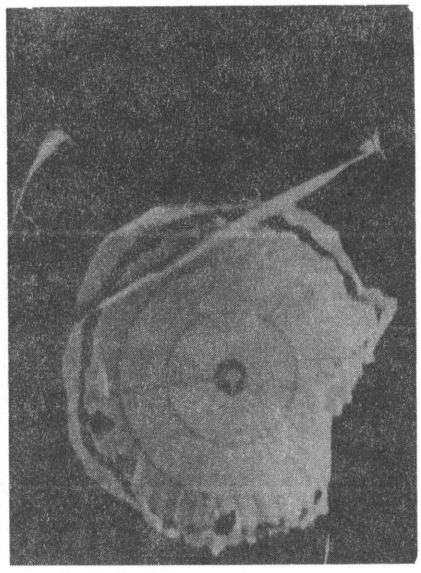

Frame 75, $t' = 1.194$ sec

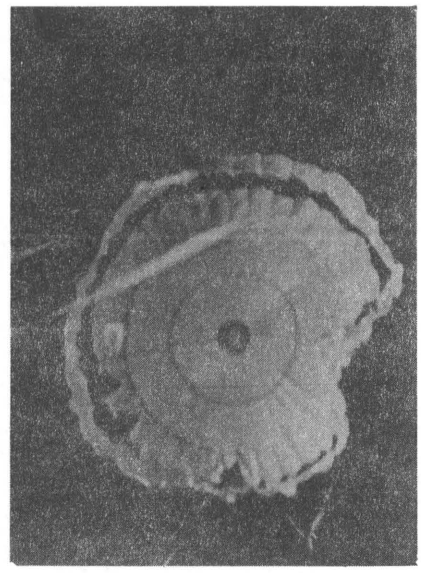

Frame 76, $t' = 1.210$ sec
(maximum frontal area)

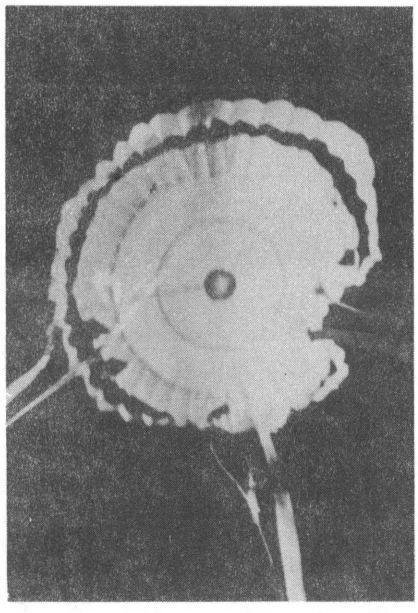

Frame 77, $t' = 1.226$ sec

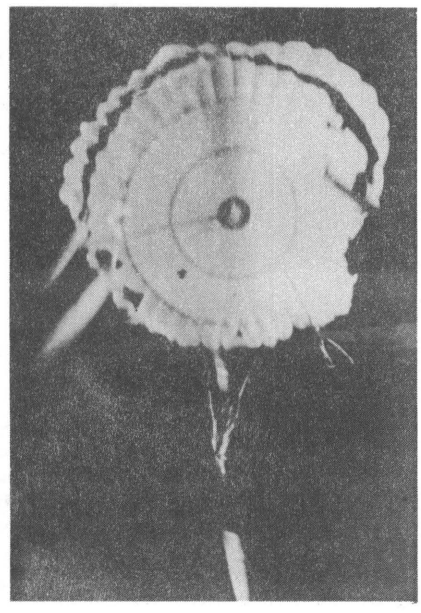

Frame 78, $t' = 1.242$ sec

L-72-6595

Figure 29.- Continued.

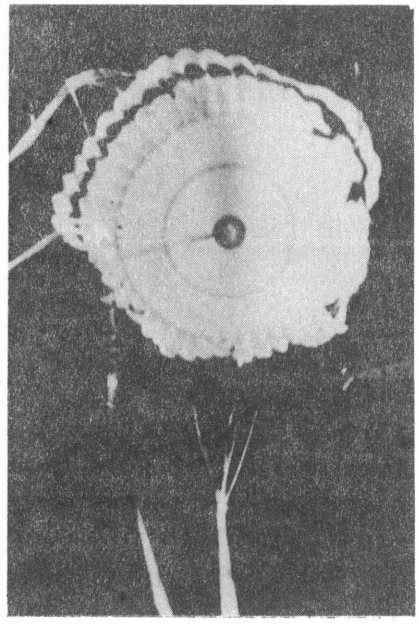

Frame 79, t' = 1.258 sec

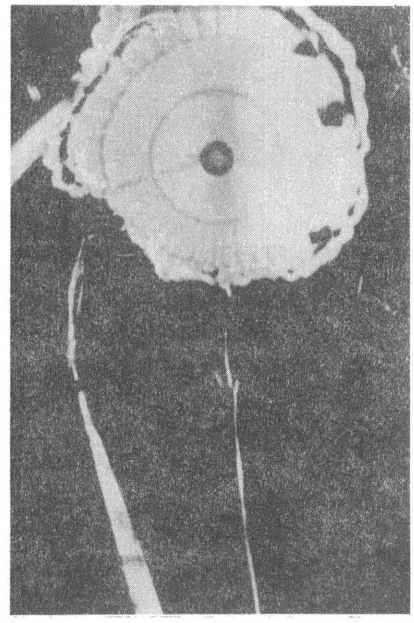

Frame 80, t' = 1.274 sec

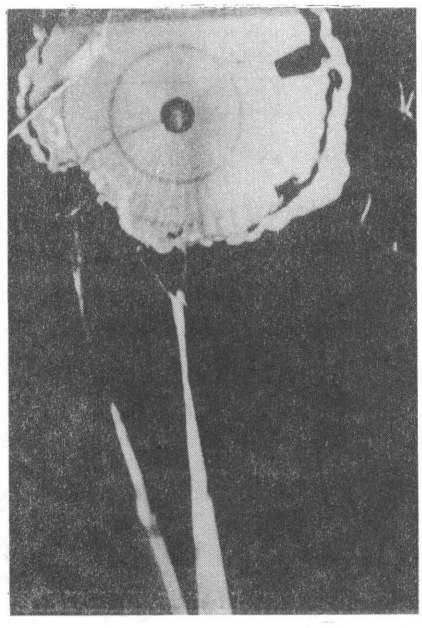

Frame 81, t' = 1.290 sec

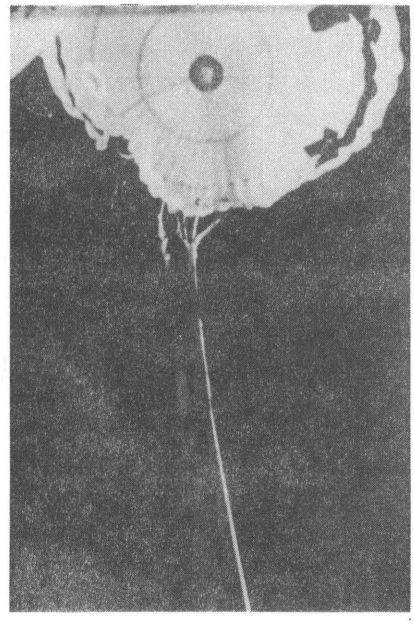

Frame 82, t' = 1.306 sec

L-72-6596

Figure 29.- Continued.

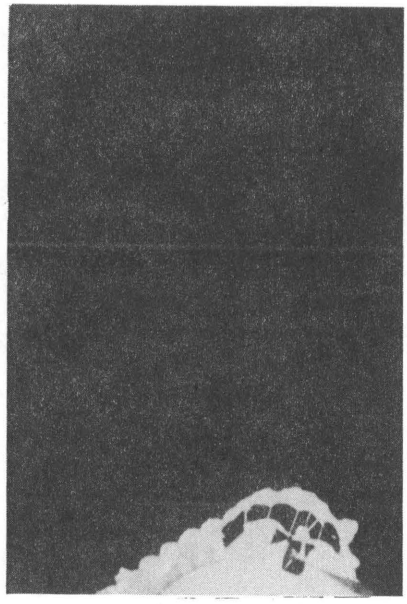

Frame 98, t' = 1.561 sec

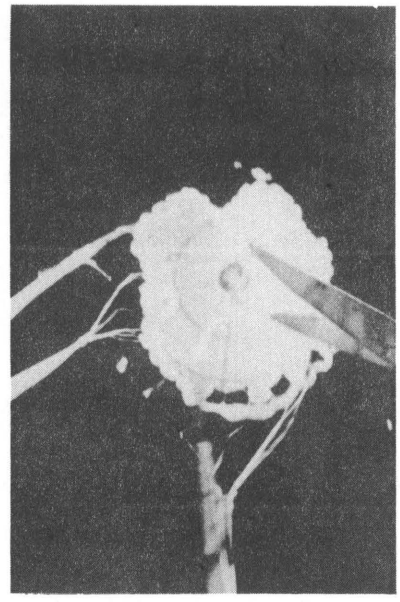

Frame 110, t' = 1.752 sec

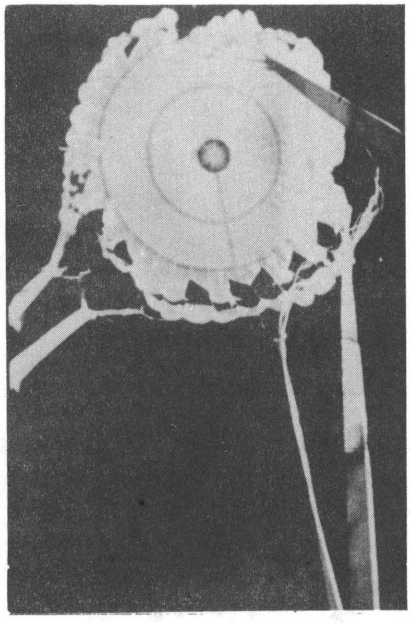

Frame 115, t' = 1.831 sec

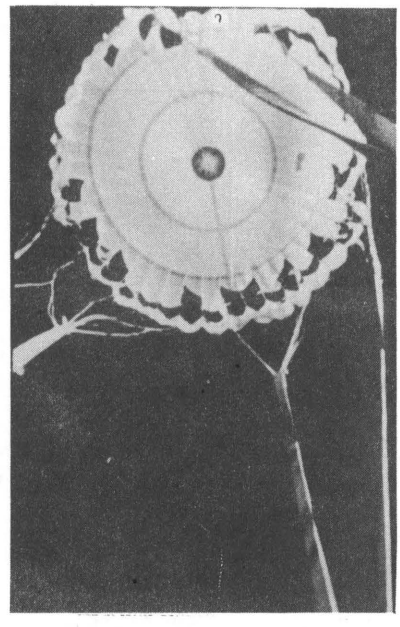

Frame 116, t' = 1.847 sec

L-72-6597

Figure 29.- Continued.

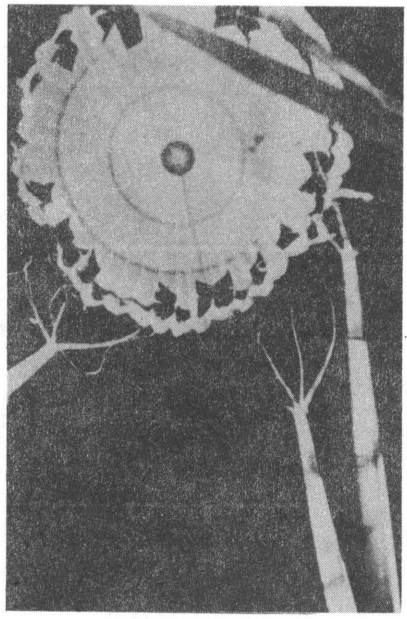

Frame 117, t' = 1.863 sec

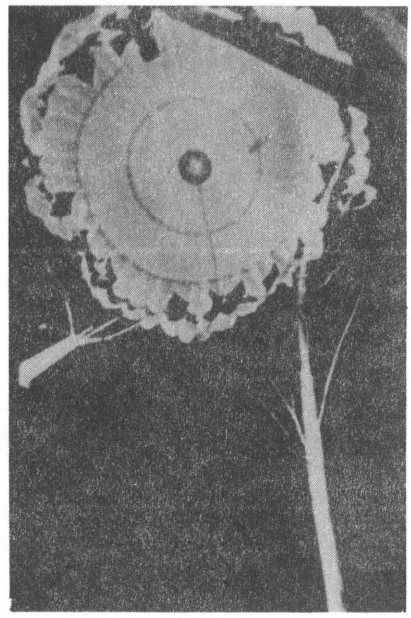

Frame 118, t' = 1.879 sec

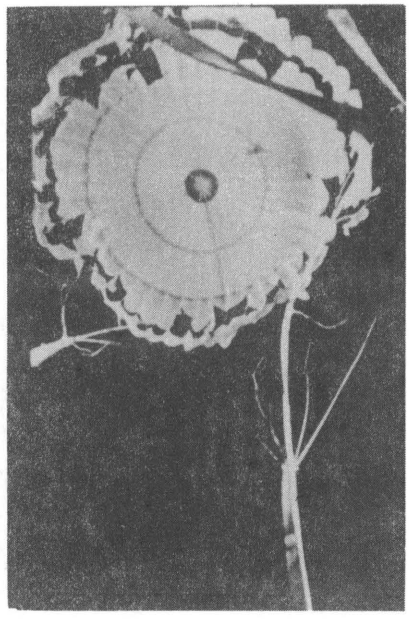

Frame 119, t' = 1.894 sec

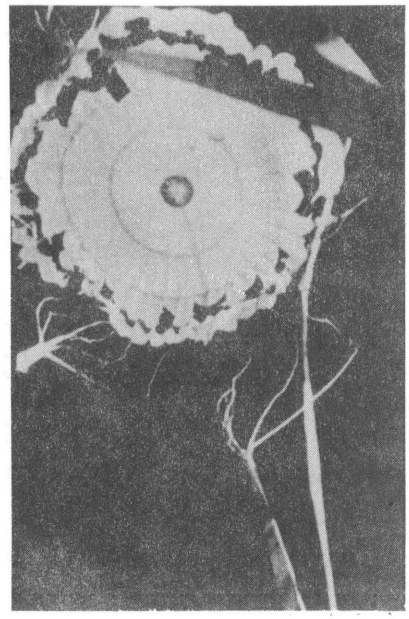

Frame 120, t' = 1.911 sec

L-72-6598

Figure 29.- Continued.

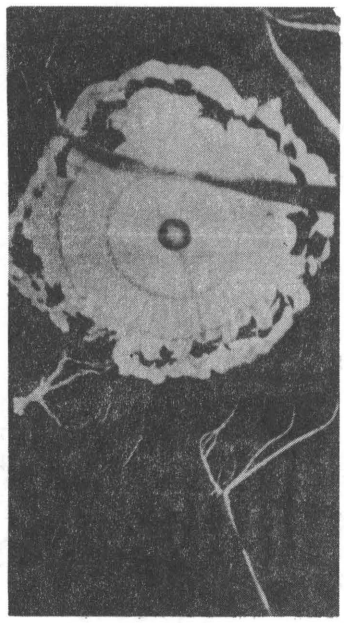

Frame 121, t' = 1.927 sec

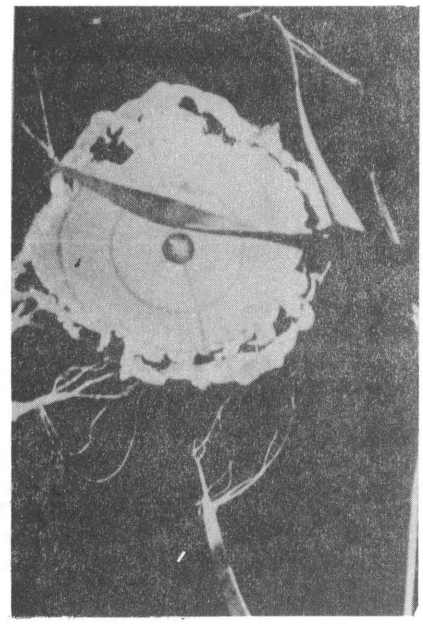

Frame 122, t' = 1.943 sec

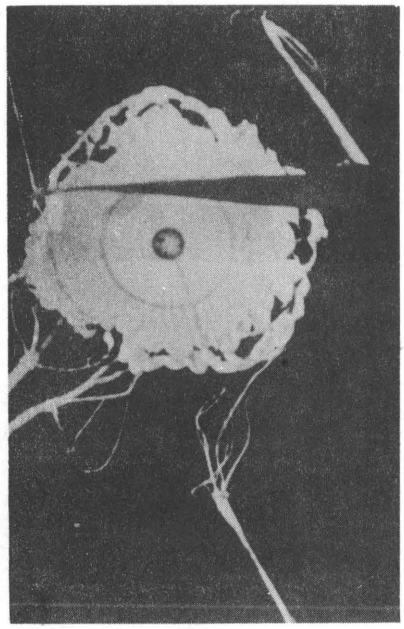

Frame 123, t' = 1.959 sec

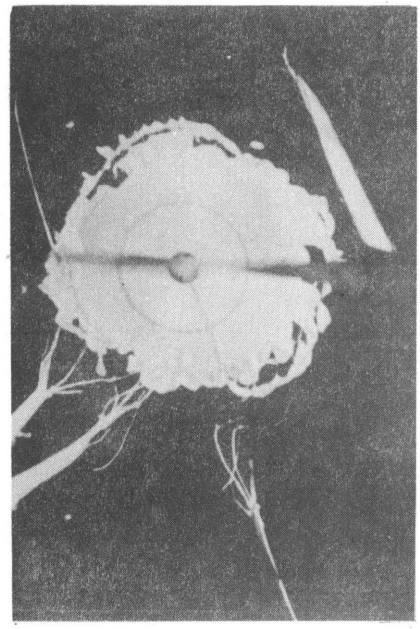

Frame 124, t' = 1.975 sec

L-72-6599

Figure 29.- Continued.

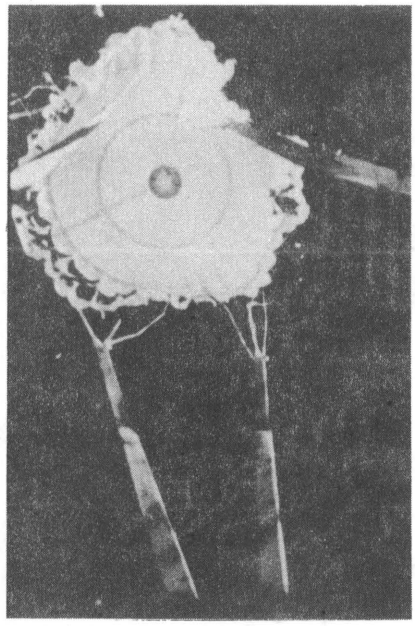

Frame 192, t' = 3.057 sec

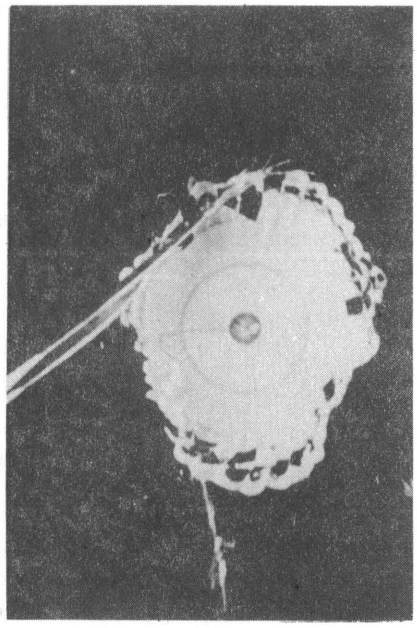

Frame 218, t' = 3.471 sec

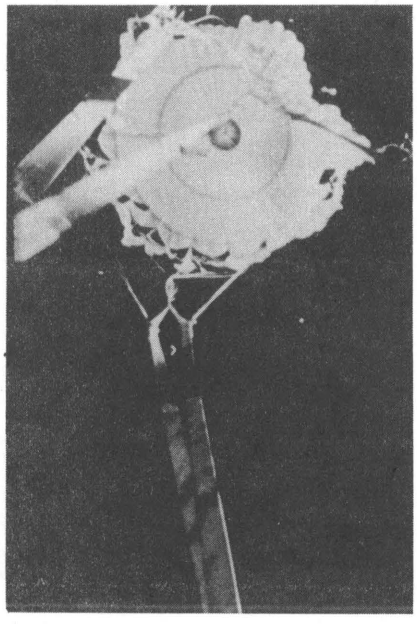

Frame 224, t' = 3.567 sec

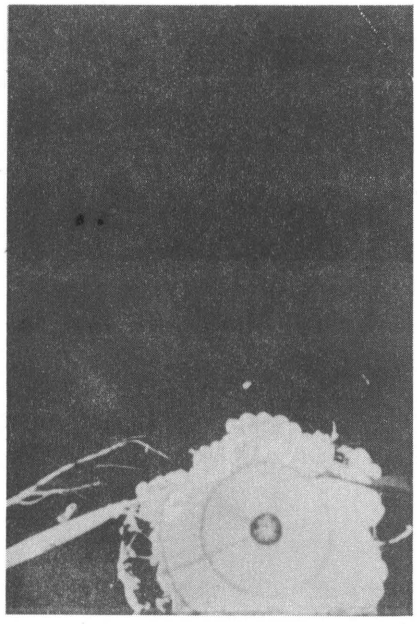

Frame 241, t' = 3.838 sec

L-72-6600

Figure 29.- Concluded.

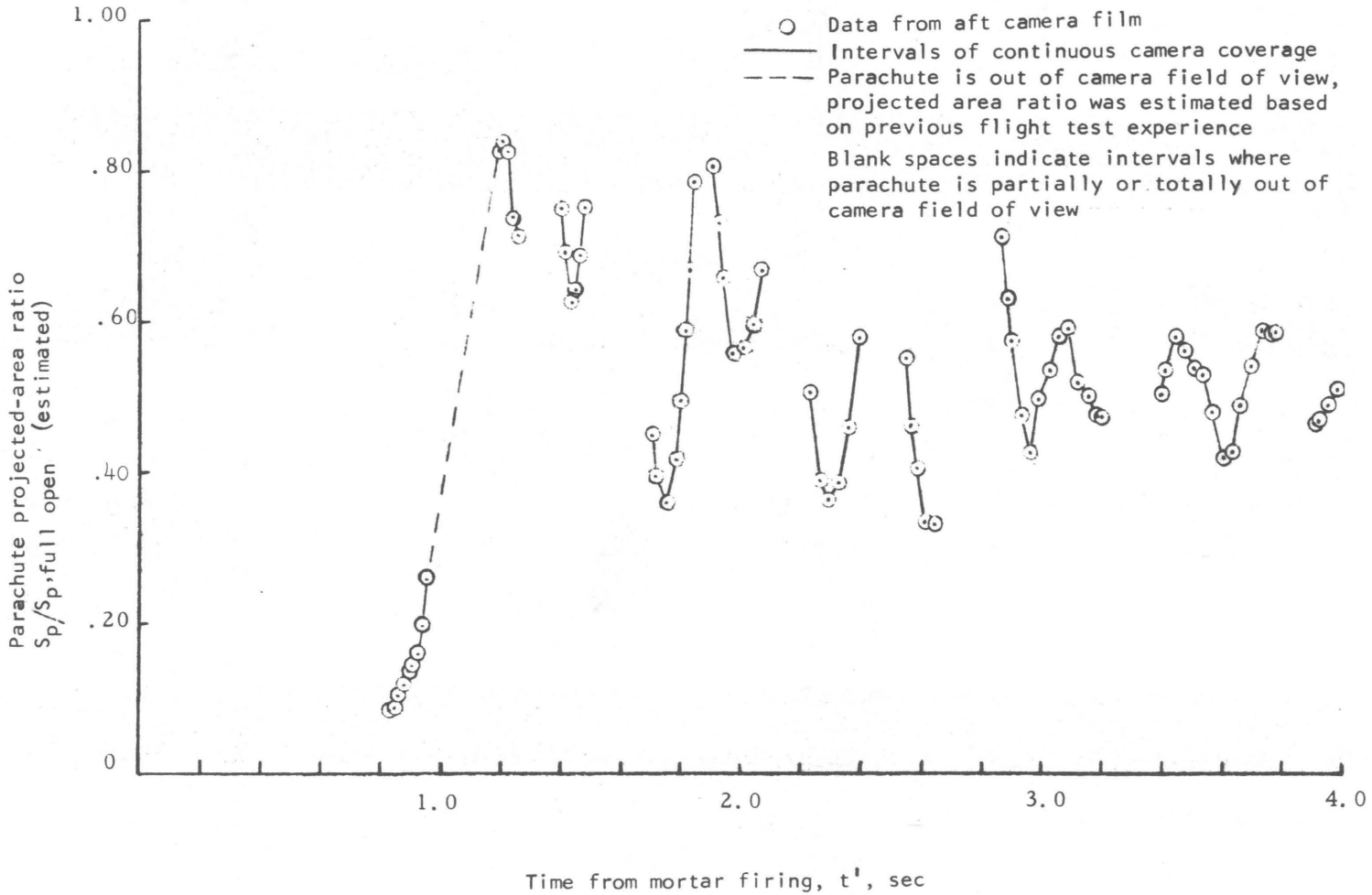

Figure 30.- Parachute projected-area ratio during deployment and initial test period.

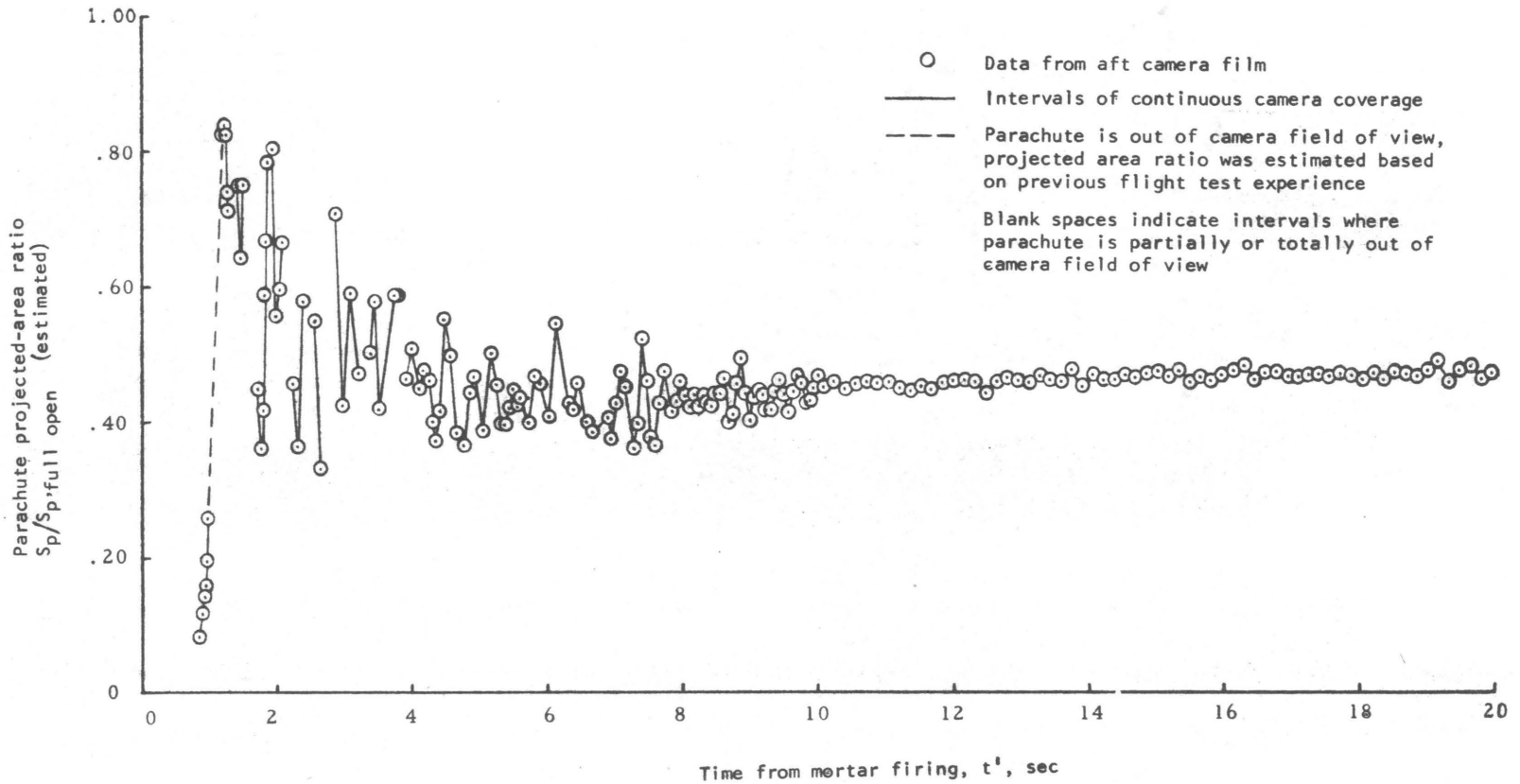

Figure 31.- Parachute projected-area ratio for first 20 seconds of operation.

of the parachute suspension lines.

As can be seen from figure 29c at t' = 1.21 seconds the parachute did not reach a complete full inflation at all places around the outer edges of the canopy. Because of parachute damage that began at the first opening and progressed rapidly thereafter, the first opening was the maximum attained for the entire flight. Therefore, an estimate was made of what the final projected area should have been by circumscribing a circle around the nearly fully opened parachute canopy as shown in figure 29c at t' = 1.21 seconds. The values of frontal area ratio shown in figures 30 and 31 are based on the estimated full open parachute projected area.

Drag efficiency.- The axial-force coefficient $C_{A,o}$ of the parachute is presented in figure 32 for the first 20 seconds after mortar firing. The $C_{A,o}$ values were determined for a non-elastic two-body system using the following equation:

$$C_{A,o} = \frac{\Sigma F(m_t/m_{p\ell})}{q\,S_o} + \frac{[(m_t/m_{p\ell}) - 1]E_1}{q\,S_o} \qquad (53)$$

The second term of the right hand side of the equation was applicable only for the first seven seconds of the parachute flight test where the bluff aeroshell remained attached to the payload. After release of the aeroshell the drag of the slender body instrumented payload was neglected and only the first term of the right-hand-side of the equation was applicable. (Data on the performance of the erected aeroshell-payload combination prior to parachute deployment is presented in reference 7).

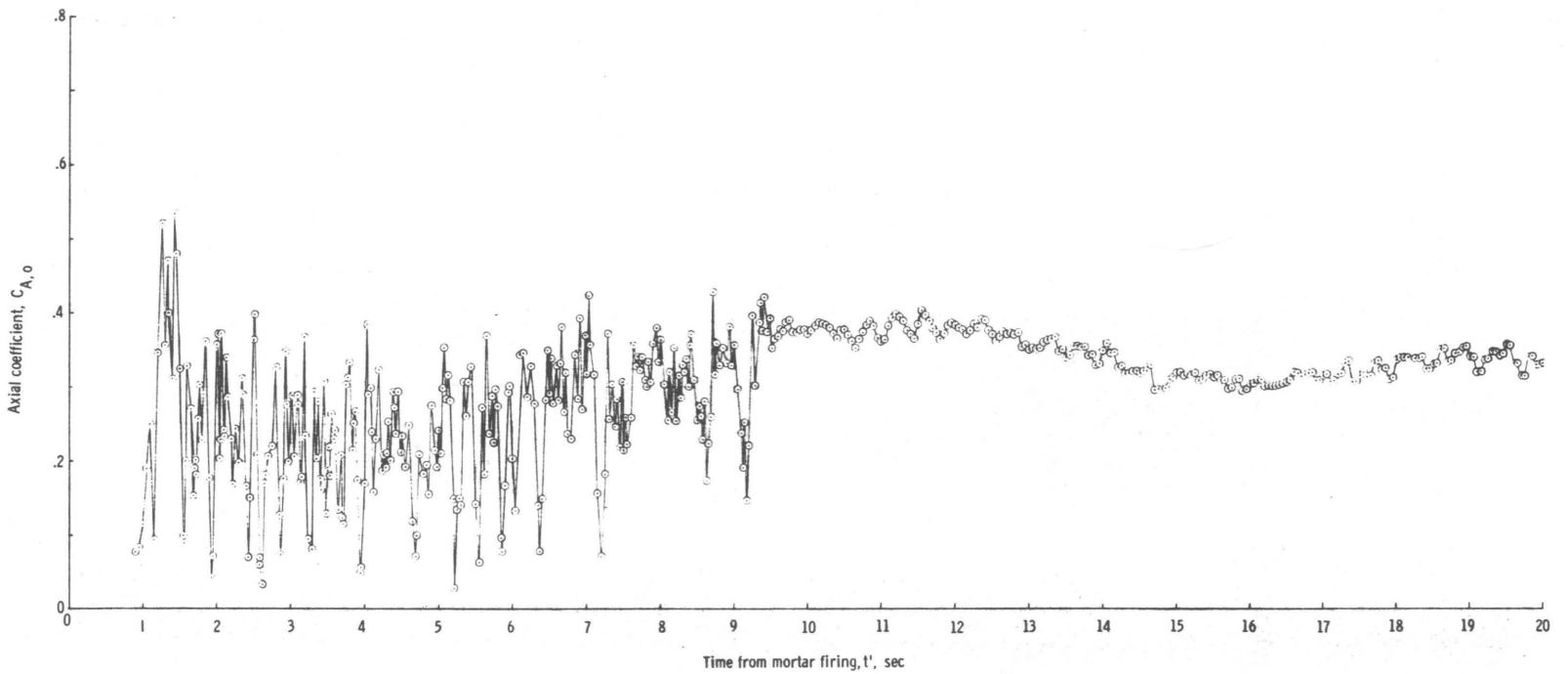

Figure 32.- Parachute axial-force coefficient as a function of time.

Average values of the parachute axial-force coefficient $C_{A,o}$ were determined at Mach number interval of 0.05 over the 20-second data period and these average values are presented in figure 33 as the drag coefficient $C_{D,o}$ as a function of Mach number.

The vertical descent velocity and the parachute effective drag coefficient $(C_{D,o})_{eff}$ during steady-state descent are presented in figure 34 for the altitude range from 100,000 to 20,000 feet. The values of effective drag coefficient were determined using the following equation:

$$(C_{D,o})_{eff} = \frac{2m_t}{\rho(\dot{z}_E)^2 S_o}(g - \ddot{z}_E) \qquad (54)$$

As shown in figure 33 the test parachute provided an average effective drag coefficient of 0.33 which represents about 60 percent of that expected for an undamaged disk-gap-band parachute (reference 10). The scatter in the $(C_{D,o})_{eff}$ data increased at the lower altitudes because small variations or errors in measured descent velocities result in large changes in the $(C_{D,o})_{eff}$ values as determined by the above equation.

Stability.- At the time of parachute deployment the aeroshell-payload combination was oscillating through an angle-of-attack range of ±40 degrees. The oscillatory motion of the aeroshell-payload continued after deployment of the test parachute with the parachute soon exhibiting somewhat similar motion. The angular motion of the deployed parachute was obtained by first using the payload aft camera film to determine the

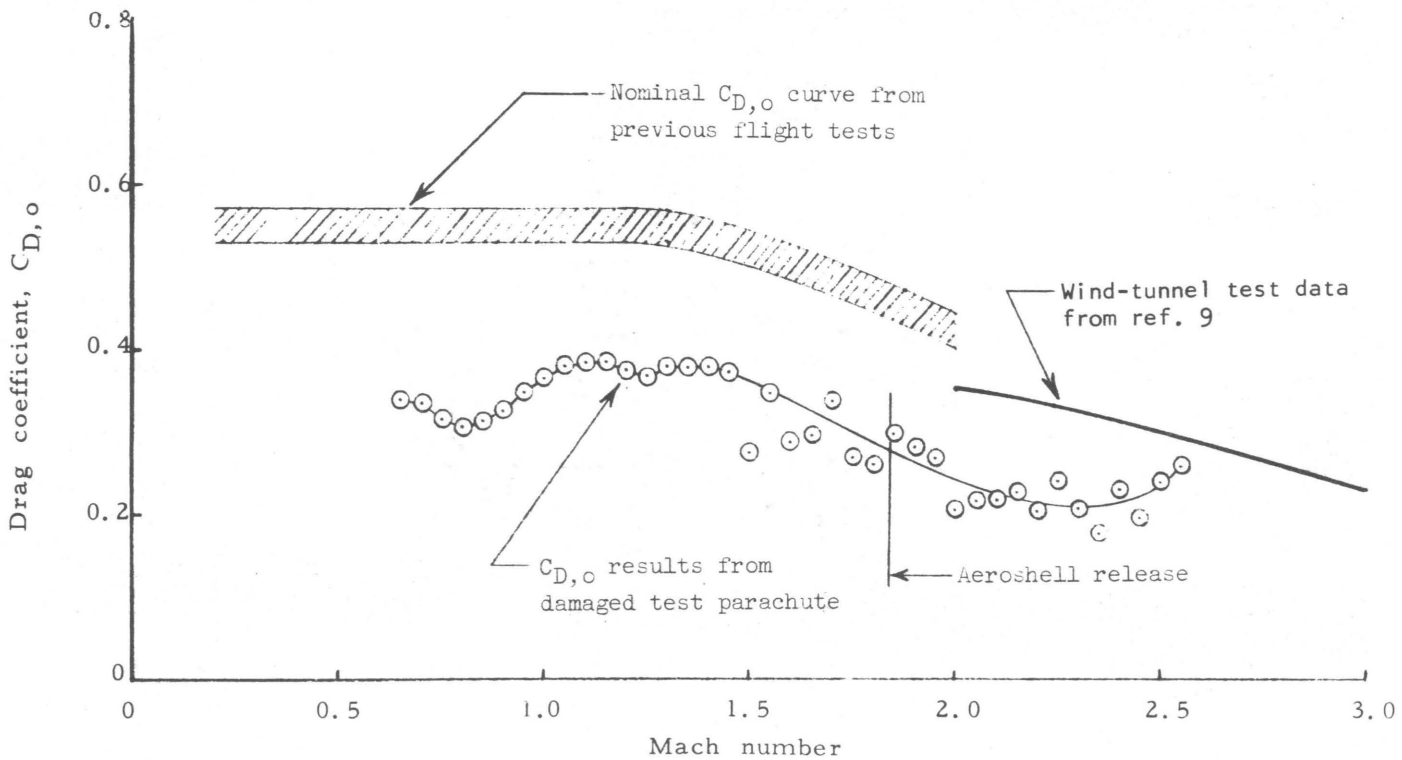

Figure 33.- Drag coefficient as a function of Mach number.

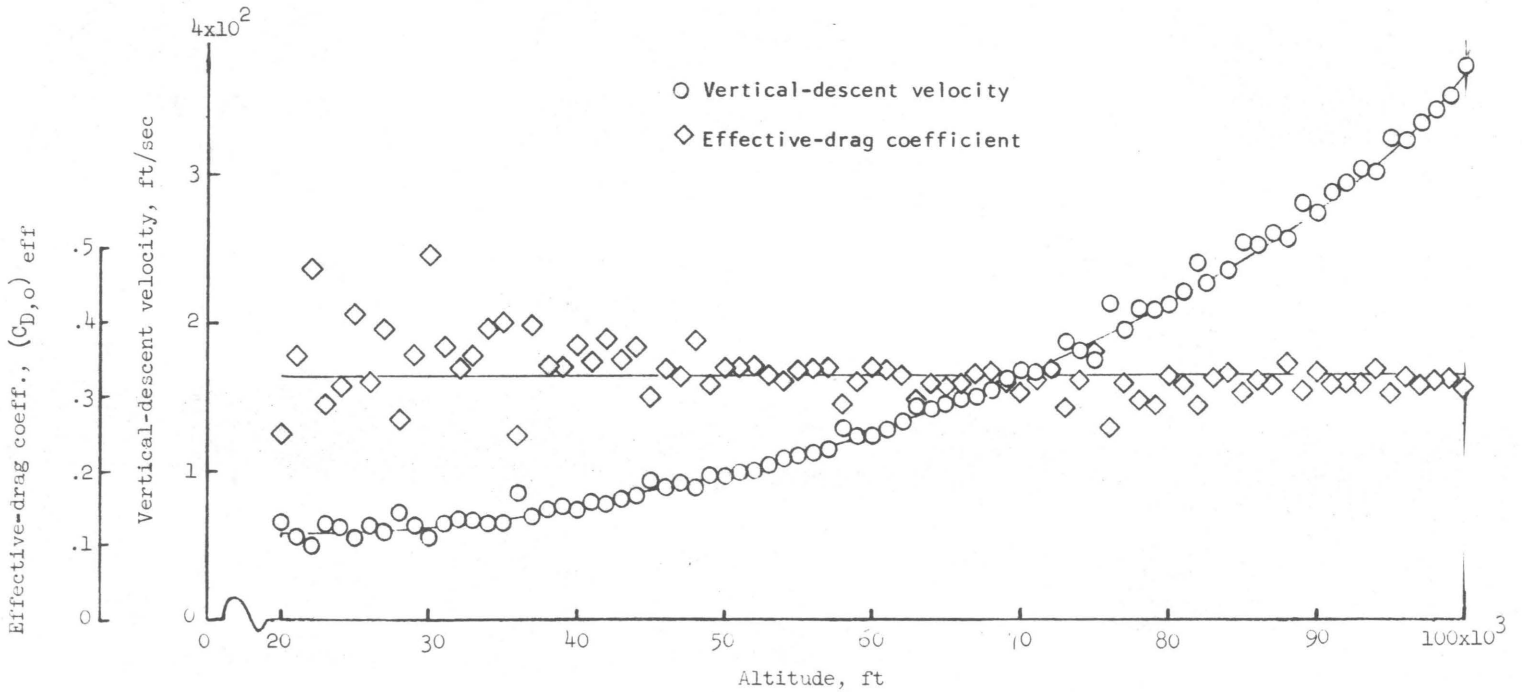

Figure 34.- Variation of vertical-descent velocity and effective-drag coefficient with altitude.

attitude of the parachute with respect to the forebody and then, by time correlation with the aeroshell-payload attitude data (from the gyro platform), determining the parachute position with respect to the flight path. The parachute and the aeroshell-payload pitch and yaw attitude data are shown in figure 35 for the first 10 seconds after mortar firing.

The attitude data shown in figure 35 include a correction (plus 3.7 degrees yaw and minus 3.2 degrees pitch angle) based on a determination of the center-of-oscillation of the aeroshell-payload during the interval immediately prior to deployment of the test parachute. The pitch angle is in the vertical plane of the vehicle flight path and the yaw angle is in a plane perpendicular to the vertical plane. The aeroshell-payload was in a nose up and nose left attitude (in this report a negative value of pitch and positive value of yaw) with respect to the flight path at the instant of mortar firing. The parachute was therefore deployed below and to the right side of the flight path. During the interval from t' = 0 to about t' = 0.75 seconds the unfurling parachute remained below and to the right of the flight path essentially in the orientation in which it was deployed. As the parachute inflation sequence began (at about t' = 0.83 sec) the parachute became aligned with the flight path and after the first inflation of the parachute at t' = 1.21 seconds the parachute motion closely followed the motion of the forebody. During the time interval immediately following the first inflation the parachute experienced its most extreme motions. It was also during this time interval (from t' = 1.21 seconds to about t' = 4.0 seconds) that the

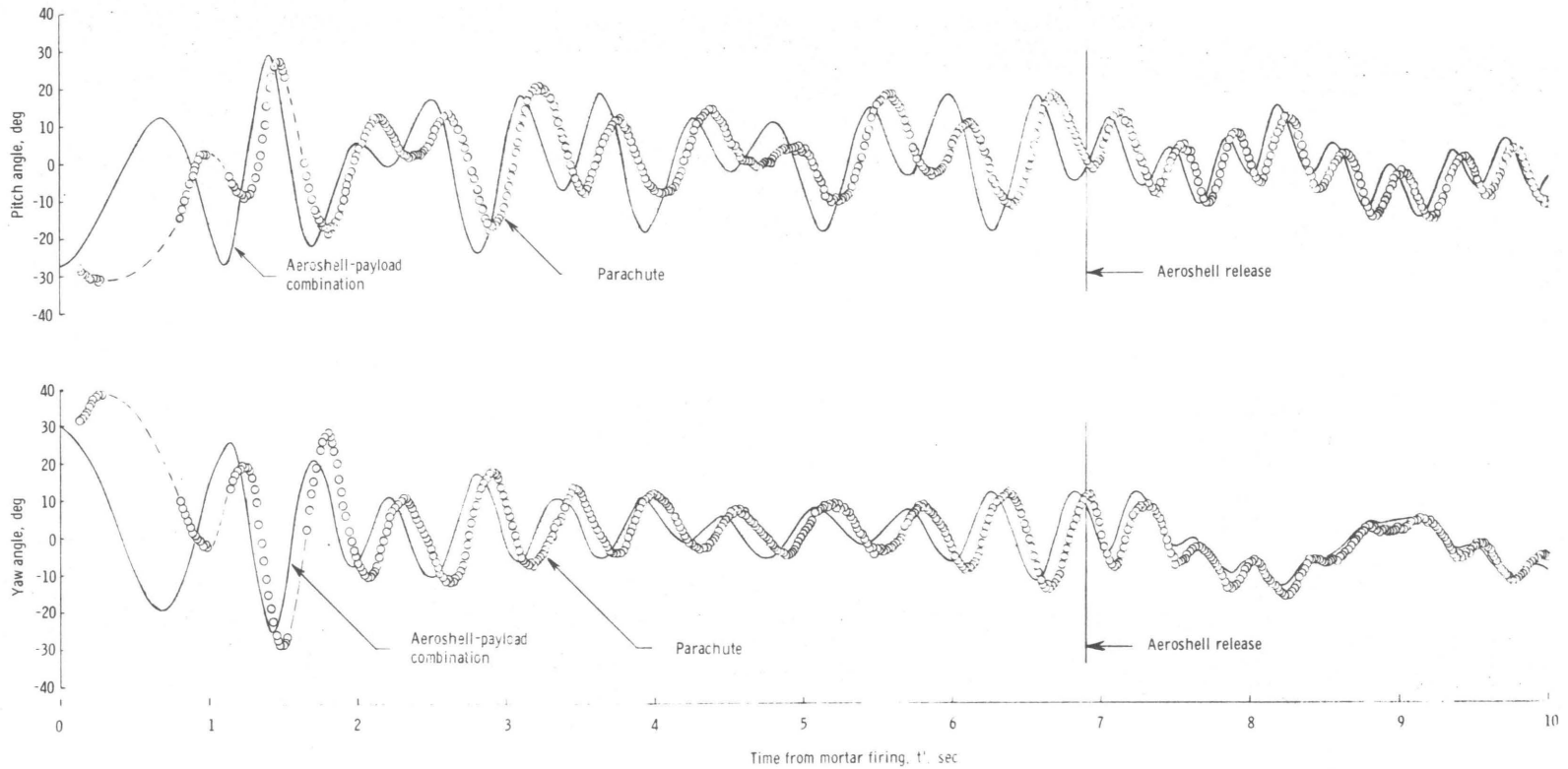

Figure 35.- Payload and parachute pitch and yaw angle with respect to vehicle flight path.

majority of the canopy damage occurred. Evaluation of the aft camera film indicated that there were abrupt and severe changes in parachute canopy shape associated with the rapidly changing attitude of the parachute and forebody and in at least one instance damage to a particular area of the canopy can be observed as the shape change took place, figure 29c (frame 77 to 79).

C. Parachute Damage Analysis

Damage description.- Damage to the test parachute canopy occurred in the outer area of the disk and to all areas of the band. The center or nomex portion of the disk was undamaged. There were no tensile failures of any of the primary load carrying structural members of the parachute (suspension lines, radial tapes, or circumferential tapes). However, there were several failures of the stitching joining the radial tapes to the canopy hem tapes. Stitching failures occurred at 27 of the 42 radial tapes at the outer edge of the disk and at 9 of the radial tapes at the upper band edge. Figure 36 presents a photograph of two gores showing typical damaged areas and figure 37 presents a sketch of the parachute canopy indicating all of the damaged areas. The times at which damage could first be identified in different parts of the parachute are listed in table 10.

Damage causes.- After opening, the test parachute experienced rapid changes in shape and frontal area (figures 29 and 30) and position relative to the aeroshell-payload and flight path (figure 35). These changes in parachute shape, frontal area, and angular position resulted in a continually shifting pattern of parachute loading and frequent

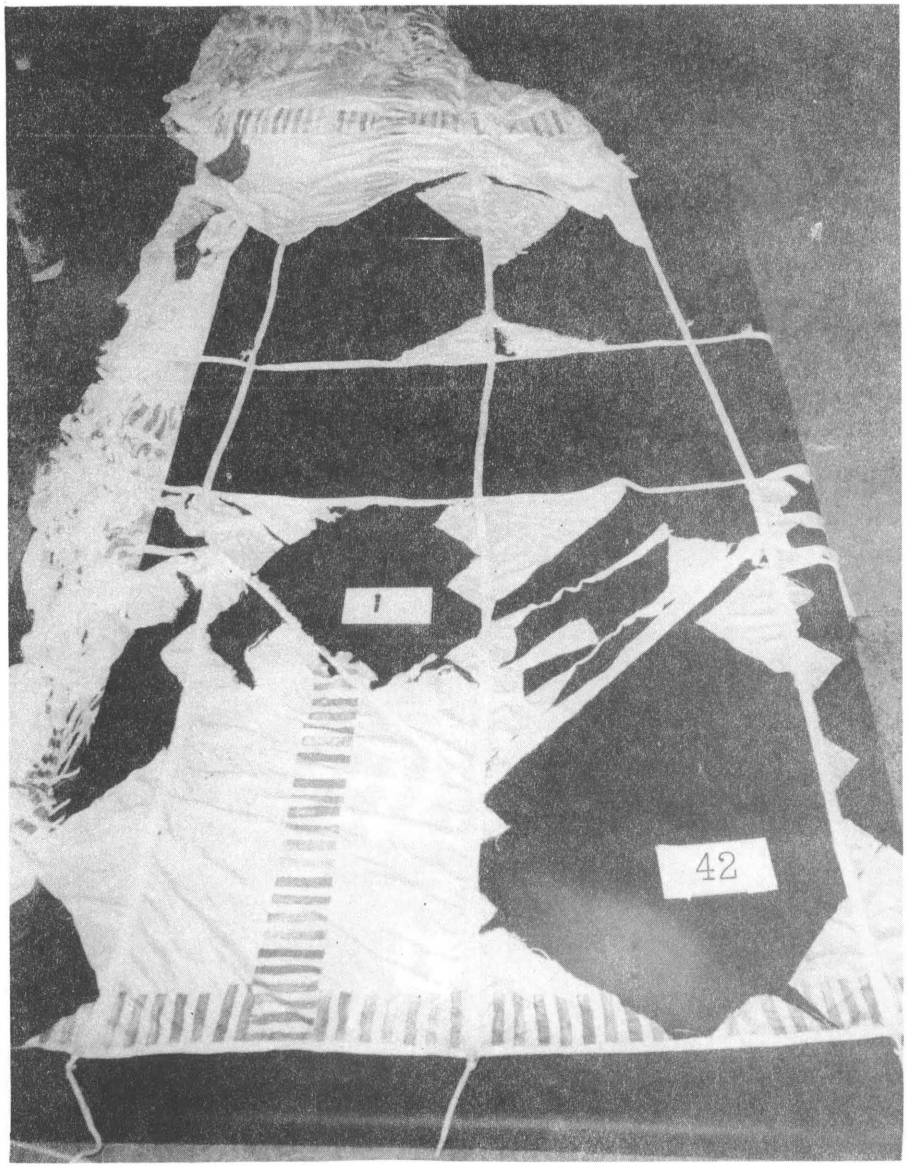

Figure 36.- Photograph showing typical damaged areas of parachute canopy.

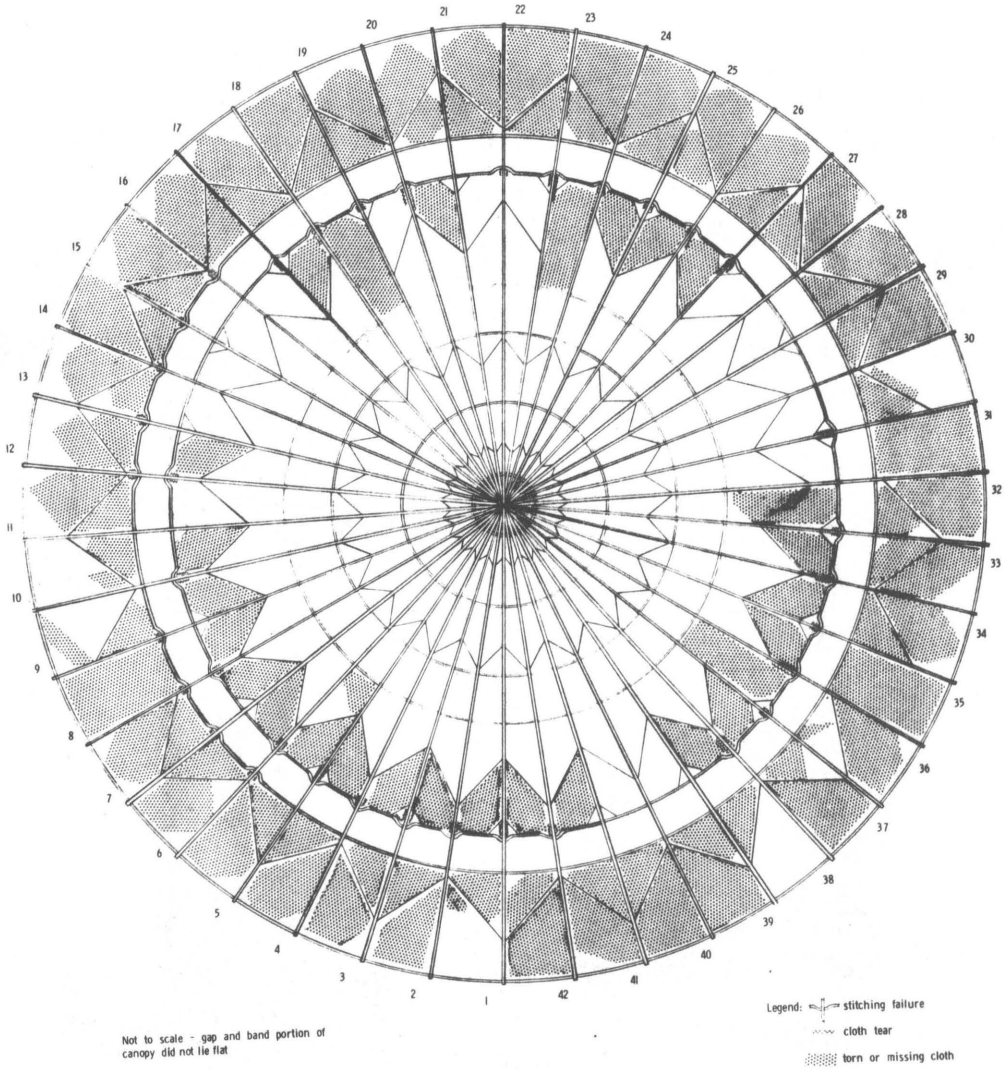

Figure 37.- Sketch showing canopy damage.

TABLE 10. PARACHUTE DAMAGE IDENTIFICATION CHART

Time, t', sec	Disk-area damage, gore no.	Band-area damage, gore no.
1.19	2, 4, 10	
1.21	23	
1.23	26	
1.26	33	33, 34, 35
1.27	17, 18	
1.29	22	
1.35	1, 41	
1.37	6, 37	
1.38	35	
1.40	3, 5	
1.50	24, 36	
1.56		21
1.83		3, 39, 41
1.85	7, 9	32
1.86	8	26, 37
1.89	42	19, 23, 24, 25
1.91		9
1.93	25, 38	13
2.10	34	27
2.87		1, 2, 4
2.91	20	
3.47	32	

transfer of loads between adjacent canopy gores through the gore tapes and cloth panels. In addition, this changing pattern of parachute loading resulted in shear-type loads between the radial tapes and the circumferential hem tapes. The major cause of damage occurring in the disk was failure of the stitching joining the radial tapes to the adjacent gore cloth. In the band area it is believed the major cause of damage was the transfer of loads between adjacent gores across the cloth panels in a diagonal direction.

Aerodynamic heating.- Prior to the flight test an analysis was made of the aerodynamic heating environment to be expected for the test parachute. This analysis indicated that temperatures would approach 400°F in the central area of the disk part of the parachute canopy. On the basis of this analysis and experience gained on a previous flight (reference 6) nomex cloth was used in the central disk area of the canopy (as shown in figure 8) and, in addition, there were three circumferential reinforcement tapes located in this area to act as rip stops and to prevent propagation of any cloth damage that might occur in this area. As was mentioned previously no damage occurred in this reinforced section.

On the flight test parachute there was considerable evidence of localized material melting or burning on the damaged areas of the parachute cloth. Because of the localized nature of the burned areas it is believed that these burns resulted from friction burning caused by torn pieces of canopy cloth flailing in the airstream and against the remaining cloth panels rather than from aerodynamic heating. However,

the dacron cloth materials may have been considerably degraded in strength as a result of elevated temperatures caused by aerodynamic heating.

D. Predicted Mars Performance

The subject parachute flight test is anything but ideal for predicting the performance of the parachute for a Mars mission. The unanticipated deployment while the aeroshell-payload combination was oscillating through an angle-of-attack range of the ±40 degrees resulted in a very unstable deployment and the parachute and the aeroshell-payload remained unstable for over ten seconds. Since the unstable motions of the parachute were the result of an unstable forebody, no conclusions can be reached about the stability performance of the parachute for a Mars mission.

The damage to the parachute resulted in a significant reduction in drag. During entry through the Mars atmosphere this decrease in drag would have caused an increase in the vehicle velocity at the retro ignition altitude. The drag was reduced to about 60 percent of the expected drag with a resulting drag coefficient 0.32 and ballistic number (m/C_DA = 0.16 slug/ft^2) for parachute and aeroshell-payload combination.

As noted in Chapter III terminal velocity occurs when drag equals weight. An expression for terminal velocity as a function of ballistic number and density was derived earlier (equation 19) as follows:

$$V_t = \sqrt{\frac{2g_m(m/C_DA)}{\rho}}$$

The analytical expression above was used to evaluate the significance of the reduction in drag of the damaged parachute since terminal velocity is reached by retro ignition altitude during a Mars entry. By calculating a terminal velocity based on the ballistic number of the damaged parachute, the amount of propellant required for a retro descent system to soft land a spacecraft that had descended with such a damaged decelerator system can be estimated. The terminal velocity for a Mars mission based on the drag of the damaged decelerator system is 420 ft/sec. The propellant requirement is increased only slightly and is still in the acceptable range established by figure 7 in Chapter III. Therefore, the decreased drag of the damaged parachute would not in itself cause failure of the Mars mission. However, the extreme dynamic oscillations are not acceptable but they are not attributed to the parachute system.

IX. SUMMARY

A systems analysis is presented for simulation of the descent of a decelerator (parachute) and spacecraft for entry through the atmosphere of the planet Mars by a flight test in the Earth's atmosphere. The analyses include definition of engineering atmosphere models for Mars, discussion of parachute model and scaling laws for Earth simulation of Mars performance, definition of a mission profile for a planetary spacecraft mission to Mars, and the selection and design of a parachute for use on a full-scale Earth simulation flight test. The results of the flight test of the parachute are presented along with the application of these results to a spacecraft mission to Mars.

BIBLIOGRAPHY

1. Heinrich, H. G.: "Model Laws Governing Parachute Performance in Martian Environment", Sonderdruck aus Raumfahrtforschung, Heft 3, July - September 1967.

2. Heinrich, H. G., and Haak, E. L.: "Stablility and Drag of Parachute with Varying Effective Porosity", ASD-TDR-62-100, September 1962, Aeronautical Systems Div., Wright Patterson Air Force Base, Ohio.

3. Heinrich, H. G.: "The Effective Porosity of Parachute Cloth", Zeitschrift fuer Flugwissenschaften, Vol. 11, Heft 10, Verlag Friedr. Vieweg & Sohn, Braunschweig, Germany.

4. Chernowitz, G., ed.: Performance of and Design Criteria for Deployable Aerodynamic Decelerators. ASD-TR-61-579, AF Flight Dynamics Laboratory, Wright Patterson AFB, Ohio, December 1963.

5. Eckstrom, C. V., and Branscome, D. R.: High-Altitude Flight Test of a Disk-Gap-Band Parachute Deployed Behind a Bluff Body at a Mach Number of 2.69. NASA TMX-2671, 1972.

6. Eckstrom, C. V.: Flight Test of a 40-Foot-Nominal-Diameter Disk-Gap-Band Parachute Deployed at a Mach Number of 3.31 and a Dynamic Pressure of 10.6 Pounds Per Square Foot. NASA TMX-1924, 1970.

7. Henning, A. B., and Lundstrum, R. R. (With Appendix A by James C. Young): Flight Test of an Erectable Spacecraft Used for Decelerator Testing at Simulated Mars Entry Conditions. NASA TN D-6910, 1972.

8. Preisser, J. S.: Determination of Angles of Attack and Sideslip from Radar Data and a Roll-Stabilized Platform. NASA TMX-2514, 1972.

9. Bobbitt, P. J., Mayhue, R. J., Faurote, G. L., and Galigher, L. L.: Supersonic and Subsonic Wind-Tunnel Tests of Reefed and Unreefed Disk-Gap-Band Parachutes. AIAA Papper No. 70-1172, September 1970.

10. Eckstrom, C. V., and Preisser, J. S.: Flight Test of a 40-Foot-Nominal Diameter Disk-Gap-Band Parachute Deployed at a Mach Number of 2.72 and a Dynamic Pressure of 9.7 Pounds Per Square Foot. NASA TM X-1623, 1968.

11. Anon: U.S. Standard Atmosphere, 1962. NASA, U.S. Air Force, and U.S. Weather Bureau, December, 1962.

12. Whitlock, C. H., and Bendura, R. J.: Inflation and Performance of Three Parachute Configurations From Supersonic Flight Tests in a Low-Density Environment. NASA TN D-5296, 1969.

13. Murrow, H. N., and McFall, J. C., Jr.: Some Test Results From the NASA Planetary Entry Parachute Program. J. Spacecraft and Rockets, Vol. 6, No. 5, May 1969, pp. 621-623.

14. Henn, Die Absinkeigenschaften von Fallschirmen, Aerodynamisches Institut der Technischer Hochschule, Darmstadt, Germany, 1944.

15. Thompson, R. P.: The Practical Problem of Landing on Mars, Astronautics and Aeronautics, July 1966, pp. 66-73.

16. Worth, R. N.: Descent and Landing Systems for Unmanned Mars Entry, Minutes of AIAA/AAS Meeting. "Stepping Stones to Mars", 1966, pp. 116-124.

17. Costigan, P. J.: Dynamic Model Study of Planetary-Entry Configurations in the Langley Spin Tunnel, NASA TN D-3499, 1966.

18. O'Hara, F.: Notes on the Opening Behavior and the Opening Forces of Parachutes, Royal Aeronautical Society Journal, Vol. 53, November 1949, pp. 1053-1062.

19. Gillis, C. L.: Deployable Aerodynamic Decelerators for Space Missions, J. of Spacecraft and Rockets, Vol. 6, No. 8, August 1969, pp. 885-890.

20. Technical Voids in Aerodynamic Deceleration R & D, Astronautics and Aeronautics, AIAA Technical Committee on Aerodynamic Deceleration Systems, December 1968, pp. 57-59.

The vita has been removed from the scanned document

FLIGHT TEST OF A SUPERSONIC DECELERATOR ON EARTH TO SIMULATE A MARS ENTRY

By

Darrell R. Branscome

ABSTRACT

A systems analysis is presented for simulation of the descent of a decelerator (parachute) and spacecraft for entry through the atmosphere of the planet Mars by a flight test in the Earth's atmosphere. Engineering atmosphere models for Mars are defined and based on these models requirements for parachutes to be used for Mars entry are developed. Appropriate parachute model and scaling laws for Earth simulation of Mars performance are developed. A disk-gap-band parachute was selected for a flight test on Earth to simulate a mission profile of a decelerator for a planetary mission to Mars.

The parachute is sized for a defined mission profile and accepted empirical methods are used to perform the design analysis of the parachute. A description of the flight test spacecraft system and the performance of the parachute during the full scale flight test is presented. The parachute sustained considerable damage during the test. The results of the Earth flight test are used to discuss predicted performance for an identically damaged parachute on Mars.